TÉCNICO LISBOA

Experimental investigation and kinetic modeling of CO_2-CH_4 plasmas

Rodolfo Lopes Pacheco Marques Simões

Thesis to obtain the Master of Science Degree in

Engineering Physics

Supervisor(s): Prof. Dr. Vasco António Dinis Leitão Guerra
Supervisor(s): Prof. Dr. Tiago Filipe da Ponte Silva

Examination Committee

Chairperson: Prof. Dr. Luís Paulo Da Mota Capitão Lemos Alves
Supervisor: Prof. Dr. Tiago Filipe da Ponte Silva
Member of the Committee: Prof. Dr. Carlos Daniel Diogo Matias Pintassilgo

November 2021

Acknowledgments

First and foremost, I would like to express my gratitude towards my supervisors: To Prof. Tiago Silva for being a key support throughout this journey, given the dedication and availability to constantly give me feedback, which undoubtedly had a very positive impact in this work. And to Prof. Vasco Guerra for all the guidance, encouragement and for giving me the opportunity to work on this topic. Secondly, I would like to thank everyone at École polytechnique and Laboratoire de Physique des Plasmas for giving me the opportunity to work in Paris and the necessary tools to pursue my research, even during times of uncertainty.

Gostaria também de agradecer a todas as pessoas que durante estes 6 anos se cruzaram comigo no Instituto Superior Técnico e me fizeram crescer tanto. Todas as expectativas que poderia ter sobre a minha vida universitária foram largamente ultrapassadas e não tenho nenhuma dúvida que terá sido um dos melhores períodos da minha vida. A todos os meus amigos de MEFT e a todos os meus amigos da Associação, um sincero obrigado. E à minha querida Inês, que tudo fez para que conseguisse terminar este capítulo, o meu maior agradecimento,

Por último, um agradecimento à minha querida família, que, como sempre, me apoiou e me abriu todas as portas possíveis para que me tornasse uma pessoa feliz e concretizada.

Resumo

Estudar os plasmas de CO_2 e CH_4 pode nos ajudar a enfrentar um dos mais importantes desafios científicos modernos: dissociar eficientemente as moléculas de CO_2 e reduzir a quantidade de gases de efeito estufa na atmosfera. Para isso, é fundamental que seja alcançada uma sólida compreensão do funcionamento interno do plasma. Para ajudar a consegui-lo, foi realizado um estudo experimental sobre a composição química do plasma, a tempreatura do gás e o seu espectro de emissão. Além disso, foi desenvolvido um modelo cinético capaz de simular o comportamento do plasma para diferentes condições, o que permite um estudo quantitativo das reações mais importantes que ocorrem no plasma.

Palavras-chave: Plasmas frios, Plasmas de CO_2 e CH_4, Descarga luminescente, Modelo Cinético

Abstract

Understanding CO_2/CH_4 plasmas can help us address one of today's most pressing scientific issues: To dissolve carbon dioxide molecules efficiently and lower the amount of greenhouse gases in the atmosphere. It is critical to gain a firm understanding of the inner workings of the plasma for this. An experimental investigation of the chemical composition of the plasma, its gas temperature, and its emission spectrum was done to contribute to this effort. Furthermore, a kinetic model capable of replicating plasma behavior under various conditions was developed, allowing for a quantitative examination of the plasma's most critical reactions.

Keywords: Cold Plasmas, CO_2/CH_4 Plasmas, Glow discharge, Kinetic modelling

Contents

List of Tables

List of Figures

Acronyms

DRM Dry reforming of methane. 12

FTIR Fourier Transform Infrared Spectroscopy. 17

IPCC Intergovernmental Panel on Climate Change. 2

LoKI The LisbOn KInetics Simulation Tool. 41

OES Optical Emission Spectroscopy. 17

Chapter 1

Introduction

Plasmas are typically referred to as the fourth state of matter and can be considered an ionized gas composed of positively charged ions, electrons and neutrals (atoms, molecules and radicals). [1]. Plasma phenomena are seen all across the Universe, ranging from interstellar space to discharge tubes produced in research laboratories, with a wide variety of physical and chemical properties. The study of plasmas has resulted in a large number of discoveries and technological breakthroughs that are present in our daily lives. For example, the entire microelectronic industry that forms the technological base of modern society is enabled thanks to plasma-surface interactions through sputtering, etching, activation, etc [2]. In recent years, we achieved significant advancements in understanding a wide range of fundamental plasma science problems. Scientists have been able to create plasmas that are only a few millimeters in diameter, allowing them to get previously unattainable insight into astrophysical events. [3] Relativistic plasmas are being manipulated by intense short-pulse lasers, resulting in compact high-gradient accelerator and ultrahigh intensity x-ray sources [3]. High energy density plasmas have also been created, allowing researchers to study the physics of the inner cores of stars and planets, and using this knowledge to advance nuclear fusion research [3]. At the same time, plasmas are being researched for important human health applications: Indeed, when considering the current set of plasma applications, plasma medicine is experiencing fast growth due to its potential for wound healing, dermatology and cancer treatment [3]

Another plasma application, widely discussed nowadays, relates to plasma-assisted chemical conversion for the reforming of CH_4 and management of CO_2. This application has the potential for developing new environmentally friendly processes using renewable electricity and improving current chemical/reforming processes. To progress towards the understanding of plasma-based conversion, this thesis aims studying the potential of plasmas to generate hydrocarbons from CO_2-CH_4 mixtures in order to create fuels and chemical feedstock. In this vision of the future, plasma can act as a processor of electricity into chemistry, providing pathways that are environmentally friendly. The current work relies on the systematic investigation of key points important for the efficient decomposition of CO_2-CH_4 mixtures in plasmas through studying the basic plasma parameters, namely dissociation degree, gas temperature and vibrational excitation.

This first chapter is organized as follows: first, in section 1.1 we address in detail the environmental problem, which motivates the study of plasma-assisted chemical conversion; in section 1.2 we present low-temperature plasmas, while addressing their their potential for chemical conversion; in section 1.3 and 3.3.2 we explore several details related to CO_2 chemistry and CO_2 conversion. Finally, in section 1.5 a brief outline of the rest of the thesis is given.

1.1 The environmental problem

It is commonly accepted that the generation of energy from fossil fuels was an achievement that had a massive influence on nearly every area of our lives and society. Although fossil fuels facilitated significant scientific breakthroughs in the industry, engineering, medicine, and other fields, we now are reliant on nonrenewable energy sources, which harm our ecosystem. Indeed, if major adjustments are not made, many of contemporary society's recent accomplishments begin to be threatened.

The excessive use of fossil fuels results in the release of greenhouse gases such as CO_2. Since the beginning of the Industrial Age, the concentration of CO_2 in our atmosphere has increased by a large proportion, increasing the global temperature of the planet. This is referred in the IPCC Sixth Assessment Report AR6 [4] that the *"observed increases in well-mixed greenhouse gas (GHG) concentrations since around 1750 are unequivocally caused by human activities"*. Furthermore, each of the last four decades has been warmer than any decade that preceded 1850 and the global surface temperature has already increased approximately 1.0 ºC, as a result of human activity.

This rapid rise in global temperature is expected to have disastrous implications for our environment, including rising sea levels, greater extreme weather occurrences, more droughts, more heat waves, extinction of animal species, and many others. It is therefore vital that we make the switch from fossil fuels to renewable energy sources in order to achieve a sustainable energy dependency in the short future.

Despite the potential of renewable sources to mitigate fossil fuel emissions, this type of energy is unable to create stable electrical power because of their inconsistency and the imbalance between supply and demand [5]. It is then vital to investigate new and efficient ways to store electrical energy that can be used when necessary. The development of an energy storage pathway, which converts transient electrical energy into valuable chemical molecules, has the potential to solve this problem. This strategy is the so-called power-to-gas approach (see figure 1.1). Here the CO_2 molecules are dissociated and combined with H2O to produce syngas (mixture of H_2 and CO), provided that a surplus of electricity is available from the electricity grid.

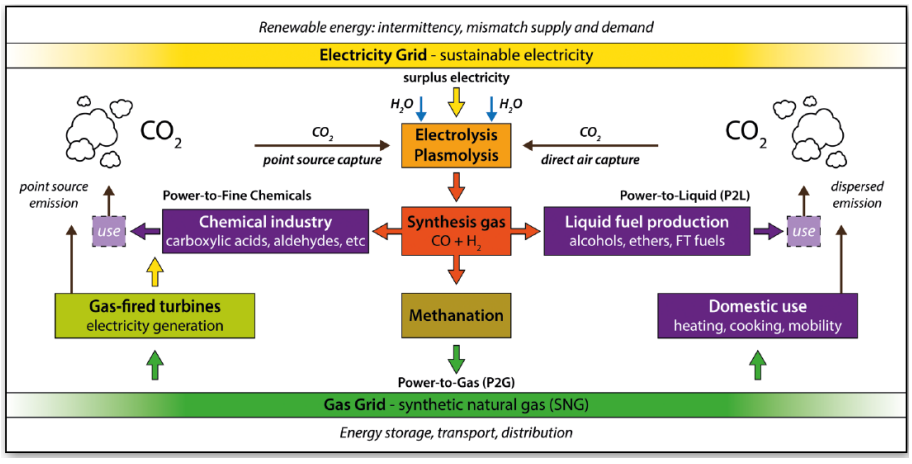

Figure 1.1: Example of the CO_2 cycle, using Electrochemical Conversion or Plasma Conversion. Taken from [5]

Note that the storage of energy in hydrocarbons takes advantage of existing infrastructure for energy transport and distribution, while enabling very high volumetric energy density when compared to other storage schemes, e.g., batteries, flywheels, etc. More details can be found in [5].

One of the most difficult tasks in implementing this cycle is properly dissociating the relatively stable CO_2 molecule. Note that CO_2 dissociation is an highly endothermic reaction. Under classical industrial conditions, this reaction is limited by the rate of heat transfer. Consequently, this leads to high production

costs, which turns the whole CO_2 conversion chain economically unreasonable. In this context, plasmas provide an ideal environment for molecular conversion due to the formation of energetic and chemically active species that can initiate chemical reactions that are difficult of impossible to obtain using ordinary thermal mechanisms. Among different types of plasmas that can be used for CO_2 and CH_4 reforming, the so-called low temperature plasmas are the most promising candidates [1]. Detailed information about non-thermal plasmas and their potential for CO_2 and CH_4 reforming will be given in the section below.

1.2 Low temperature Plasmas

Low temperature plasmas are characterized by non-equilibrium conditions under which electrons, ions and neutral species have different translational and-in case of molecules - internal (ro-vibrational) energies. Indeed, this allows to create a specific non-equilibrium gaseous media in which endothermic processes with increased energy efficiencies and dissociation rates can be achieved.

In the context of plasma-based CO_2 decomposition, it has been estimated (see e.g. [1]) that low temperature plasmas can activate the vibrational excitation of CO_2 molecules because of the characteristic low electron energies with 1-2 eV. In this temperature range, it has been estimated that about 95% of all the discharge energy is transferred from plasma electrons to the vibrations of CO_2 molecules, mostly to their asymmetric vibrational mode (see more details below). This is particularly relevant because energy accumulated in CO_2 vibrations can be used to decompose the CO_2 via the so-called vibration ladder climbing..

The previous point justify the abundant number of CO_2 non-thermal discharge experiments being developed nowadays with the aim of achieving high energy efficiencies in CO_2 decomposition. Among various plasmas sources used to investigate CO_2 decomposition (radio frequency discharges, dielectric barrier discharges, gliding arc plasmatrons microwave plasmas, etc.) the glow discharges are one of the most well-known setups. Despite the low energy efficiency and moderately low CO_2 dissociation fraction values typically associated with DC glow discharges [3], these plasma sources constitute ideal systems for fundamental studies given their simple geometry and homogeneity of the plasma. These features facilitate the study of CO_2 plasmas through the use of volume average 0D self-consistent kinetic models to account for its very complex kinetics.

In general these discharges are created when applying a potential difference between two conductive electrodes, which are placed into a low pressure chamber filled with gas. Because of the electric field between the plates, electrons emitted from the cathode will be drawn towards the anode, creating electron-ion pairs on their way through collisions with neutrals. The ions generated in this way will travel in the opposite direction bombarding the cathode and thereby causing new electrons to be emitted.

Because electrons have a relatively tiny mass in comparison to positive ions, they are quickly accelerated by the electric field, therefore their temperature will be significantly higher than that of the heavier species. Thus, whereas heavy ions have temperatures similar to neutral molecules, electrons have temperatures in the order of 10 000 K. Collisions will generate excited molecules, which can decay to lower energy levels and emit light, which is one of the plasma's distinctive features. The simplified structure of a DC glow discharge is presented schematically in Fig. 1.2.

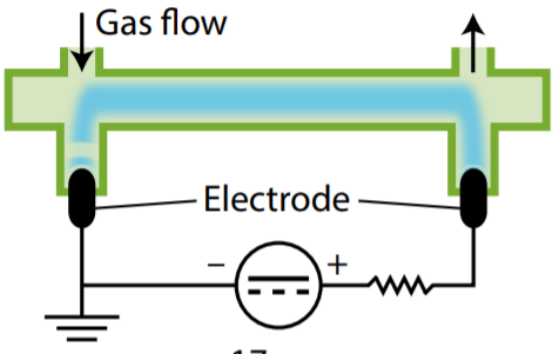

Figure 1.2: Experimental setup for a low temperature, glow discharge plasma. Adapted from [6].

1.3 Vibrational and Rotational energy levels

This section overviews some basic aspects associated with CO_2 and CH_4 vibrational/rotational kinetics, and some theoretical concepts on which this work is based upon. Regarding CO_2, it is worth noticing that this molecule is triatomic, linear and symmetric [1]. This leads to three vibrational modes - the symmetric strecthing mode (v_1), the double degenerate bending mode (v_2), and the asymmetrical stretching mode (v_3). These modes (illustrated in figure 1.3) are typically represented using the Herzberg notation $CO_2(v_1, v_2^{l_2}, v_3)$, where $l2$ is the projection of the momentum of bending vibrations onto the axis of the molecule. It can take the values $l_2 = v_2, v_2 - 2, v_2 - 4, ...,$ 1 or 0, depending on whether v_2 is odd or even (see more details in [1]).

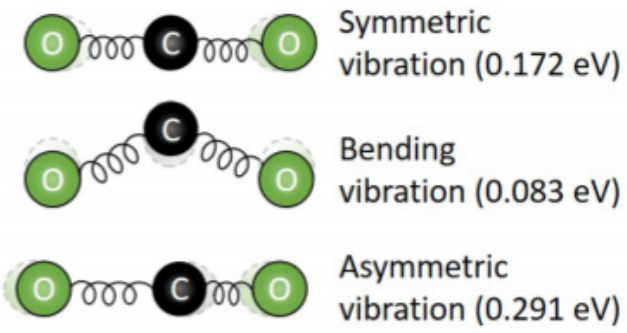

Figure 1.3: Vibrational modes for the CO_2 molecule. Taken from [7]

The kinetics associated to the asymmetric mode has been widely studied. Indeed, this mode is usually related to vibrational-vibrational exchanges, which can stimulate the molecular dissociation through the so-called vibrational ladder climbing mechanism (see e.g. [1] reference). At the same time, the study of symmetric and bending modes of vibration is also of special importance given the phenomenon of Fermi Resonance, which leads to an energy shift of vibrational levels with equal symmetry associated to the bending mode (figure 1.4). Note that for a fermi resonance to take place, two vibrational states must have nearly the same energy, which in the case of CO_2, occurs for levels $CO_2(v_1, v2^{l2}, v3_)$ and $CO_2(v_1 - 1, (v2 + 2)^{l2}, v3_)$. One example of this resonance relates to the levels (02^00) and (10^00). Under fermi resonance, these two levels possess the energies of approximately 1285.4 and 1388.2 cm^{-1}, with an average energy of 1336.8 cm^{-1} (see left column - bottom line in figure 1.5). Note that this average energy is roughly the same as the energy associated to bending level 02^20 (see middle column - second line in figure 1.5).

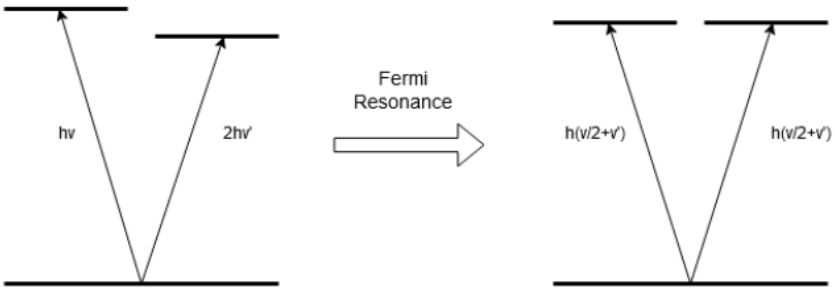

Figure 1.4: Energetic representation of Fermi Resonance.

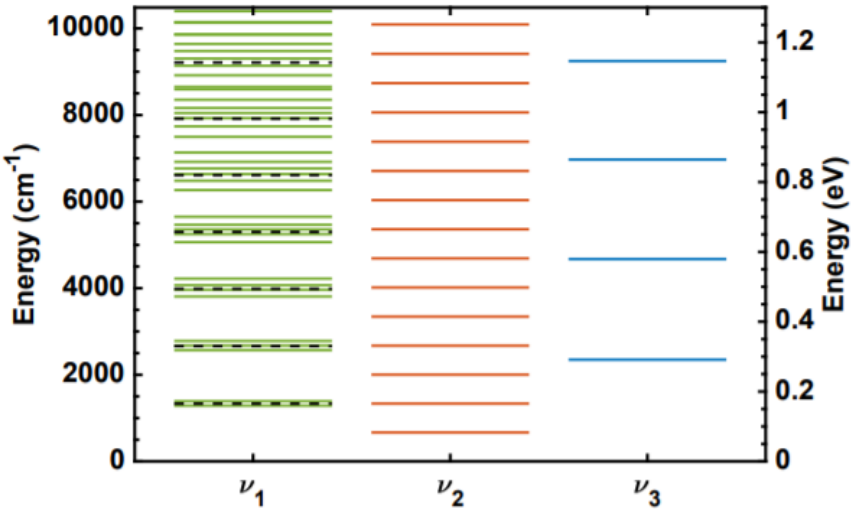

Figure 1.5: CO_2 vibrational modes, up to 10.500 cm^{-1} . For ϵ_1, the dashed black lines indicate the energy of pure levels, and the green lines are the new vibrational levels, resulting from the Fermi resonance between the symmetric stretch and the bending mode. Taken from [6]

We turn now our attention towards relation between the energy of vibrational levels and molecular dissociation. There are three major contributions to molecule energy: electronic energy, which comes from the energy levels of the electrons in their orbitals (n), vibrational excitation, which depends on the excited vibrational modes (v), and rotational energy, which depends on the molecule's total angular momentum (J). Nuclear energy contributions are ignored in the case of low temperature plasma. The molecular energy may then be expressed as a sum of three different contributions:

$$E_{evJ} = hc(T_e + G_e(v) + F_{ev}(J)) \tag{1.1}$$

Where T_e is the electronic energy, which is tabulated for each electronic state, $G_e(v)$ is the vibration energy and $F_{ev}(J)$ the rotational energy. The values for the vibrational and rotational energies depend on the approximations and the molecule. We can, for example, look at the model proposed at [7], where an anharmonic oscillator and rotor dependency on the vibrational levels for CO_2 is considered. In this case, the vibrational energy, can be approximated by [8]:

$$G_e(v) = \sum_{k=1}^{3} w_k(\nu_k + d_k/2) + \sum_{k=1}^{3}\sum_{j\geq k}^{3} \chi_{kj}(\nu_l + d_k/2)(\nu_j + d_j/2) + g_{22}l_2^2, \tag{1.2}$$

where ω_k, χ_{kj}, g_{22} are spectroscopy constants, d_k the degeneration of a given mode ($d_1 = d_2 = 1$, $d_3 = 2$), and v_k the quantum numbers for the 3 vibrational modes. This expression is obtained with first order perturbation theory approximations. Finally, for the rotational energy, it can be approximated by [9]:

$$F_{ev}(J) = B_v(J(J+1)) - D_v(J(J+1))^2 + H_v(J(J+1))^3 \tag{1.3}$$

where B_v, D_v and H_v are rotational constants whose values can be found in [10].

A representation of the energy levels of the CO_2 molecule is shown in figure 1.6. This figure provides a good illustration of two possible ways of dissociating CO_2: either by a step-wise vibrational excitation (also referred to as vv up-pupping mechanism), or direct dissociation by electron impact. In the first, the CO_2 vibrational levels are excited one by one, and the energy of the molecule increases until it dissociates into CO and O. On the other hand, in the direct dissociation, an electron collides with the CO_2 molecule, causing the separation into CO and O, without any vibrational excitation. As it is shown in figure 1.6, the vibrational pumping mechanism requires less energy than the electron impact dissociation (5.5eV compared to 7.5eV), which is very important if our goal is to maximize the energetic efficiency of this process.

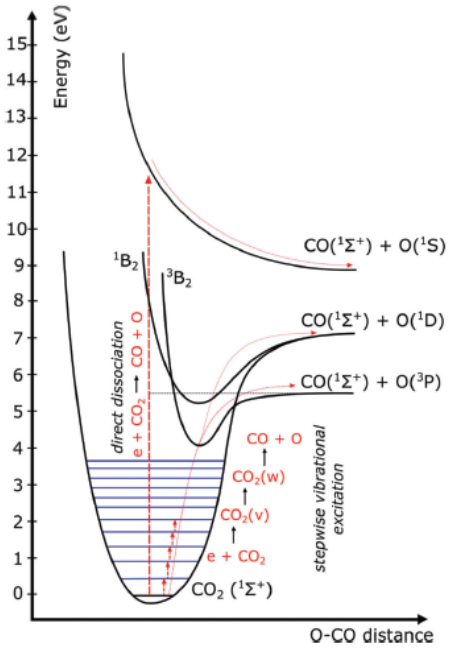

Figure 1.6: Potential energy values of electronic states of CO_2, as a function of the internuclear distance [1]

In regards to the CH_4 molecule, we can make the following claims: There are three translational degrees of freedom, three rotational degrees of freedom, and nine vibrational degrees of freedom in this tetrahedral molecule. Due to its inherent geometry, and because all of the vertices are H atoms, these vibrational modes are degenerated.

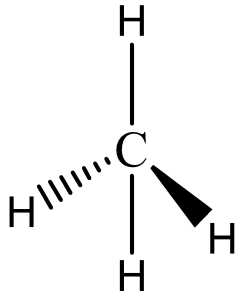

Figure 1.7: Three dimensional representation of CH_4 molecule.

Indeed, after combining the degenerate modes, methane has just four different vibrational modes. Thus, a methane molecule's vibrational state can be expressed as $CH_4(v_1, v_2, v_3, v_4)$ with degeneracies (1,2,3,3). The values for rovibrational constants can be found in [11]. Reference [12] provides a visual representation of the vibrations.

1.4 CO_2 Conversion

All research involving CO_2 decomposition in plasma has one common task: increasing the energy efficiency associated to the decomposition process, while keeping the dissociation rate at reasonably high level. To understand the difficulties of this reaction, we must introduce two important parameters: α, the conversion rate, that determines the amount of CO_2 that was converted into CO; and η, the energetic efficiency, that quantifies the the ratio between the useful output and input of an energy conversion process.

$$\alpha = \frac{[CO]_{out}}{[CO2]_{in}} \tag{1.4}$$

$$\eta = \frac{\Gamma_{CO} \Delta H_{CO+O}}{P_{in}} \tag{1.5}$$

Where Γ_{CO} is the CO particle flux, ΔH_{CO+O} enthalpy variation of the dissociation process, P_{in} the total power input and $[CO]_{out}$ and $[CO2]_{in}$ the output and input concentrations of CO and CO_2, respectively.

In the most direct way, CO_2 dissociation can be represented by the following reaction:

$$CO_2 \longrightarrow CO + O, \Delta H = 5.5eV/molecule \tag{1.6}$$

The enthalpy variation of the reaction is very considerable, as shown in equation 1.6. However, the atomic oxygen created is able to react with another oxygen atom to form O_2, or it can collide with vibrationally excited CO_2:

$$\mathrm{CO_2}(\nu) + O \longrightarrow CO + O_2, \Delta H = 0.3eV/molecule \tag{1.7}$$

Combining both equations, the process for CO_2 dissociation can be described by:

$$\mathrm{CO_{2(g)}} \longrightarrow \mathrm{CO_{(g)}} + \frac{1}{2}\,\mathrm{O_{2(g)}}, \Delta H = 2.9eV/molecule \tag{1.8}$$

The enthalpy variation of the reaction is very considerable, as shown in equation 1.8. For this reason, CO_2 conversion can be accomplished through thermal conversion, but only at high temperatures ranging from 3000 K to 5000 K [13] .

With thermal CO_2 splitting, according to [13], it is possible to achieve an energetic efficiency of 47%, with a conversion rate of 80% at the temperature range 3000-3500 K. However, because of the high temperatures necessary to achieve this level of efficiency, it is necessary to separate the CO and O_2, to avoid an explosive mixture, using membrane reactor systems. For example, K. Fan et al [14] used a solid oxide ($SrCo_{0.5}FeO_3$) membrane reactor and methane as the sweep gas. At a temperature of 1213 K, it was possible to obtain a conversion rate of up to 10% . However, when the dilution of the feed gas was taken into account,an effective conversion of only 2% was actually reached. Overall, with the use of thermal splitting, at a temperature range of 1200-1900K, which is lower than the optimal temperature, and with semipermeable membranes to extract the oxygen, the conversion rate is around 1% to 2%, which is too low to be feasible for effective industrial use [13].

As discussed before, low temperature plasmas have special properties that stimulate the dissociation of the CO_2 molecule. Electrons will receive a lot of energy from the electric field and distribute it across the plasma's energy states of excitation, ionization, and dissociation.

The energy levels involved in the dissociation of the CO_2 molecule are again depicted in figure 1.6. As discussed in [5] a very efficient way to proceed with this process is through vibration-vibration (VV) up-pumping, which involves a ladder climbing of higher vibrational levels, resulting in the dissociation of the CO_2 molecule. In comparison to direct dissociation, which requires 7.5 eV of energy, this procedure requires only 5.5 eV, making it substantially more efficient. Furthermore, the resultant O atom can collide with another CO_2 molecule, as in, $CO_2 + O \rightarrow CO + O_2$, at an energy of 0.3 eV [1]. The energy required to produce one CO molecule is then reduced to 2.9 eV, only 39 % of the original value.

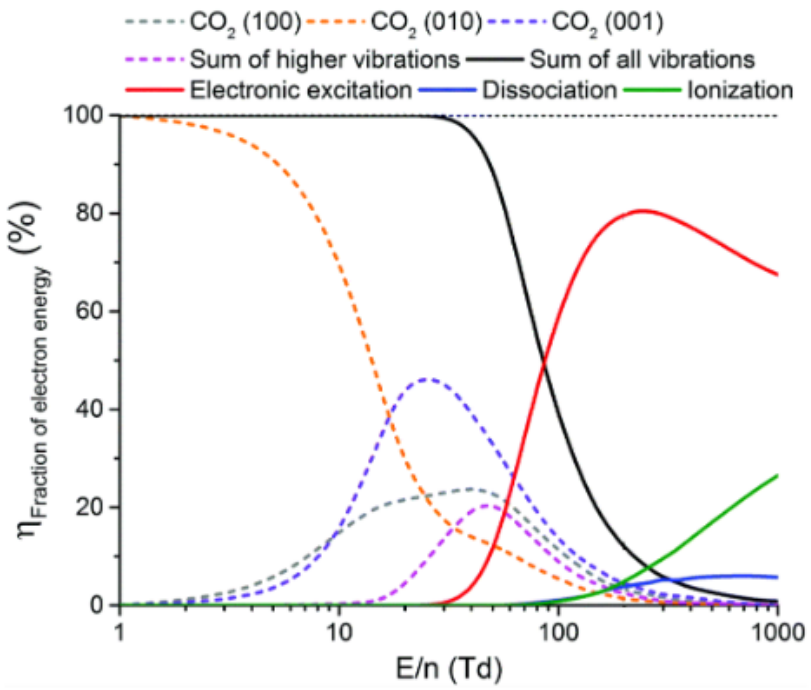

Figure 1.8: Fraction of energy transferred through the different energy channels of CO_2, as a function of the reduced electric field . Taken from [13]

As previously explained, the CO_2 molecule has many excitation contributions that can lead to its dissociation. We can see in 1.8 that this is significantly dependent on the reduced electric field (electric field over gas density). For example, for low E/n ranges (1 to 40 Td), it has been estimated that about 95% of all the discharge energy is transferred from plasma electrons to the vibrations of CO_2 molecules.

In this work, we will go through the significance of the various excitation pathways in order to obtain a more efficient CO_2 conversion.

Another very important process for CO_2 conversion is dry reforming methane (DRM), which converts CH_4 and CO_2 into synthesis gas:

$$\mathrm{CO_{2(g)} + CH_{4(g)} \longrightarrow 2\,CO_{(g)} + H_{2(g)}}, \Delta H = 2.56 ev/molecule \tag{1.9}$$

It is well known that CH_4 is also a greenhouse gas which also needs to be recycled. Just like the CO_2 dissociation, this reaction is highly endothermic, which means that high temperatures ($\approx$ 1000 K), are necessary to have this process run in an efficient manner. Another problem is the fact that a lot of side reactions can be occur, like reverse water-gas shift ($\mathrm{CO_2 + H_2 \rightarrow H_2O + CO}$), the Boudouard reaction ($\mathrm{2CO \rightarrow CO_2 + C}$),and methane cracking ($\mathrm{CH_4 \rightarrow C + 2H_2}$), which promote the creation of carbon deposits that deactivate the catalysts, preventing this reaction from being used in an industrial scale. We will further explore how can plasmas improve this process.

1.5 Thesis Outline

The structure of this master thesis is the following:

In chapter 2, we present the current state of the art of CO_2 kinetic modelling and of plasma applications for the dissociation of CO_2 and dry reforming of methane.

In chapter 3, the experimental part of the work is presented. This includes an overview of the diagnostic techniques used, as well as the different experimental setups and results.

In chapter 4, a complete description of the modelling developed in this work is presented, starting with its theoretical framework and ending with the results obtained for CO_2-CH_4 plasmas.

In chapter 5, the final conclusions and suggestions for future work are given.

Chapter 2

State of the Art

In this chapter we will overview several research topics related to the study CO_2 low temperature discharges, namely kinetic modelling, plasmolysis and plasma reforming with methane. For each topic we discuss the various contributions of this work.

2.1 CO_2 Kinetic Modelling

CO_2 kinetic modelling has been the focus of many works that can be traced back to the 70s. Indeed, already in 1976 [15] studies were showing that showing that electron impact dissociation in plasmas, followed by following molecular electronic excitation is one of the primary dissociation routes for CO_2. In these studies, cross-sections and rate constants were calculated for the dissociation process are given, and an analysis of the effects of vibrational and rotational stimulation on the cross-sections and rate constants of the target molecules was made. More recently, Cenian [16] and [17] illustrates and validates a kinetic model applied to CO_2 dissociation in a low-pressure DC-excited laser. Aerts et al [18] analysed the chemical splitting of CO_2in a dielectric barrier discharge using a chemical reaction set that incorporates the vibrational states of CO_2, O_2, CO.

The work of Aerts et al.[18] was further developed by Kozak et al [19] who included VV, VT, and eV transfers for 25 vibrational states of CO_2, with a focus on the asymmetric vibrational mode, as well as equivalent processes for CO and O_2 - including interactions between these three molecules. By simulating both microwave discharge plasma and atmospheric pressure DBD with this model, the results appear to be in line with earlier experiments.

Finally, it is worth mentioning that the N-PRiME group in Lisbon has been actively contributing to the numerical modelling of CO_2-containing discharges using a step-by-step strategy to validate different aspects of CO_2 chemistry on plasmas. In particular, previous modelling research works were focused on the: (i) study of the time-resolved evolution of the lower vibrationally excited CO_2 levels during the afterglow of CO_2 discharges [20]; (ii) investigation of the effect of electrons on the distribution of the lower vibrationally excited CO_2 levels in pulsed and continuous glow discharges [21]; (iii) investigation of the influence of N_2 on the CO_2 vibrational distribution function and dissociation yield in pulsed glow discharges [22]; (iv) validation of the electron-impact dissociation cross sections of CO_2 [23]; (v) studying of the gas heating in the afterglow of glow discharges and to proposing a reaction mechanism to predict the formation of dissociation products in CO_2 [24].

In this work we follow this step-by-step modelling strategy by advancing towards the development of a reaction mechanism that takes into account CO_2-CH_4 mixtures. All the details related to kinetic modelling and new features regarding cross sections and rate coefficients will be described in detail in

chapter 4.

2.2 Plasmolysis - Experimental Studies

Plasma-based dissociation of CO_2 is a topic that has been experimentally studied in detail for more than 40 years. In this context, it is worth mentioning that earlier results obtained in the Sovietic Union [25], [26] gave highly promising results, in the context of CO_2 dissociation under a non-equilibrium microwave discharge. Under supersonic expansion gas conditions, these studies revealed an energy efficiency of 80% - 90%. These remarkable levels of energetic efficiency, however, have not been replicated to this day, since the highest energy efficiency values recently reported are around 50–60 % [27]

More recently, many studies have relied on microwave plasmas to maximize the conversion of CO_2 ([28], [29], [30], [31]). In 2014, Silva et all [29] studied the plasma-based CO_2 conversion in a flowing gas surfaguide pulsed microwave discharge under various conditions using CO_2 and CO_2 + N_2 gas mixtures. It was possible to achieve values for the dissociation rate of about 80 %, while keeping the energetic efficiency at $\approx 20\%$. On the other hand, in 2016, Bongers [28] presented the results of CO_2 dissociation in a vortex-stabilized microwave plasma reactor, studying the effect of the microwave field, residence time, quenching, and vortex configuration on the energy - and conversion efficiency of CO_2 dissociation. Here it was possible to achieve energy efficiency values for η at almost 50%, while keeping a low conversion rate.

Overall, and despite recent improvements, the levels of efficiency indicated in the late 1970s have not been achieved, and additional research is required to increase the possibilities of future industrial application.

To further explore this topic, the present work will address the potential of plasmas to create hydrocarbons from CO_2-CH_4 mixtures, while analyzing several parameters that influence the energy efficiency of CO_2 conversion. This work will explore the possibility of measuring plasma parameters like gas temperature and the reduced electric field through optical emission spectroscopy, which is one of the most straightforward diagnostic techniques for this type of plasma.

2.3 Plasma applications in Dry Reforming of Methane

We will now analyse the state of the art of Dry Reforming of Methane (DRM), using different types of plasma reactors for this process. With regards to Dielectric Barrier Discharges, Wang [32] investigated the effect of commercial catalyst Ni/Al2O3 with a DBD plasma in the dry reforming of methane with a coaxial DBD reactor. Different spacial distributions for the catalyst were studied. It was possible to obtain levels of conversion of 60 % for CO_2 and 40 % for CH_4, and a very high selectivity. However, Snoeckx in [33], studied the energetic efficiency of the process, with different configurations, and concluded that the maximum theoretical energy efficiency was between 11.4 % and 15.1 %. This is a a very low value compared to desired value of 60 %, which means DBD is not suited for industrial use, although it is very useful setup to understand the fundamental processes that occur in the plasma.

In another important study [34], the performance of DRM was studied in a Self-triggered spark reactor. Here, it was possible to achieve a conversion rate of 71% for CH_4 and 65% for CO_2, with selectivity of 78% for H2 and 86% for CO, and conversion ability of 2.3 mmol/kJ. The byproducts of the reaction were also studied, and the optimal ratio of CO_2:CH_4 was found to be 1, given the reduction of water production,while improving the stability of the discharge.

Regarding the nanosecond repetitively pulsed discharges (NPDs), it is worth mentioning the very recent work of Montesano et al [35] . It was shown that it is possible to achieve a conversion rate between

40 % and 50 % for CH_4 and CO_2 and an energetic efficiency between 50 and 65 %. It was also shown that plasma-pulse parameters can have a very positive influence on energy efficiency parameters.

Another promising experimental setup is the atmospheric pressure glow discharge plasmas (APGLD). In [36], the dry methane reforming was studied using this setup and it was possible to achieve a conversion of 98.52 % and 90.3 % of CH_4 and CO_2 respectively. Furthermore, the highest conversion ability was of 12.21 mmol/kJ. In this work, to further explore the topic of CH_4 reforming, we will experimentally investigate DC glow discharges sustained with CO_2-CH_4 mixtures. In particular, we will study the influence of plasma parameters to the production of various hydrocarbons. A modeling and experimental investigation will be carried out: On one hand, we'll use experimental measurements and the FTIR technique to investigate the chemical composition of the plasma. On the other hand, a kinetic model will be developed to simulate plasma behavior under various conditions and to determine the most significant mechanisms of molecule creation and annihilation. All details can be found in chapter 3

Chapter 3

Plasma Diagnostics and experimental results

3.1 Gas Discharges

Gas discharges are physical basis of the many of the setups in which non-thermal plasmas are created. An electric discharge can be thought of as two electrodes placed inside a glass tube and linked to a power supply. At a specific voltage necessary for sufficiently intense electron avalanches, the current suddenly climbs quickly as the voltage applied across the two electrodes increases. When the pressure is low, on the order of a few Torrs, and the external circuit has a high resistance to prevent a significant current from flowing, a glow discharge occurs. This is the major experimental setup for this work, and it is explored in more detail in the next section.

There are other important types of electric discharges. A corona discharge occurs only in regions with severely non-uniform electric fields at high pressures [1]. Typically, the electric field in one of the electrodes is much greater. This can happen very frequently, because if a charged object has a sharp point, the electric field strength around that point will be much higher than elsewhere. If the voltage is high enough, the ionization of its surroundings (for example, air) will occur, and it will become conductive. This process can happen at an atmospheric process and it has a number of commercial and industrial applications like, for example, removing unnecessary electric charges from an aircraft's surface while in flight.

Very similarly to corona discharges, arc discharges can also occur at an atmospheric pressure. In this case, there are usually two electrodes with a very high electric field, and a low conducting medium, like air, separating them. With a sufficiently high voltage, the air will be totally ionized, and an arc between the electrodes will be formed, where conduction occurs. Arc discharges have been used for a long time, since in the late 1800s, electric arc lighting was in wide use for public lighting.

Finally, it is also important refer low-pressure radio-frequency discharges, where a non-equilibrium plasma is generated when an electric wave with a very high frequency passes through a given medium, and electrons are energized by it. This type of plasma has very interesting properties, like its high energetic efficiency and scalability potential, which are very important for large scale and industrial implementations ([37], [38]).

3.1.1 DC Glow discharge

When a high enough voltage is applied to a charged anode and cathode, a glow discharge occurs. The cathode releases electrons as a result of bombardment by positive ions, and the glow discharge gets its name from the characteristic light emission. In figure 3.1 we can see a representation of the structure of the Glow discharge plasma.

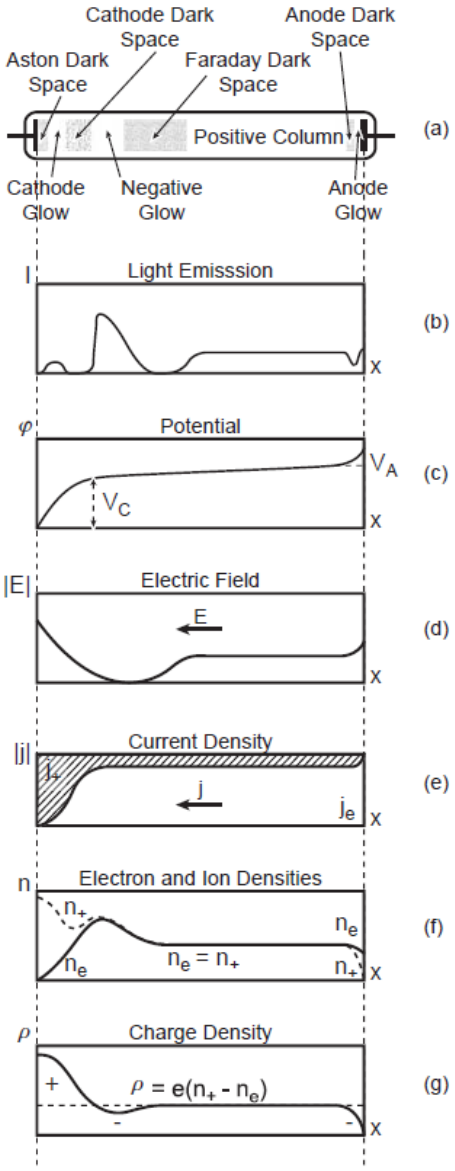

Figure 3.1: Schematic representation of glow discharge and of its physical parameters. From [1]

In these discharges, a cathode and anode are permanently fixed to a gas chamber. Once a sufficient potential difference is attained, electron and ion densities are amplified in a manner similar to avalanche breakdown, until the entire chamber is filled with positive and negative ions and electrons, thus forming a plasma. In this case, the electrons gain sufficient energy to ionize the neutral particles. However, if this voltage is too high, the electrons will avoid colliding with neutrals and there will be no plasma. It is then necessary to chose a voltage close to the breakdown voltage, V_B, given by the semi-empirical

Paschen's law.

$$V_B = \frac{Bpd}{ln(Apd) - ln(ln(1 + \frac{1}{\gamma}))} \tag{3.1}$$

where d is the distance between the electrodes, p the pressure, γ the secondary emission coefficient and A and B determined experimentally and depend on the gas composition.

As it can be seen in figure 3.1, the glow discharge has very distinct areas, alternating between light and dark zones, whose size is dependent on the specific parameters of the experiment. In this work, with $p \approx 1Torr$ and $d \approx 50cm$, the tube is going to be filled with the positive column, which facilitates our work, since it is highly homogeneous. However, at lower pressures, striations will appear in the tube, creating a problem because the light emitted will not be as homogeneous as before. We shall discuss this issue further, however in order to fix it, we will apply a diffuser when collecting experimental data.

3.2 Diagnostic Techniques

Plasma diagnostics are a collection of methodologies, tools, and experimental techniques used to evaluate plasma characteristics such as density, temperature, spatial distributions, from which plasma parameters can be derived. In this section, we will explore which diagnostic techniques were used throughout this work. First we describe optical emission spectroscopy (OES) and its potential for temperature measurements in plasmas. OES will also be used to analyze the broadband emission associated to the chemiluminescence from recombination of CO and O. After, we present the Fourier-transform infrared spectroscopy (FTIR) techniques, that were used to obtain the chemical composition of the plasma.

3.2.1 Optical Emission Spectroscopy

OES is a non-intrusive optical technique that relies on the light produced by the relaxation of excited species in plasma. Because of its ease of use and great sensitivity, this method is perhaps the most commonly utilized diagnostic in plasmas. OES is a line-of-sight measuring approach, that usually averages data along a specific plasma area. It is a qualitative way of measuring the plasma composition and it allows for several species to be detected at the same time. It can be used as a quantitative approach [39], provided that a proper population model associated to the emitted species is known. To characterize the emission spectrum obtained in OES, the following intensity equation can be used [39]:

$$I(p,q) = \frac{h\upsilon_{pq}}{4\pi} n(p) A(p,q) l \tag{3.2}$$

where $I(p,q)$ is the intensity line of the state transition $p \rightarrow q$, $h\upsilon_{pq}$ is the energy difference between the p and q state, p is the most energetic level , $n(p)$ the density of the q state, $A(p,q)$ the transition probability and l the line-segment of the plasma along which radiation is collected. The OES setup is used in this work will be described in section 3.3.1.

3.2.2 Rotational Temperature Fit - CO Angstrom rotational band

Gas temperature measurements in plasmas through rotational temperature (obtained from rotational spectra using OES) is a very common method provided that translational-rotational equilibrium exists. This method has been used in many molecular systems, like N_2, OH, CO, etc and a general overview of the method for different systems is given in [40]. In this section we will provide the details required to fit the emission spectrum of the rotational band of CO to quantify the gas temperature in the plasma.

More specifically, we apply this method to the CO Angstrom rotational band associated to the vibrational transition vi = 0 $\rightarrow$ vf = 1. This method has been used in the works of Silva at al in [41] and Du et al in[42]. The intensity distribution I_{rot} in a rotational emission band, associated to the vibrational translation between v_i and v_j, assuming a Boltzmann distribution, is given by [43] :

$$I_{rot} = \frac{C_{rot} S_{J_i J_j}}{Q_{rot} \lambda^4_{J_i J_j}} exp\left(-\frac{F(J_i)hc}{k_B T_{rot}}\right) \tag{3.3}$$

where C_{rot} is a constant that combines all the terms not dependent on J states, Q_{rot} the statistical sum, $S_{J_i J_j}$ the Hönl-London factor (taken from [42]) and $\lambda_{J_i J_j}$ the transition wavelength, $F(J_i)$ the rotational energy term and h,the Planck constant, k_B the Boltzmann constant and c the speed of light, $F(J)$ given by:

$$F(J) = B_v J(J+1) - D_v J^2 (J+1)^2 \tag{3.4}$$

Where B_v and D_v where:

$$B_v = B_e - \alpha_e(v + 0.5) \tag{3.5}$$

$$D_v = D_e - \beta_e(v + 0.5) \tag{3.6}$$

where B_e, α_e, D_e and β_e are rotational constants (taken in this work from [42]) , defined for the vibrational level v. Note that for the CO Angstrom rotational band, (CO $(B^1\Sigma)(v_i = 0) \rightarrow \mathrm{CO}(A^1\Pi)(v_j = 1)$, it is necessary to sum three different branches: P, Q and R, which correspond to $\Delta J = J_i - J_j = -1, 0 + 1$. For more details, see [40]. In addition, to reflect the broadening of the spectral lines, a pseudo-Voigt distribution ([41], [42]), i.e., a combination of a Gaussian and a Lorentzian function, was used according to:

$$V(\lambda) = G(\lambda, W_G) \otimes L(\lambda, W_L) \tag{3.7}$$

where G and L are the gaussian and lorenzian distributions and W_G and W_L the corresponding full width at half maximum (FWHM). With the intensity spectrum $I(\lambda, W_G, W_L, T_{rot})$ calculated, and using the λ as the independent variable, a fitting script, we developed a MATALB fitting script that takes into account the experimental emission spectra to determine the rotational temperature. An example of the emission spectrum of the CO angstrom rotational band that will be fitted is given in figure 3.2. The results are provided later in 3.3.3.

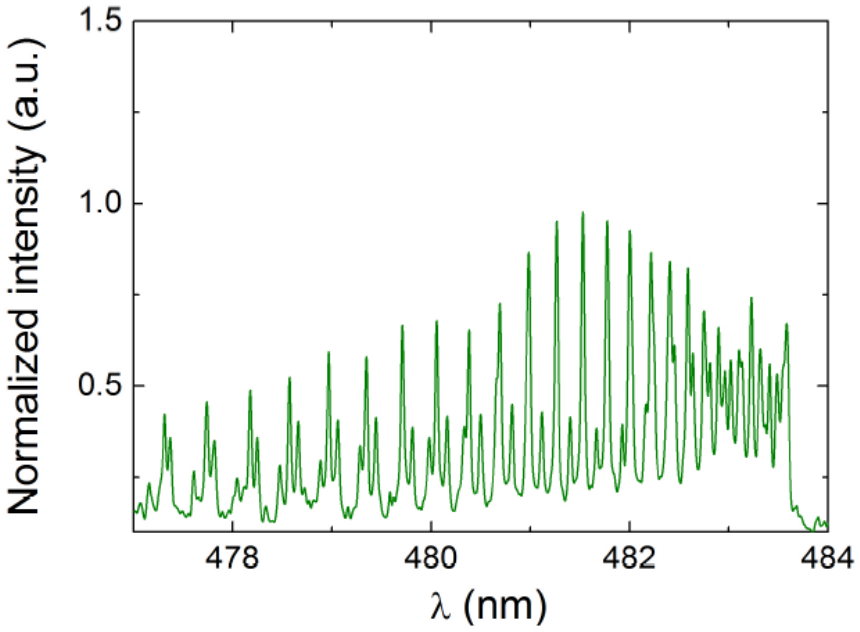

Figure 3.2: Emission spectrum of the CO Angstrom band. Adapted from [41]

3.2.3 FTIR spectroscopy

Infrared Spectroscopy consists essentially in the study of the interaction of infrared light with matter. This can be achieved through an Infrared Spectrometer.Using IR absorption spectroscopy it is possible to determine with a high accuracy the density of the plasma species and its vibrational states. In this work, we apply the FTIR in the positive column of the glow discharge to study the the chemical composition of the plasma.

Using a polychromatic beam of incident light that shined at a sample, information is extracted using interference with the same polychromatic beam with a phase difference. From this process it will result an interferogram, which then can be subjected to a Fourier transform and a spectrum of the intensity of the beam, as a function of its wavelength, will be obtained.

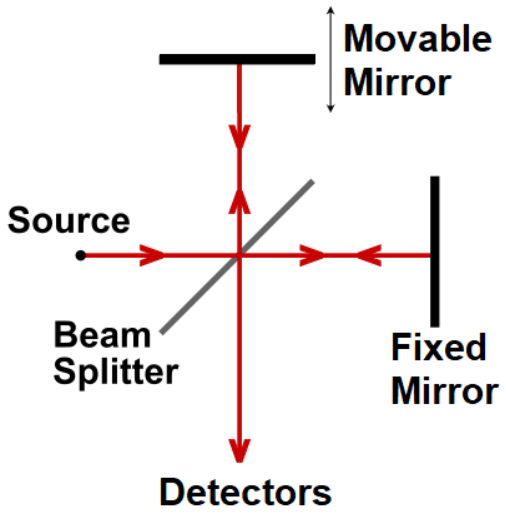

Figure 3.3: Interferometer used for FTIR.

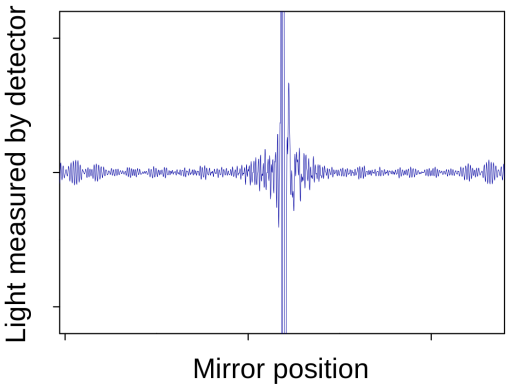

Figure 3.4: Interferogram obtained from the interferometer.

In figure 3.3, the scheme of an interferometer utilized for FTIR is represented. The interferometer is made up of two perpendicular plane mirrors, one of which is fixed and the other which may be moved. A beamsplitter is used to separate the incoming laser beam and send it down two distinct paths to each mirror, where it will be reflected. Interference will occur when the two beams of light recombine owing to their differing lengths, and the resultant laser beam will proceed towards the detector. With these experiment, one can now obtain the transmitance spectrum, with the contributions from the plasma.

$$T = \frac{I}{I_0} = \frac{I_t - I_{plasma}}{I_0} \tag{3.8}$$

Where I_0 is the background emission, taken before the plasma is turned on, I is the intensity spectrum, which depends on the intensity I_{plasma} of the plasma radiation and I_t, which is the intensity measured after the beam has travelled through the interferometer. The transmittance is then heavily dependent on the plasma parameters. Considering the Beer-Lambert law, we have:

$$-ln(T) = \int_0^{+\infty} \mu(z)dz \tag{3.9}$$

where z is the depth into the sample and μ_z the absorption coefficient, given by:

$$\mu(z) = n(z)\sigma \tag{3.10}$$

where n(z) is the density of attenuating species and σ the attenuation cross section. It is then easy to see that it is possible to obtain parameters like the density of the different species of the plasma, by fitting the transmittance spectrum that was measured. However, there are some species whose density is not measurable through this method, like O_2, O, H_2 and H.

3.2.3.1 Fitting Algorithm

To extract information from the measured spectrum with the FTIR techniques, a fitting algorithm was used. This procedure was based on the algorithm developed by Klarenaar et al [10] and the later adaptations done by in the master thesis of H.Rodriges [44].

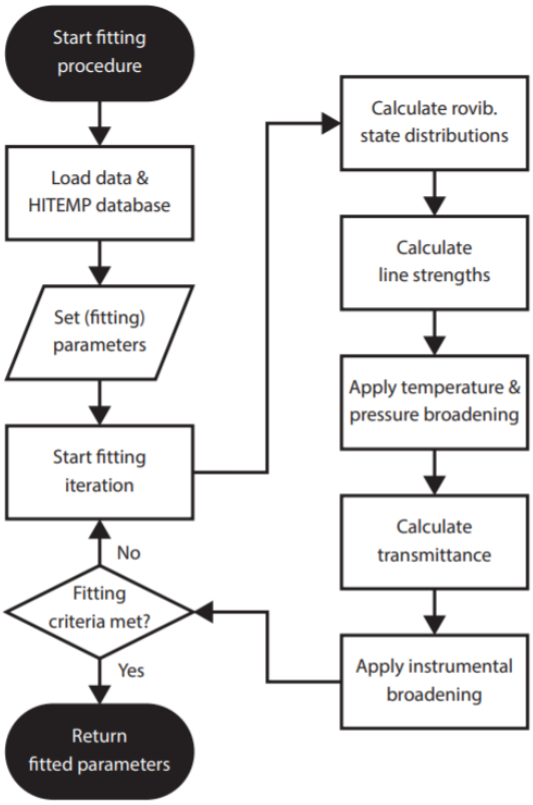

Figure 3.5: Flowchart of the original algorithm from [10]

In figure 3.5 a flowchart of the algorithm developed by Klarenaar is shown. It considers the region where $\nu \in [1975, 2400]cm^{-}1$ and fits CO and CO_2 vibrational lines. In [44], H. Rodrigues further developed the algorithm to extend the frequency region to $[1000, 4000]cm^{-}1$, and to fit the densities of the plasma, instead of the α parameter (conversion rate, defined in equation 1.4). Additional extensions also took into account the presence of species formed as a result of decomposition of CO_2 and CH_4, namely the ones that are present in CO_2-CH_4 plasmas. The fundamental procedure to fit the transmittance spectrum is the following: First, we consider the gas thermalized and a Boltzmann distribution for the states of the molecules is used. The fitting parameters will then be the gas temperature T_g, the pressure and the different molecules concentration. Secondly, with the distribution of states defined, the line strength S_k is calculated, for each different transition of state in the molecule. This is done with the data in the HITRAN database. Then, it is possible using the Beer-Lambert law to calculate the transmittance, assuming an homogenious medium with length L, composed of several different absorbers, for a frequency ν:

$$T(\nu) = \prod_{j}^{j_{max}} e^{-Ln_j \sum_{i_1}^{i_{max}(j)} \sigma_i(\mu)} \tag{3.11}$$

where n_j is the density of the species, σ_i the cross section for a specific line, the product is done over all of the absorber species and the sum over the different transitions that contribute to the given frequency. The Voigt function is used for the cross section, and it takes into account the various types of broadening that occur, like the Doppler broadening and the collisional broadening.

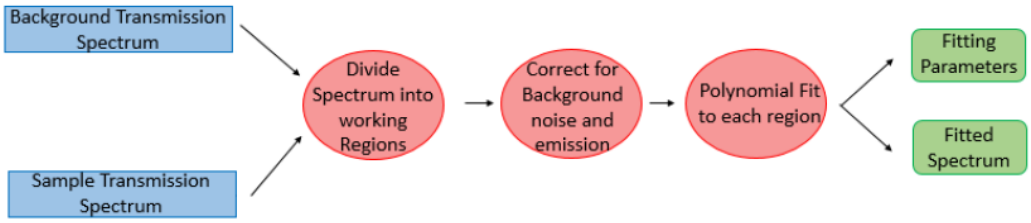

Figure 3.6: Flowchart of the fitting algorithm. Adapted from [44]

Finally, flowchart in figure 3.6 represents the final algorithm used to fit the full spectrum. Unlike the original algorithm, this one will take into account all the molecules present in table 3.1. Furthermore, as mentioned before, it covers the region of $\nu \in [1000, 4000] cm^{-}1$, because it dives the full spectrum into separate sub-regions, that are fitted separately. The continuity between the functions is imposed. Lastly, a threshold of noise is introduced, due to the presence of H_2O species. This facilitates the fit in noisy regions, but at the cost of ignoring some of the smaller peaks, which is not a serious problem, since they contribute very little for the final density calculation.

Molecules		
CO_2	CO	CH_4
C_2H_2	H_2O	C_2H_6
C_2H_4		

Table 3.1: Molecules included in the fitting algorithm

3.3 Optical emission Spectroscopy - Experimental Results

3.3.1 General Considerations

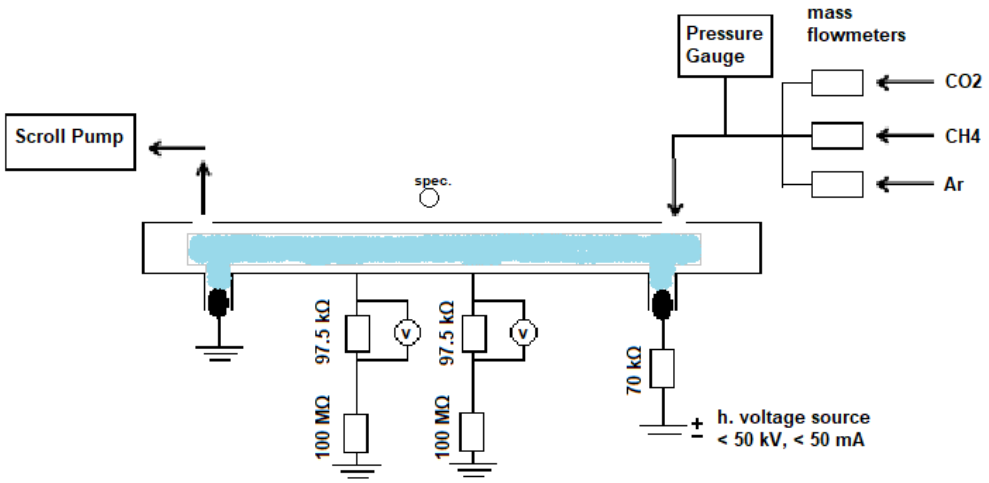

Figure 3.7: Experimental setup for the optical emission spectroscopy measurements.

In this section we will analyze the results related to optical emission spectroscopy. In particular we will analyze the potential of the Angstrom band to measure gas temperature and the applicability of broad-

band acquisition to quantify the reduced electric field of the discharge. The experimental measurements made using OES shared the same experimental setup, that is shown in figure 3.7. The pressure in the tube was varied between 0.5 and 5 Torr and the total gas flow was varied between 7.79 and 7.88 sccm, using gas from bottles of pure CO_2, CH_4 and Ar. A small amount of Ar was present in the mixture and the objective of this was to reuse some of the previous experimental work done in the same conditions. For example, the gas temperatures measurements made in [45] were used to calculate the gas density in this work. The pressure was measured with a capacitance manometer , and the gas was evacuated by a scroll pump through a pressure-regulating valve. The discharge current was varied between 10 and 50 mA. All measurements were taken at the axial centre of the positive column of the glow discharge; radial gradients in the electric field were therefore not taken into account. The following points were taken into account throughout the measurement procedure:

- Two different spectrometers were used in throughout the measures: a USB spectrometer, the Maya 2000 that allowed for a wide range spectrum, where $\lambda \in [200, 900]nm$ and a most precise spectrometer, where the $\lambda \in [474, 484]$. Two different spectrometers were used to measure emission spectra: a low resolution USB spectrometer Maya 2000 that allowed for a wide range spectrum ($\lambda \in [200, 900]nm$), used for the broadband measures and a high resolution spectrometer ($\lambda \in [474, 484]$) which guaranteed the measurements of the rotational structure of CO Angstrom band

- The calibration of the USB spectrometer, together with the used optical fibers used, was made using a light source which the emission spectrum was known. Then, the USB spectrometer was used to measure the emission spectrum, a ratio between the measured and the expected intensity values was calculated, for every wavelength value. These correction values were used every measurement, to correct the intensity spectrum obtained.

- The intensity spectrums acquired using the USB spectrometer (including in the calibration) always included an average of 20 acquisitions, in order to eliminate any possible time fluctuations in the intensity values. Furthermore, the acquisition time for each measure was between 300 and 1600 ms.

- Before each acquisition of the plasma spectrum, the background spectrum was also taken, with the plasma turned off, and later, this background intensity was always subtracted to the intensity spectrum obtained, with the plasma turned on.

- For low pressure conditions (bbelow 1 torr), the plasma was not homogeneous throughout the reactor any more. In fact, plasma striations appeared, leading to consecutive bright and dark areas. To increase the homogeneity of the diffusion, we used diffusion filters. The effect on the light intensity was measured, using the same light source with and without the diffusion filter. It was found that the intensity measured with the diffuser, followed the expression: $I_{\text{diff}} \approx 0.4 I_{\text{no diff}}$. This correction was applied whenever plasma striations appeared.

3.3.2 Broadband study

The emission spectra analyzed in this work are characterized not only by the characteristics bands of CO_2, CO and atomic oxygen lines, but also by a continuum-like shape as a result of the recombination of CO + O. This continuum was observed between 250 and 800 nm with a maximum intensity around 500 nm (see figure 3.8)

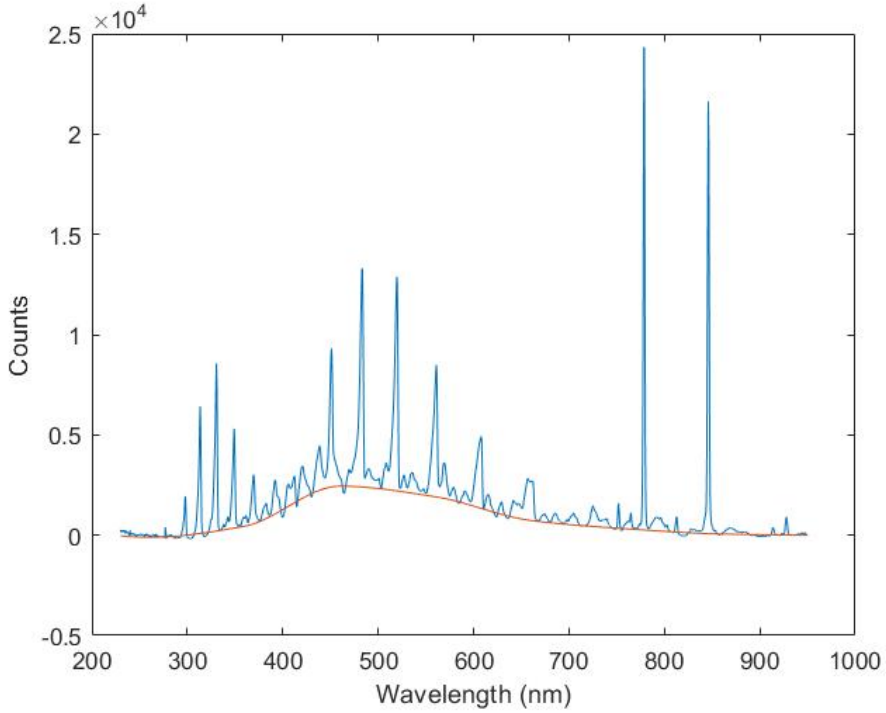

Figure 3.8: Intensity spectrum measured for a DC glow discharge plasma with current of 40 mA, pressure of 3 Torr, and with gas composition of input flow of 7.40 sccm of CO_2 and 0.39 sccm of Ar.

One hypothesis to explain this emission is the process of CO + O chemiluminescence reaction:

$$\mathrm{CO} + \mathrm{O} \rightarrow \mathrm{CO_2} + h\upsilon \tag{3.12}$$

To explain the emission of this process we can consider the following chemical reactions:

$$\mathrm{CO} + \mathrm{O} + M \rightarrow \mathrm{CO_2}(^3B_2) + M \tag{3.13}$$

$$\mathrm{CO_2}(^3B_2) \rightarrow \mathrm{CO_2}(^1B_2) \tag{3.14}$$

$$\mathrm{CO_2}(^1B_2) \rightarrow \mathrm{CO_2}(^1\Sigma_g^+) + h\upsilon \tag{3.15}$$

$$\mathrm{CO_2}(^3B_2) + M \rightarrow \mathrm{CO_2}(^1\Sigma_g^+) + M \tag{3.16}$$

From the balance equation in steady state associated to the $\mathrm{CO_2}(^3B_2)$ excited molecule (see Slack for more details [46]) we can see that the the broadband emission becomes proportional to the concentration of CO and O according to the following expression, the intensity of the broadband emission is given by equation 3.17:

$$I = I_0[\mathrm{CO}][\mathrm{O}] = I_O N^2 f_{\mathrm{CO}} f_O \tag{3.17}$$

Where $[CO]$ and $[O]$ are the concentrations of CO and O species, N is the gas density, and f_{CO} and f_O are respectively, the fraction of the CO and O molecules in the plasma, respectively. The quantity I_0

can be experimentally obtained. In [46] the authors showed that I_0 can be written according to:

$$I_0 = 6.8(\pm 0.6) \cdot 10^5 exp(-1960/T_g)\ (cm^3 mole^{-1} s^{-1}) \tag{3.18}$$

Provided that the broadband is explained by the mechanisms proposed in Slack [46], one could expect the total broadband emission to follow the trend described by 3.18. To explore this hypothesis we have calculated the intensity of the broadband emission as function of the gas temperature. To this purpose, we have started by calculating the baseline of the measured spectrum. A matlab script was developed to calculate the baseline (see red line in figure 3.8) using the using the "msbackadj" function, from the Bioinformatics Toolbox. Then the total spectrum intensity was determined through the calculation of the integral of the baseline over the full wavelength range. Figure 3.9 shows evolution of the intensity of the broadband continuum as a function of the gas temperature.

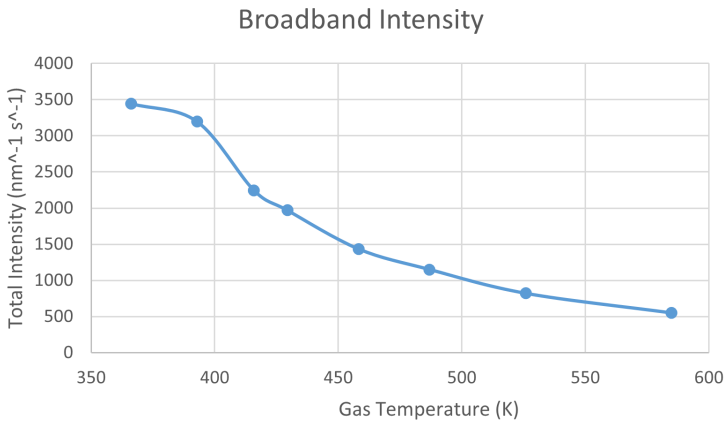

Figure 3.9: Variation of the broadband intensity with gas temperature, measured for a DC glow discharge plasma with current of 40 mA, and with gas composition of input flow of 7.40 sccm of CO_2 and 0.39 sccm of Ar.

The gas temperature indicated in figure 3.9 was previously measured in [45]. We can see that the emission intensity exponentially decreases with the gas temperature, which is the opposite of what is predicted by equations 3.17 and 3.18. Note that the total density of the plasma is also increasing, considering that for T_{gas} = 366 K (first point in figure 3.9) we have a gas density of $8.3 \cdot 10^{21} m^{-3}$, while for T_{gas} = 584.9 K (last point in figure 3.9) we have a gas density of $8.1 \cdot 10^{22} m^{-3}$. Finally, even though the fractions of CO and O change with the gas temperature, this variation is residual compared to the change in I_O and N. Using results from previous experiments [45], it was possible to conclude that the variation of f_{CO} was only about 3 %. We can conclude that the mechanism proposed by Slack in [46] is not suited to describe the data observed in this work.

To further explore the discrepancy between the experimental results and expression 3.17 we will now analyze the effect of electron excitation associated to creation of the $\mathrm{CO_2}(^3B_2)$. As discussed in chapter (see figure 1.8), when the reduced increase, there is also an increasing contribution of energy transferred directly to the electronic excited states of CO_2. It is also worth noticing that the range of reduced electric field that characterize the experimental setup used in this work (30-100 Td) are likely to promote CO_2 electronic excitation. To analyze the creation of $\mathrm{CO_2}(^3B_2)$ via electron impact, and following [1], we start by considering the following rate coefficient for electronic excitation between two energetic levels i and k (assuming a Maxwellian distrubution):

$$k_{el}\ \alpha\ exp\left(-\frac{\Delta E_{ik}}{T_e}\right) \tag{3.19}$$

where ΔE_{ik} is the energetic difference between the states i and k, and T_e is the electron temperature. Considering that the electron temperature is proportional to the change in reduced electric field, we can now propose an expression for the intensity measured. This approximation is very similar to the one used by Guerra et al [47] :

$$k_{el} = a \cdot exp\left(-\frac{c_{el}}{(E/N)}\right) \tag{3.20}$$

$$I = k_{el}[\mathrm{CO_2}] \tag{3.21}$$

$$log_{10}\left(\frac{I}{[\mathrm{CO_2}]}\right) = -\frac{c_{el}}{(E/N)} + b \tag{3.22}$$

where a and b are constant values, (E/N) is the reduced electric field, and c_{el} is a constant value related to the reduced electric field necessary to electronically excite CO_2. Expression 3.22 was used to analyze the relation between E/N with the broadband emission, for various conditions of discharge current and gas flow 3.2:

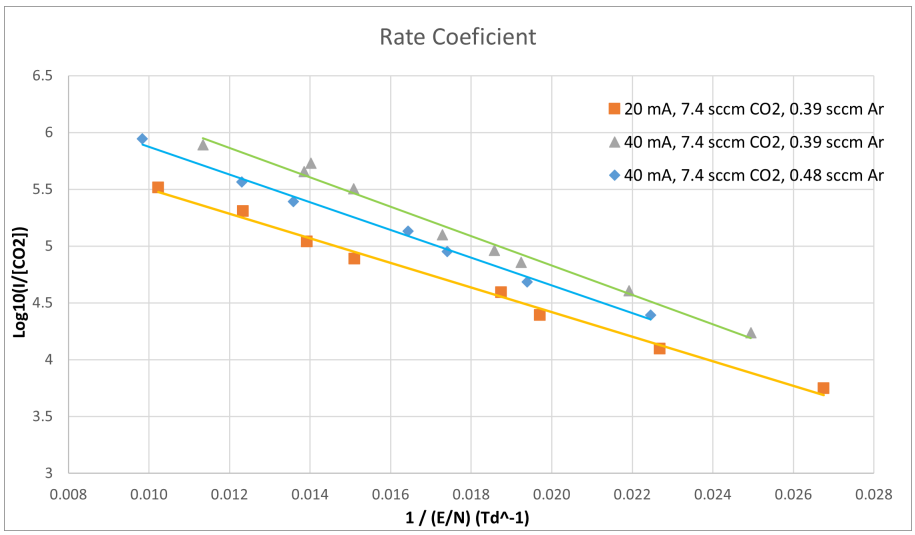

Figure 3.10: Variation of the logarithm of broadband intensity divided by the CO_2 concentration, measured for different gas mixtures (CO_2, and Ar), as a function of the reduced electric field.

Current (mA)	CO_2 Flow (sccm)	CH_4 Flow (sccm)	Ar Flow (sccm)	b	c_{el} (Td)
20	7.40	0	0.39	6.59	108.28
40	7.40	0	0.39	7.42	129.3
40	7.40	0	0.48	7.10	122.1
40	3.70	3.70	0.43	7.02	127.2
40	6.66	0.74	0.43	6.80	112.5
40	7.03	0.37	0.43	6.49	92.6

Table 3.2: Parameters obtained from the fits in figures 3.10 and 3.11. The medium and the standard deviation of the b and c_{el} values are the following: $\overline{c_{el}}$=115.33 Td, $\sigma_{c_{el}}$=13.83 Td. $\overline{b}$=6.90, σ_b =0.05

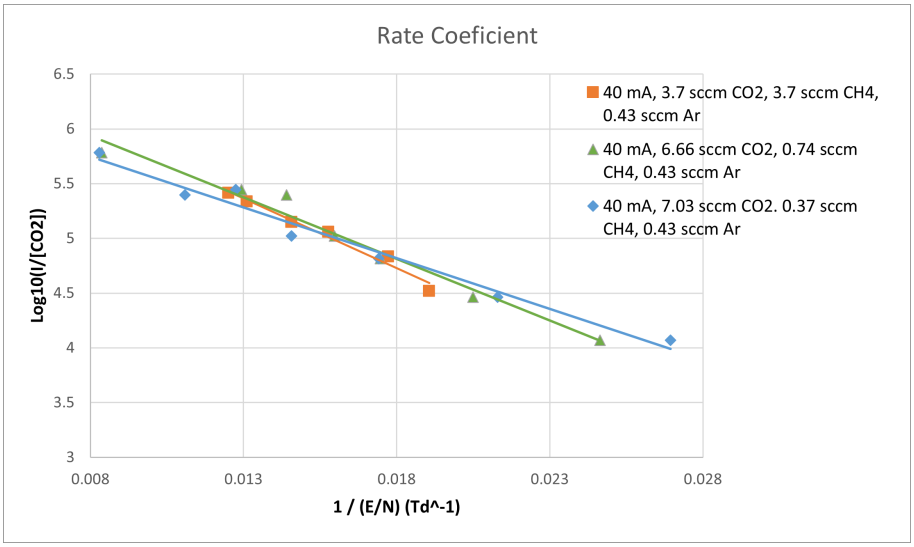

Figure 3.11: Variation of the logarithm of broadband intensity divided by the CO_2 concentration, measured for different gas mixtures (CO_2, CH_4 and Ar) as a function of the reduced electric field.

The results show a clear dependence of the intensity of the broadband emission on the electronic excitation of the CO_2 molecule. From figures 3.10 and 3.11, we can observe linear linear dependence of the broadband emission with the quantity 1/(E/N), from which we can conclude that the reduced electric field and the CO_2 concentration are the main parameters that determine the intensity of this emission. Furthermore the decrease of intensity with the increase of the gas temperature, as previously seen, can be explained by the decrease in the reduced electric field. In relation to the values of b and c_{el} we see that they present some dependence with plasma conditions given their evolution with current and flow rates (see table 3.2).

Overall, the method developed in this section offers an easy-to-handle solution if quick reduced electric field measurements are required in CO_2 discharges, provided access to the broadband emission. Note, however, that the applicability of the proposed method is always dependent of mechanisms that can influence the creation and loss of electronic excited states of CO_2 , namely $\mathrm{CO}_2(^3B_2)$. This approach should be further studied and validated in future works. In particular, next studies should analyze the dependence of b and c_{el} constants with the plasma conditions (e.g. discharge current and flow rate).

3.3.3 Gas temperature measurements

In this section we analyze the gas temperature obtained from the fitting of the CO Angstrom system. Spectra with different initial gas compositions were analyzed. In this analyses, the combined flow of CO_2 and CH_4 was always 7.40 sccm with a small amount of Ar (0.43 sccm). The relative amounts of CO_2 and CH_4 were changed for different sets of measures. Furthermore, the pressure and current

values were also varied in the range of 0.5 and 5 Torr and 10 and 50 mA, respectively.

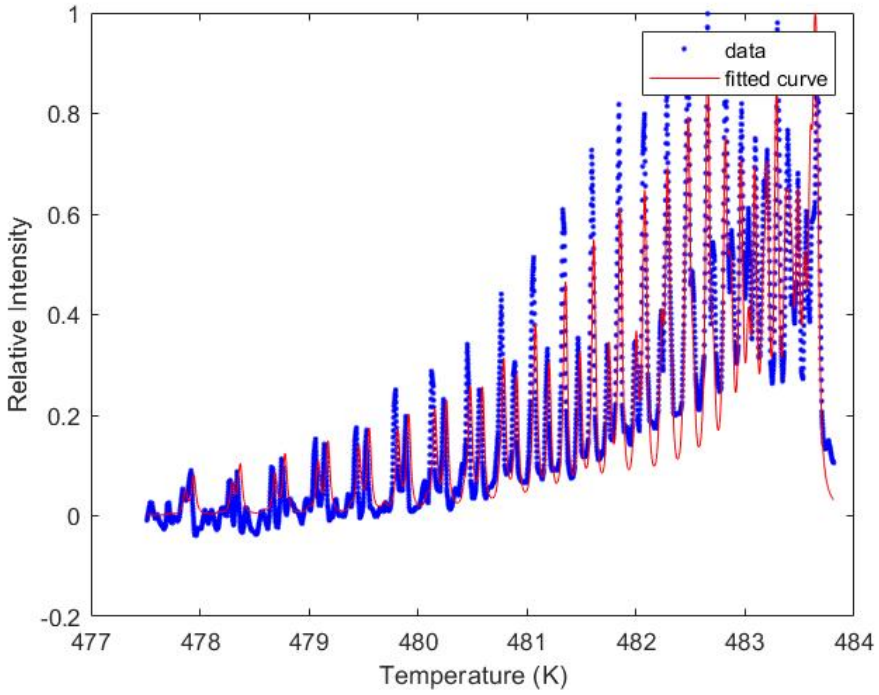

Figure 3.12: CO rotational emission band and the corresponding fit, with input flow of 7.03 sccm of CO_2 and 0.37 sccm if CH_4, pressure at 1.5 Torr and current of 40 mA.

Figure 3.12 shows an example of the experimental data obtained for the CO rotational emission Angstrom band and the corresponding fitting spectrum. We can now apply the fitting procedure for different conditions of current, pressure and gas mixture:

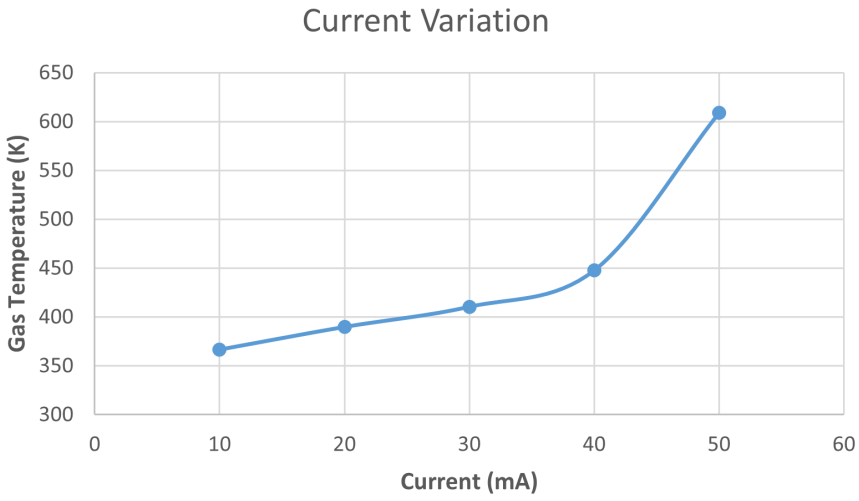

Figure 3.13: Variation of the gas temperature with current, measured for a DC glow discharge plasma with pressure of 3 Torr, and with with input flow of 3.70 sccm of CO_2 and 3.70 sccm of CH_4.

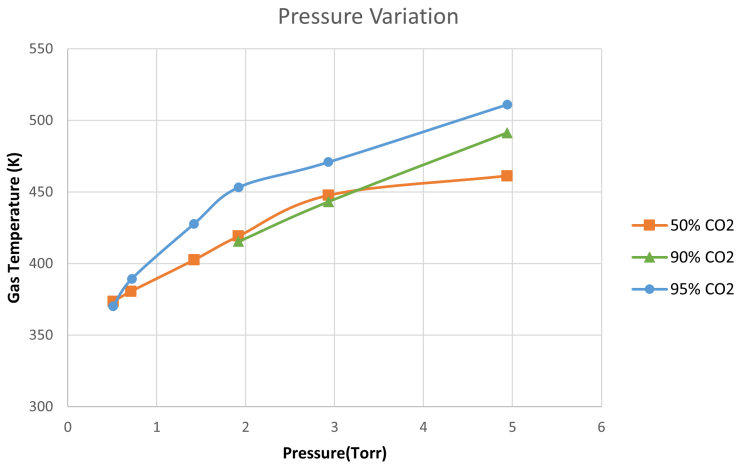

Figure 3.14: Variation of the gas temperature with pressure, for a DC glow discharge plasma with a current of 40 mA, and varying input flows.

In figure 3.13 we see the variation of the gas temperature with discharge current. As expected we observe an increase of the gas temperature with the discharge current, which is particularly strong from 40 to 50 mA. In figure 3.14 shows the variation of the gas temperature with the gas pressure. We can see that the temperature also increases with the growth of the pressure. Finally, the temperature also has an increasing trend with the amount of CO_2 present in the initial mixture.

These results are consistent with the measurements that were made in the PhD thesis of A. S. Morillo-Candas in [45], in which the gas temperature was measured in CO_2 plasmas (but without CH_4), and also increased with the current and pressure values. Note that in [45] the gas temperature was obtained through FTIR measurments. In this work we have demonstrated that OES also offers an easy-to-handle solution if T_{gas} measurements are required in CO_2 discharges, provided access to the emission of CO Angstrom band. To further validated this approach, it would be necessary to compare the gas temperature measures through FTIR measurements and through the rotational temperature fit.

3.4 Fourier Transform Infrared Spectroscopy - Experimental Results

3.4.1 General Considerations

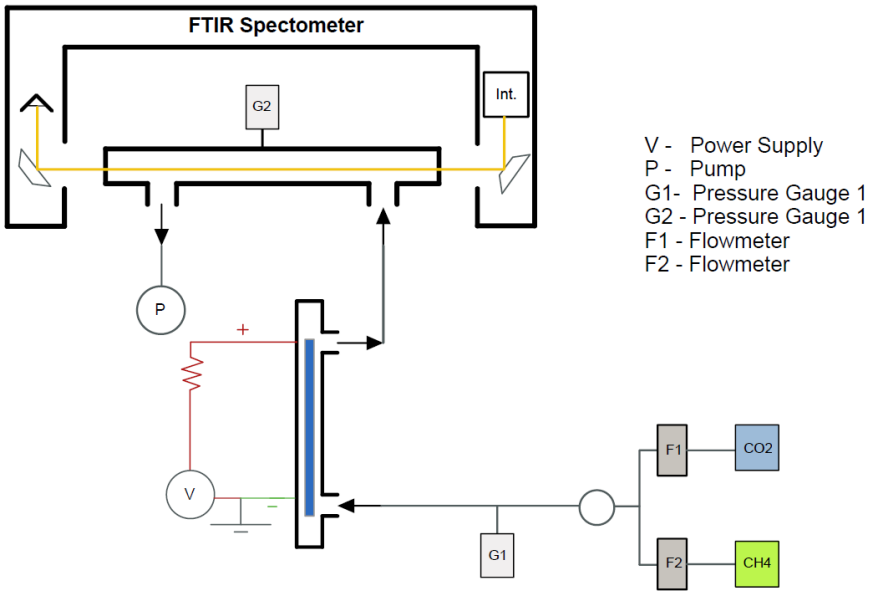

Figure 3.15: Experimental setup for the DC Glow Discharge plasma, used for FTIR measurements.

In this section we analyze the concentration of species downstream the DC discharge, ignited with mixtures of CO_2 and CH_4 (see figure 3.15). More specifically, we will analyze the fraction of CO_2, CO, CH_4, C_2H_2, C_2H_4, C_2H_6 and H_2O as function of various parameters, namely gas pressure, initial CO2 fraction and total gas flow. The input gas consists of CO_2 and CH_4, whose flows are controlled by the respective flowmeters, in the range between 1.45 sccm to 7.40 sccm. The gas is pumped into the reactor, where the plasma is created as a result of the high voltage applied between the cathode and anode, with a low current (typically $\leq$ 50 mA). Argon flow is used to clean the reactors in between measurements. Finally, since this is a downstream measurement, the second reactor acts as a measurement cell for the post-plasma gas, and this is where the FTIR measurements will be made. Regarding the measurements, the following concerns are important to consider:

- Liquid nitrogen was used to initially cool the FTIR before every set of measurements and the reactor was purged with Argon, for 20 minutes, with the pump turned on, in order to clean the reactor of impurities and unwanted species. This was done every 3 hours, in case measurements were continuously being made.
- The background emission was taken after the cooling of the FTIR and before turning on the plasma.
- The pressure was controlled and measured directly with the pressure gauge. Some conditions (depending on the pressure studied) required a calibration of the pressure through adjustments of about 0.02-0.05 Torr.
- For pressures higher than 1 Torr, the experimental measurements were taken using an automatic script, that controlled the different parameters (pressure, current, gas flows) and was able to collect all the necessary spectrums. At low pressures (below 1 Torr) this automatic script had be replaced

by manual control, given that the automated pressure controller did not allow pressure as low as 1 torr for flows of 7.40sccm.

- Before turning on the plasma, the absorption spectrum was always taken with the desired gas flows in the reactor, without using high voltage. The purpose of this point was to confirm that the gas mixture before the plasma was properly formed. With the fitting algorithm, it was possible to confirm the presence of CH_4 and CO_2. Initially, the gas mixture was not always the expected one and it was necessary to repeat some of the measures. When the experimental measures were redone, more time was given in between measurements, so that the inlet gases had more time to purge the previous gas composition. After this, the chemical composition was the intended one.

- From the fitting algorithm, it was also possible to obtain a measured value of the pressure. This value was always calculated with a systematic error of about 0.1 Torr at low pressure and 0.2 Torr at high pressures.

- Regarding the total flow, two different values were used, $\dot{Q} = 7.40sccm$ and $\dot{Q} = 2.88sccm$. The first flow value was used since it provided a stable α parameter (dissociation rate,$\alpha = [CO]_{out}/[CO2]_{in}$) during the measurements. The second value leads to an equal residence time of the experimental data present in section 3.3.

3.4.2 Results

In this section, the results of the spectrum transmittance fitting will be shown. This fit will provide the equilibrium chemical composition of the plasma species, as function of different initial conditions.

We start by exploring the different chemical compositions for constant values of the pressure and total flow (3 Torr and 2.89 sccm), while changing the discharge current. In figure 3.16 we can see that the amount of CO_2 and CH_4 are decreasing, with a total reduction of more than 10 % in the concentration. On the other hand, CO fraction has a steady increase from about 0.25% to about 0.4% when the current increases from about 10 to 50 mA.

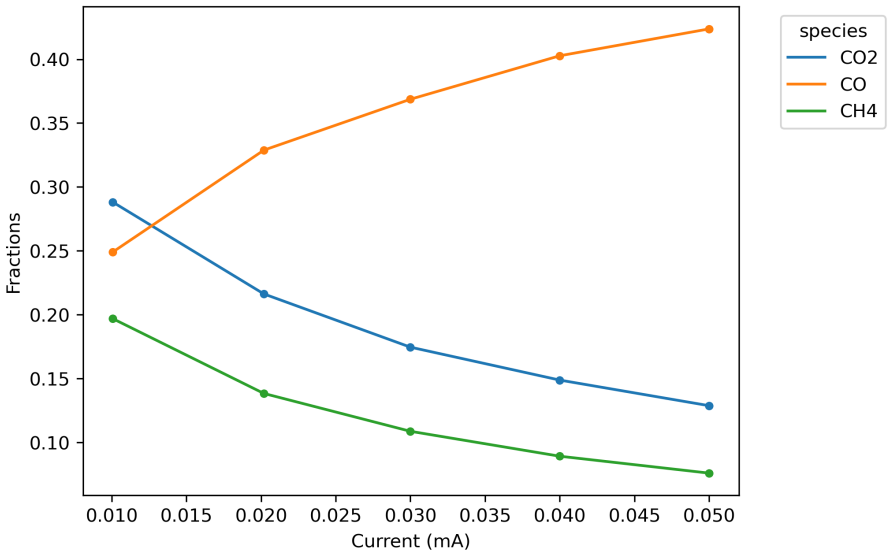

Figure 3.16: Equilibrium concentration values for CO_2, CO, CH_4, with varying current, at 3 Torr, with a 50/50% CO_2/CH_4 mixture and with total flow at 2.89 sccm.

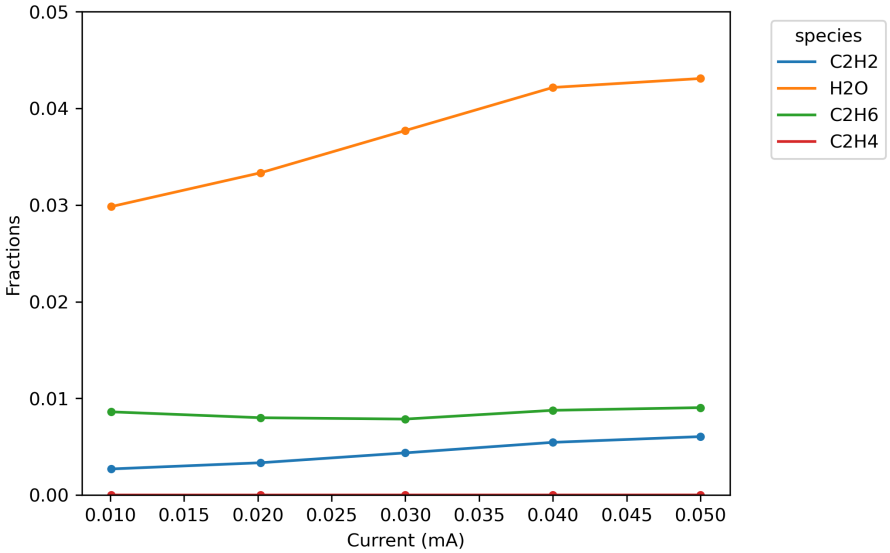

Figure 3.17: Equilibrium concentration values for H_2O, C_2H_2, C_2H_4 and C_2H_6, with varying current, at 3 Torr, with a 50/50% CO_2/CH_4 mixture and with total flow at 2.89 sccm.

In figure 3.17 it is possible to look at the low-concentration species. Under the present conditions, water can reach 4% concentration for currents above 40 mA. It is also possible to see that the concentration is increasing with the increasing current. Small amounts of C_2H_4 and C_2H_6 were also detected, with concentrations of about 1 % and 0.5%, respectively. Negligible quantities of C2H4 were also detected. It is worth mentioning also that the sum of the total concentrations does not add up to 100 %, given that some molecules and atoms present in the setup are not detected by FTIR, such as O_2, H_2, O and H.

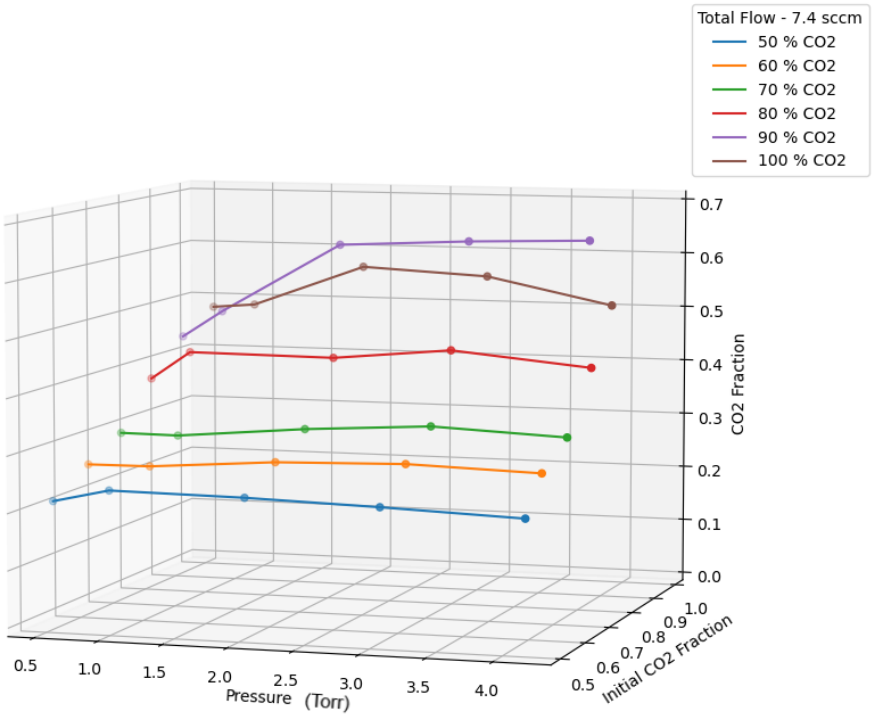

Figure 3.18: Equilibrium concentration values for CO_2, with varying current and pressure, with a total flow of 7.40sccm.

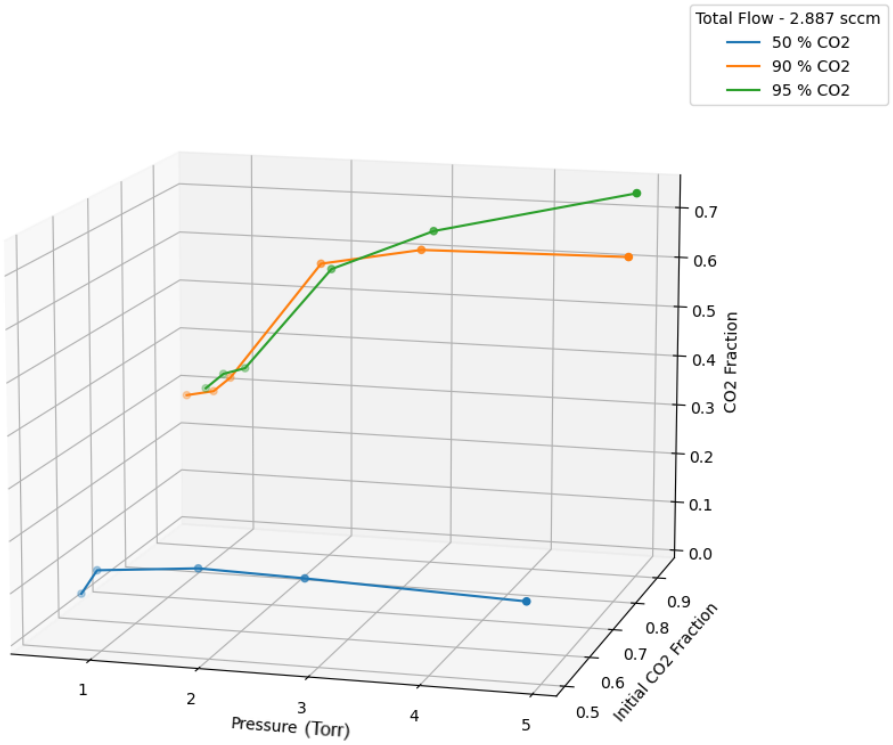

Figure 3.19: Equilibrium concentration values for CO_2, with varying current and pressure, with a total flow of 2.89sccm.

In figure 3.18 we can see the change of CO_2 concentration with the gas flow of CO_2 and gas pressure, using a total gas flow of 7.40 sccm. Here we see that by increasing the initial amount of CO_2 in the plasma we also increase the final concentration of CO_2. As for the effect of the pressure, the variation is much lower. It is worth noticing that when the initial flow of CO_2 is 90%, the measured concentration of CO_2 presents a significant increase with the pressure (about 20%). This effect will be further explored in the modelling section.

The results related to the total gas flow of 2.89 sccm can be seen in figure 3.19. When the initial CO_2 flow is 50% there is a clear decrease in the measured amount of CO_2, compared to the situation observed in figure 3.18. When the initial CO_2 flow is 90 % and 95%, the variation of pressure has a significant impact on the final amount of CO_2 in the plasma, since the concentration values can increase up to 40 %.

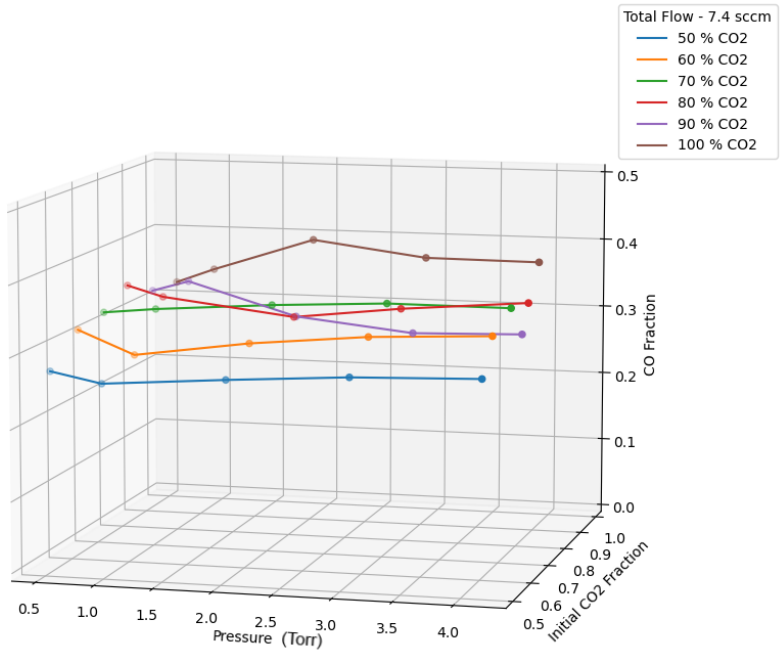

Figure 3.20: Equilibrium concentration values for CO, with varying current and pressure, with a total flow of 7.40sccm.

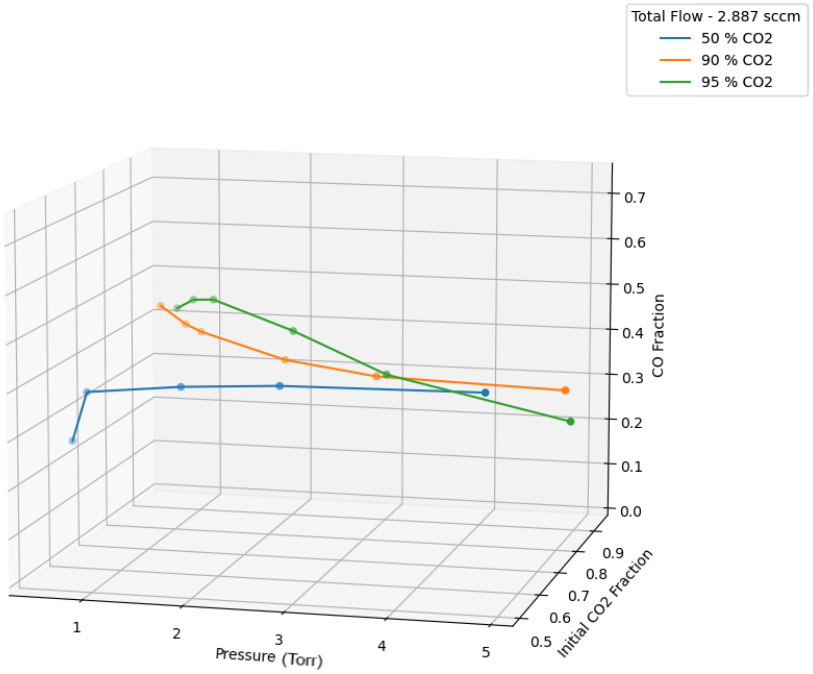

Figure 3.21: Equilibrium concentration values for CO, with varying current and pressure, with a total flow of 2.89sccm.

The results related to the fraction of CO measured downstream the reactor are shown in figure 3.20 and 3.21. In 3.20 we see that the final concentration of the final concentration of CO does not vary linearly with the initial amount of CO_2 mixture. Furthermore when the mixture is 90% CO_2, the fraction of CO has a significant decrease with the increase of gas pressure. effect can also be related to an increase of CO2 fraction. However, when the mixture is composed by 100 % CO_2,an opposite trend is observed. Here the amount of CO fraction increases with the pressure. This effect will be further

explored during the modelling analysis in chapter 4.

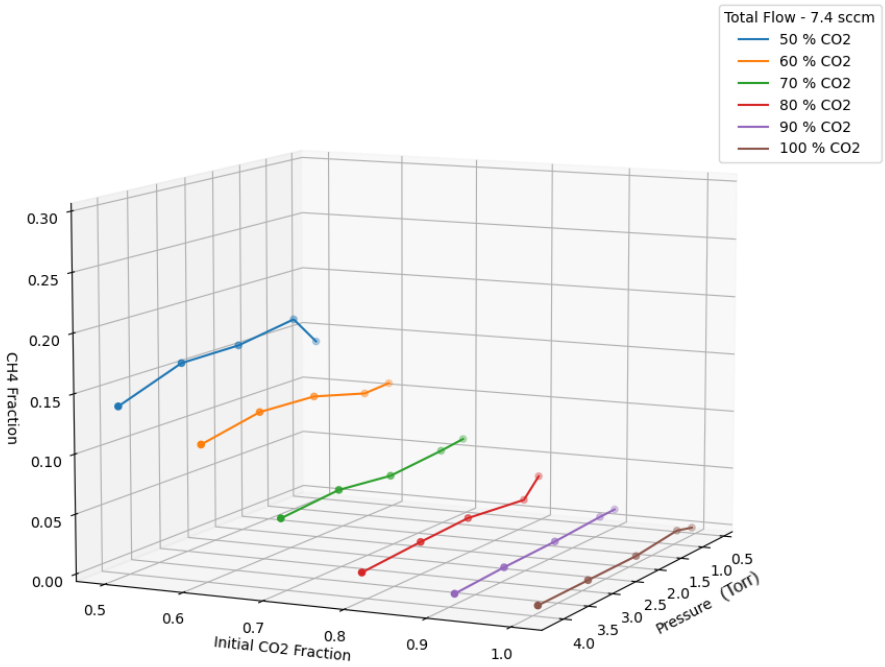

Figure 3.22: Equilibrium concentration values for CH_4, with varying current and pressure, with a total flow of 7.40sccm.

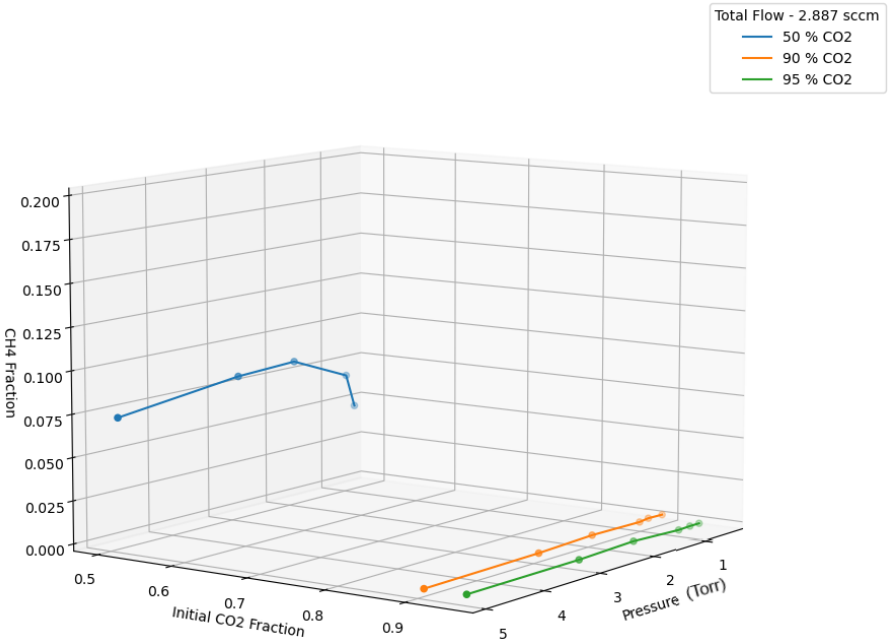

Figure 3.23: Equilibrium concentration values for CH_4, with varying current and pressure, with a total flow of 2.89sccm.

Figures 3.22 and 3.23 show the results related to the change of CH_4 fraction as a function of pressure and initial fraction of CO_2. Firstly, and provided that we are not considering high-pressure values (above 2 Torr), the variation of pressure does not have a major influence in the measured CH_4 fraction. Also, the variation of the total flow seems to reduce the CH_4 fraction measured in the plasma (see the cases of 50% initial CO_2 fraction between figure 3.22 and 3.23). Finally, as it would be expected,

the fraction of CH_4 measured increases when increasing the initial amount of CH_4 used in the mixture.

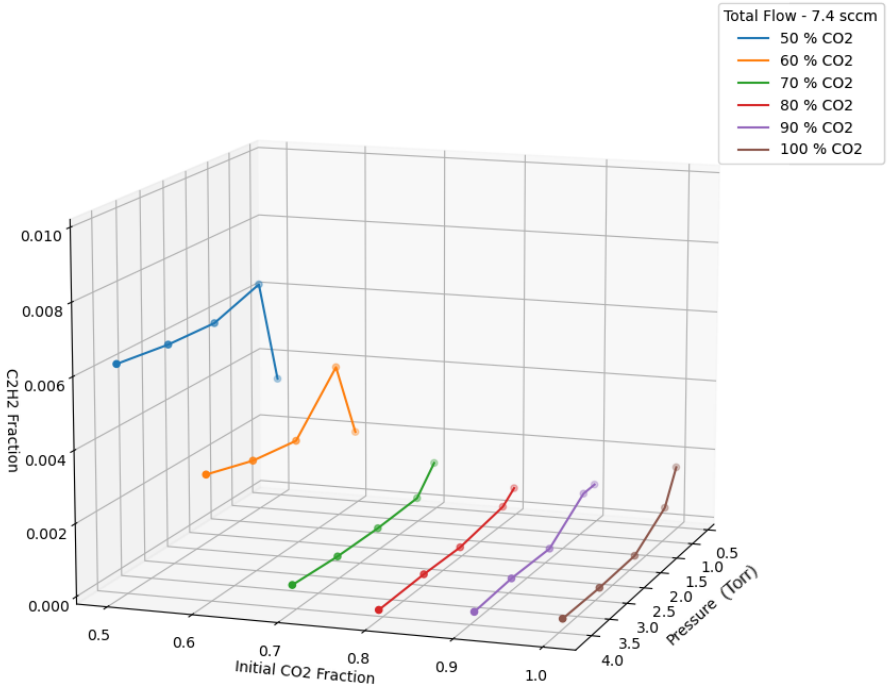

Figure 3.24: Equilibrium concentration values for C_2H_2, with varying current and pressure, with a total flow of 7.40sccm.

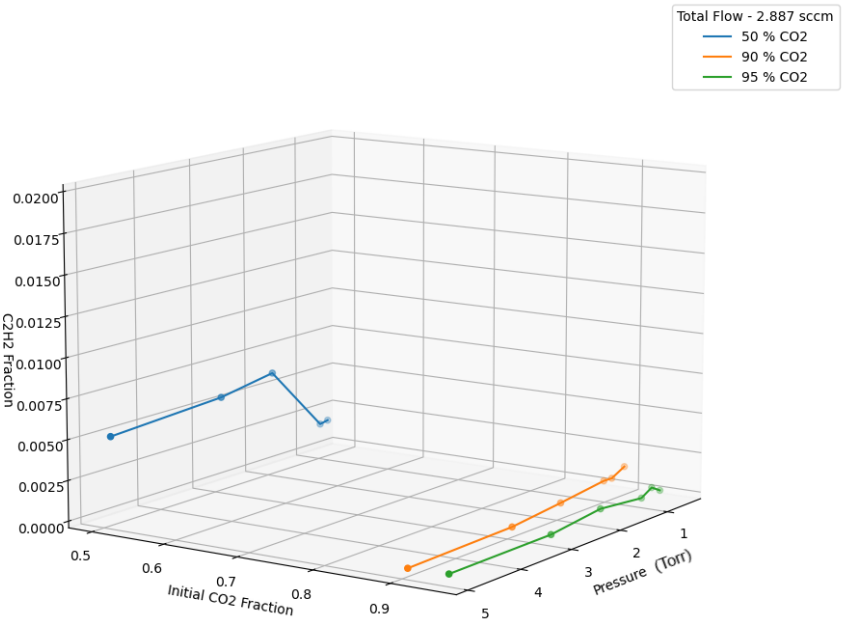

Figure 3.25: Equilibrium concentration values for C_2H_2, with varying current and pressure, with a total flow of 2.89sccm.

The results related to the C_2H_2 fraction measured in the plasma are shown in figures 3.24 and 3.25. Compared to the previous species, we can see that the concentration of C_2H_2 is very small. Nevertheless, it is interesting to note that trends associated to the change of C_2H_2 fraction are similar to the trends observed in case of CH_4. For instance, the change of C_2H_2 fraction seems to be also

independent of the pressure (for values above 2 torr). Furthermore, a an increase of the initial amount of CH_4 in the mixture also leads to an increase of the amount of C_2H_2.

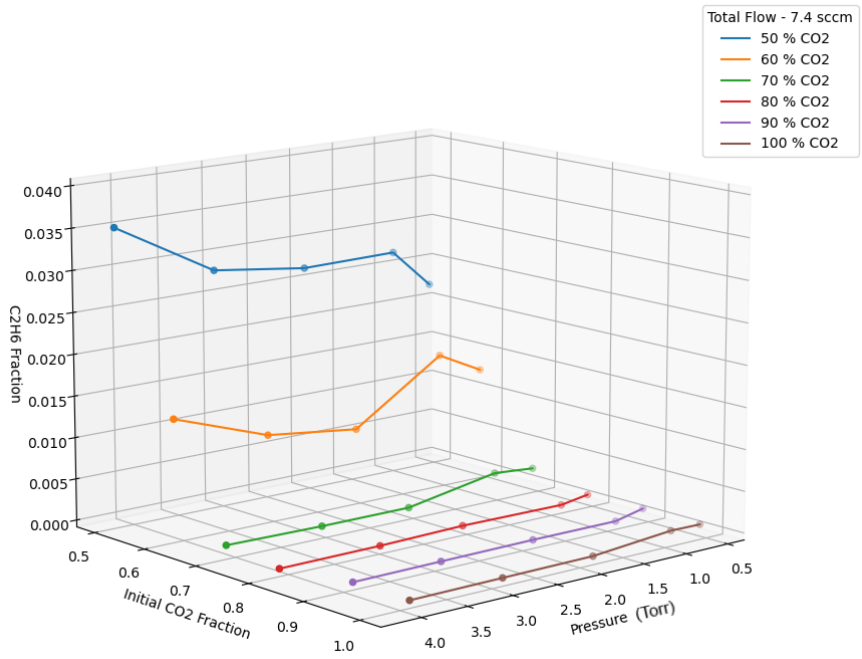

Figure 3.26: Equilibrium concentration values for C_2H_6, with varying current and pressure, with a total flow of 7.40sccm.

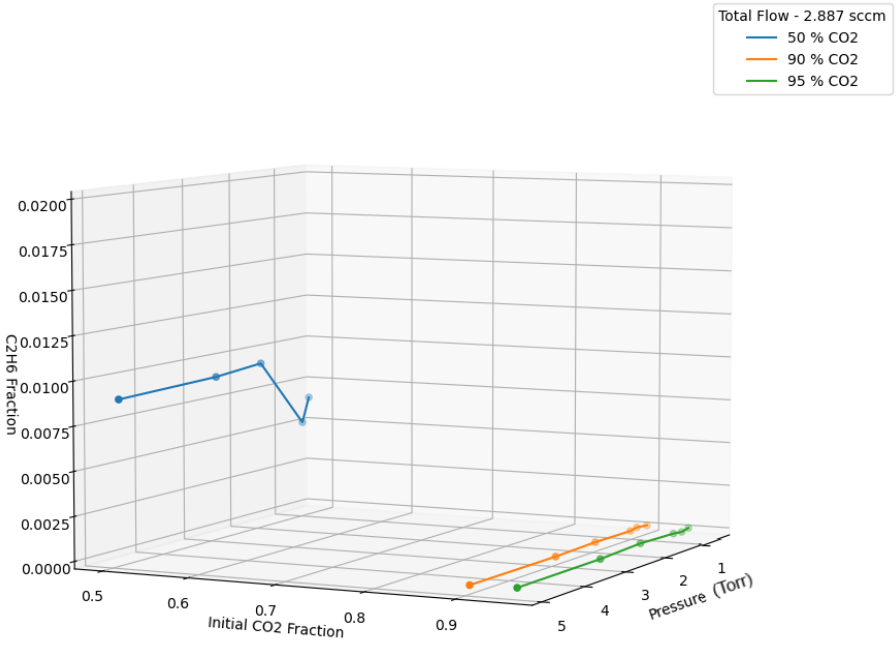

Figure 3.27: Equilibrium concentration values for C_2H_6, with varying current and pressure, with a total flow of 2.89sccm.

The C_2H_6 fractions are shown in figures 3.26 and 3.27. The molecule can reach a concentration above 3%, which may lead to an important contribution for the overall chemistry of CO_2-CH_4 plasmas. We can see that an increase of he total flow rate leads to an increase of the C_2H_6 fraction. We can also see that, as the initial amount of CH_4 increases, so does the final concentration of C_2H_6.

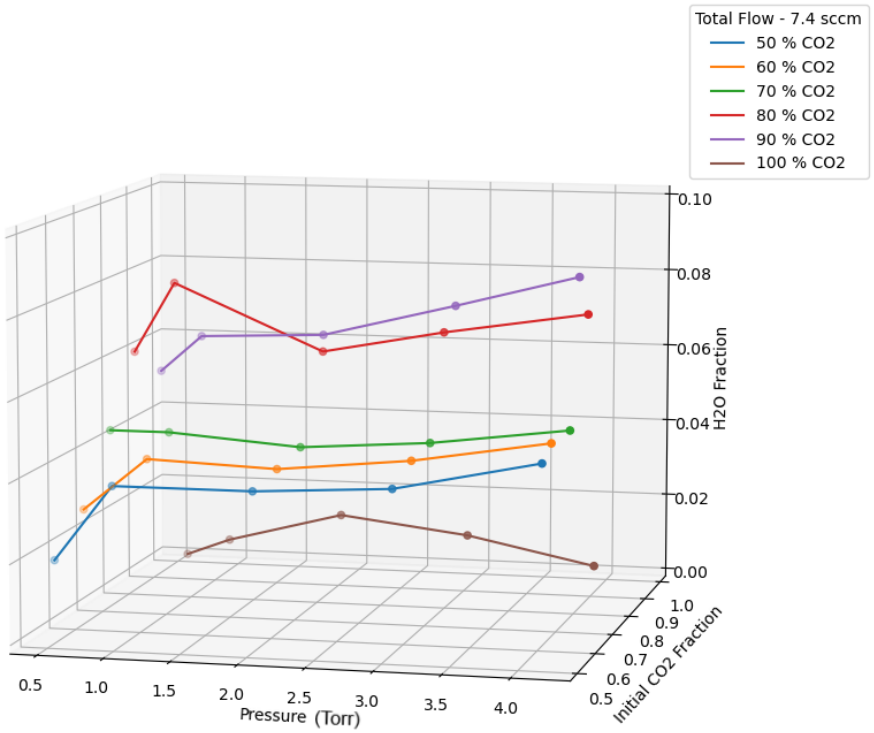

Figure 3.28: Equilibrium concentration values for H_2O, with varying current and pressure, with a total flow of 7.40sccm.

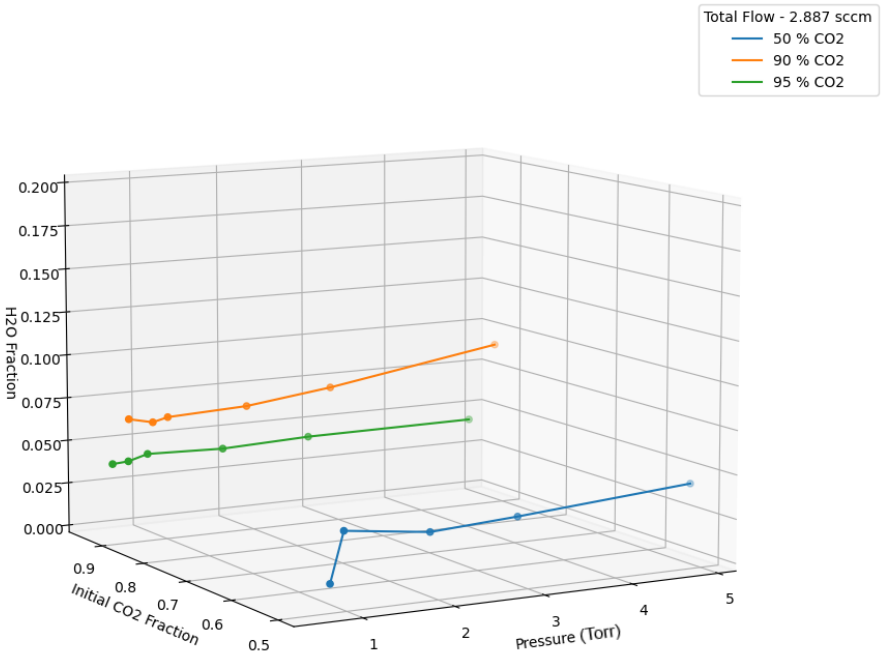

Figure 3.29: Equilibrium concentration values for H_2O, with varying current and pressure, with a total flow of 2.89sccm.

The results related to the H_2O fraction are shown in figures 3.28 and 3.29. First of all, note that the H_2O molecule should not be detected when the initial mixture is composed by entirely by CO_2 given the lack of H atoms be present if the initial amount of CO_2 is 100%, given the lack of H atoms. However in figure 3.28, with a pressure of 1.75 torr, a small amount of H_2O is found. This observation is due to

remains of H_2O from previous measurements that were not removed from the reactor. Note that when the initial concentration of CO_2 is ranged from 80 % to 90 %, the H_2O fraction is about 6% to 8%. If the initial CO_2 concentration is ranged between 50% and 70%, the H_2O fraction decreases to about 2% to 4%. Also when the total flow is 2.89 sccm, the fraction of H_2O decreases about 50% (compared to the situation with higher flow rate). Finally, regarding the pressure effect in figure 3.29, we see that, in general, the fraction of H_2O increases with the gas pressure.

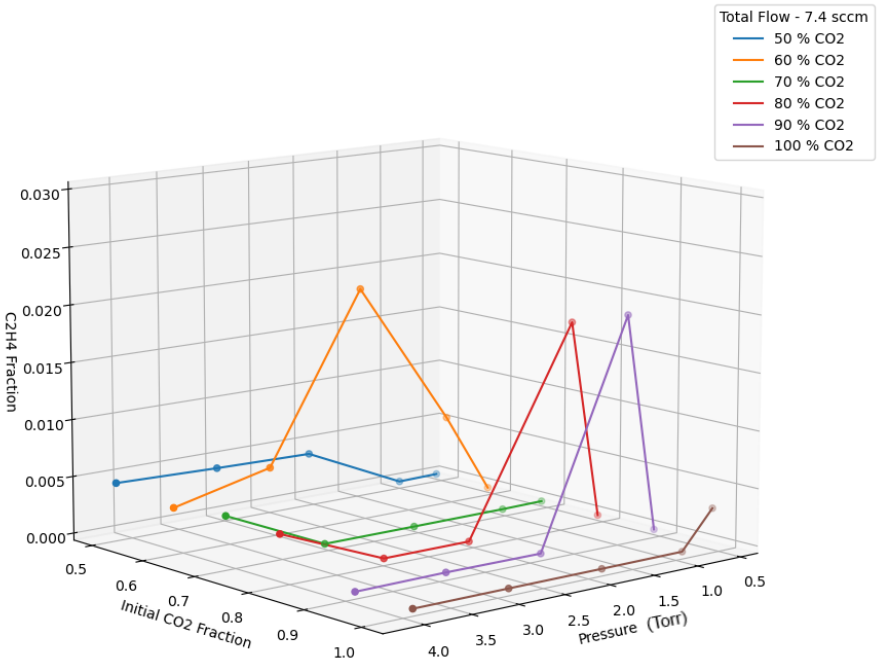

Figure 3.30: Equilibrium concentration values for C_2H_4, with varying current and pressure, with a total flow of 7.40sccm.

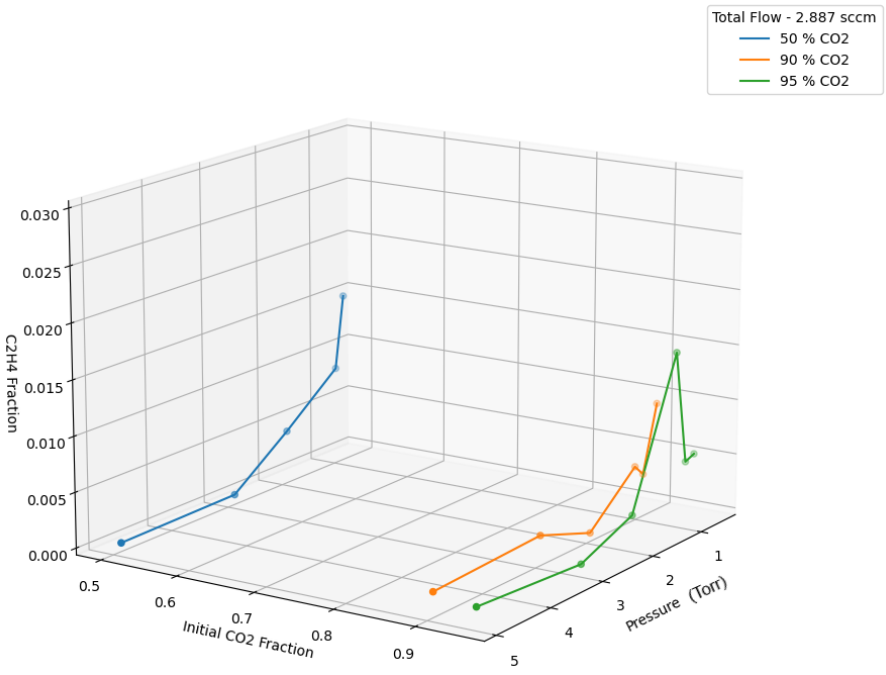

Figure 3.31: Equilibrium concentration values for C_2H_4, with varying current and pressure, with a total flow of 2.89sccm.

Finally, figures 3.30 and 3.31 shows the results associated to the fraction of C_2H_4 molecule. For both situations of total flow (i.e. 7.40 sccm and 2.89 sccm), the experiments show a general increase of the C_2H_4 fraction with the decrease of pressure. For some conditions the fraction of C_2H_4 can reach about 2%

Chapter 4

Modelling

4.1 Theoretical Introduction

In order to accurately simulate our low temperature plasma and compare our experimental results, the LisbOn KInetics Simulation Tool (LoKI) was used [48]. Plasmas are a notoriously complex environment, due to the non-linearity of the equations that govern it. Overall, the LoKI software is able to solve a two-term homogeneous electron Boltzmann (LoKI-B) and also to determine the chemistry of the various neutral and charged species present in the plasma (LoKI-C). The LoKI software is programmed under MATLAB to benefit from its matrix-based architecture, and LoKI-B is distributed as open-source [48]. In the next sections, an overview of the models is given.

4.1.1 LoKI-B

It's possible to write the electron Boltzmann equation as:

$$\frac{\partial f_e}{\partial t} + \vec{v_e}.\vec{\nabla}_{\vec{r}} f_e + \frac{\vec{F_e}}{m_e}.\vec{\nabla}_{v_e} f_e = \left(\frac{\partial f_e}{\partial t}\right)_{coll}, \tag{4.1}$$

where f_e is the velocity distribution function , $\vec{v_e}$ is the electron velocity, $\vec{r}$ is the electron position, $\vec{F_e}$ is the total force applied on the electron, $\left(\frac{\partial f_e}{\partial t}\right)_{coll}$ is the variation of the EEDF due to the collision between electrons and heavy species

Since this equation is difficult to solve, approximations are commonly used. To learn more about the assumptions/approximations used in the LoKI Boltzmann solver, see Tejero-del-Caz et al [48]. In this case, we just look at the most relevant ones:

- Steady State: Because the EEDF's relaxation time is shorter than that of any other phenomenon under study, it does not depend explicitly on time.
- Plasma homogeneity: the EEDF does not depend explicitly on position (Electric field roughly uniform);
- Non-magnetised plasma;
- Small anisotropic regime: Because the electric field only induces small anisotropies in the system, the velocity distribution function expansion may be expressed as $f_e \approx f_{e,1} + \vec{v_e}.\vec{f_{e,1}}$

With these approximations, equation 4.1 may be simplified to:

$$\frac{\partial f_e}{\partial t} - \frac{\vec{F_e}}{m_e}.\vec{\nabla}_{v_e} f_e = \left(\frac{\partial f_e}{\partial t}\right)_{coll}, \tag{4.2}$$

4.1.2 LoKI-C

LoKI-C is concerned with the processes that occur in the plasma that include heavy species. So, for each heavy atom in plasma, including transport effects, the algorithm solves the zero-dimensional rate-balance equations (volume averaged). This is the rate balance equation for the general species i:

$$\frac{dn_i}{dt} = \sum_j \left(\frac{dn_i}{dt}\right)_j = 0 \tag{4.3}$$

where n_i is the density of species i and the sum is computed over all j reactions involving the formation or destruction of species i. The following equation can be used to generalize the numerous species equations that account for their genesis and destruction:

$$\left(\frac{dn_i}{dt}\right)_j = \left(k_j \prod_l n_l\right)\left(a^+_{i,j} - a^-_{i,j}\right) \tag{4.4}$$

where $a^+_{i,j}$ and $a^-_{i,j}$ are the stoichiometric coefficients of species i on the right and left hand sides of the reaction, accounting for the formation and destruction mechanisms, respectively, and the sum is performed over the number of j reactions involving species i.

Heavy-species chemistry reaction rates are classified into four categories: electron-heavy species (e-H), heavy species (H-H), diffusion to the wall (H-w), and reactor inlet and outlet flow. These types of reactions are discussed in the following sections:

Electron-heavy species

Electron impact excitation, electron impact dissociation, electron impact ionization, and electron attachment are all examples of reactions in this category. They take the form:

$$e + M \longrightarrow \text{reaction products} \tag{4.5}$$

where M is a collisional species. The reaction terms are described by [49]:

$$\left(\frac{dn_i}{dt}\right)_{e_H} = n_e \sum_j \left(\left(a^+_{i,j} - a^-_{i,j}\right) n_j k_j\right) \tag{4.6}$$

where n_i denotes the density of the species i on the left-hand side of reaction j and n_e denotes the electron density, which is used as an input in the model. The rate coefficient is then calculated numerically by integrating the cross section found in the literature for each specific process using the EEDF calculated by the LoKI-B.

Heavy species reactions

This group includes all 2 or 3 body reactions involving collisions between neutrals and/or ions, as well as radiative decay.. They take the following form:

$$\alpha_1(M_1) + \alpha_2(M_2) + \alpha_3(M_3) \longrightarrow \text{reaction products} \tag{4.7}$$

where M_k represents the species and a_k its stoichiometric coefficient. The reaction terms are given by:

$$\left(\frac{dn_i}{dt}\right)_{H-H} = n_e \sum_j \left(\left(a_{i,j}^+ - a_{i,j}^-\right) n_{j,1} n_{j,2} n_{j,3} k_j\right) \tag{4.8}$$

In this scenario, the rate coefficients k_j are commonly derived using Arrhenius type equations, the constants for which can be found in the literature. If vibrationally excited species are present in the chemical equation, the Fridman approximation [1] often can be utilized.

Diffusion to the Wall

Diffusion to the wall can result in the loss of both neutral and charged particles, with different equations describing these processes. Beginning with the neutrals, the wall losses of neutral species I are computed using an effective loss rate coefficient on the wall, k_j, where i is the typical decay time due to diffusion to the wall ($\tau_i = k_j^{-1}$) [50]. This decay time is calculated as follows:

$$\tau_i = \frac{\Lambda^2}{D_i} + \frac{\frac{4V}{S}(1 - \frac{\gamma_i}{2})}{\gamma_i \overline{v_i}} \tag{4.9}$$

where Λ is the characteristic length, V and S are the reactor volume and area, D_i is the diffusion coefficient, γ_i is the destruction probability on the wall and $\overline{v_i}$ is the thermal speed of species i. The diffusion coefficient D_i is given by [51]:

$$D_i = \frac{1 - \chi_i}{\sum_{i \neq b} \frac{\chi_b}{D_{ib}}} \tag{4.10}$$

and where $\chi_i = N_i/N$ and $\chi_b = N_b/N$ are the relative concentrations of species i and b in the plasma; and D_{ib} are the binary diffusion coefficients of species i in background gas b, respectively. The mathematical formula for D_{ib} is given by Hirschfelder [52] as:

$$D_{ib} = \frac{1.930 \times 10^{21} \sqrt{\frac{T_{gas}}{2u_{ib}}}}{N \sigma_{ij} \Omega^{(1,1)*} T*} \tag{4.11}$$

where u_{ij} is the reduced mass, $T* = k_B T_{gas}/e_{ij}$, and σ_{ij} and ϵ_{ij} are parameters of the Lenard-Jones interaction potential. The collision integral $\Omega^{(1,1)*}$ can be found in [52], and the Lenard-Jones parameters are given by $\sigma_{ij} = (\sigma_i + \sigma_j)/2$ and $\epsilon_{ij} = \sqrt{\epsilon_i \epsilon_j}$. The individual Lenard-Jones parameters can be found in the literature.

Finally, by combining the last two formulas, the reaction term associated with neutral species diffusion to the wall is obtained by:

$$\left(\frac{dn_i}{dt}\right)_{e_H} = n_e \sum_j \left(\left(a_{i,j}^+ - a_{i,j}^-\right) n_j / \tau_i\right) \tag{4.12}$$

Where species i is being destroyed by reaction j at the wall.

Regarding, charged species it is important to note that they experience a different process than neutral species when it comes to plasma diffusion, which is called ambipolar diffusion. Here, the ambipolar diffusion coefficient for a specific species i, $D_{a,i}$ may be calculated by using the following formula:

$$D_{a,i} = D_i - \mu_i \frac{\sum_{b=1}^{n+1} n_b D_b}{\sum_{b=1}^{n+1} n_b \mu_b} \tag{4.13}$$

Where D_i and μ_i are the free diffusion and mobility coefficients of each species i and these two

numbers can be obtained and used to generate the relevant rate coefficient by repeating the previous approach and using the free mobility coefficient as a tabular value.

$$k_i = \frac{D_i}{\Lambda^2} - \frac{\mu_i}{\Lambda^2} \frac{\sum_{b=1}^{n+1} n_b D_b}{\sum_{b=1}^{n+1} n_b \mu_b} \tag{4.14}$$

Similarly, the contribution to the rate balance equation is determined using expression 4.12.

Entering and existing flow

The reactions of entering and exiting flow may be represented as

$$* \longrightarrow M, \text{ inlet flow} \tag{4.15}$$

$$M \longrightarrow *, \text{ outlet flow} \tag{4.16}$$

Because there are no species on the reaction's left side, the given rate coefficient is already a rate density. As a result, the term that accounts for the incoming flow response may be easily expressed as

$$\left(\frac{dn_i}{dt}\right)_{in} = \frac{4.47796 \times 10^{17} f_i^{in}}{V} \tag{4.17}$$

in which 1 sccm = 4.47796 particles/s is included as a conversion factor in the numerator, V is the reactor's volume, and f_i^{in} is the inlet flux.

The steady-state system approximation is utilized to compute the exit flow term by assuming that the total number of particles in the reactor is kept constant, and therefore this rate coefficient is computed at each time instant to keep the balance constant. This way, the exiting flow term is given by:

$$\left(\frac{dn_i}{dt}\right)_{out} = n_i k^{out} = n_i \frac{4.47796 \times 10^{17} f_i^{out}}{V} \tag{4.18}$$

where f_i^{in} is the outlet flux.

4.1.3 LoKI Flowchart

We will now look into the workflow of the LoKI as a whole, as represented in figure 4.1

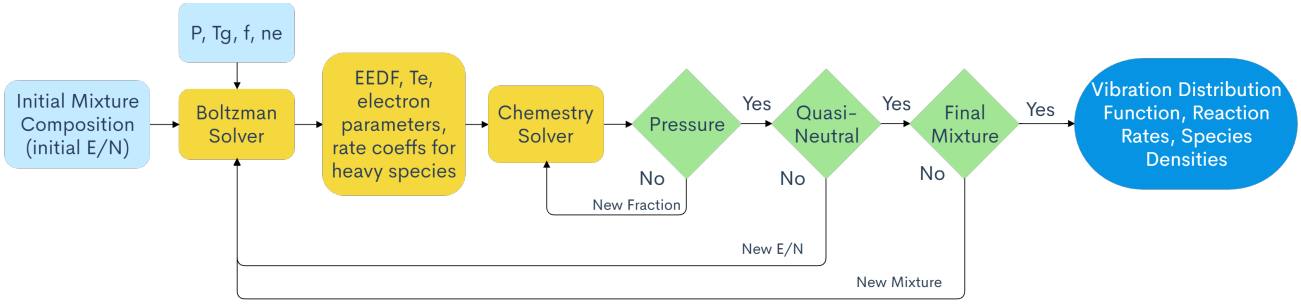

Figure 4.1: Flowchart of the LoKI software.

In the flowchart, one begins by supplying the original neutral gas mixture and an initial approximation for the reduced electric field. The Boltzmann Solver is then used to solve the electron Boltzmann equation using the provided cross sections. Once the working conditions have been set up, one enters them all at once: in this case: pressure (p), gas temperature (T_g), electron density (n_e), and optionally

the EEDF - otherwise, LoKI calculates the EEDF and integrates over it to achieve the desired rates corresponding to the transition from state i to state j, according to the following expression:

$$C_{i,j} = \sqrt{\frac{2}{m_e}} \int_0^{+\infty} u\sigma_{i,j}(u) f(u) du \tag{4.19}$$

where m_e is the electron mass, $\sigma_{i,j}$ the cross sections and u the energy, and $f(u)$ the EEDF. In addition to the EEDF and rate coefficients, the user is also given with the electron swarm characteristics and temperature, T_e.

The code now moves on to the chemical solver, LoKI-C. Three nested cycles are performed using the LoKI-B output as inputs to evaluate the pressure, neutrality, and final balance of the system. A new fraction is examined if the conservation of particles does not meet a certain threshold in the initial cycle. A new value of E/N is proposed if the plasma charge differs from zero on the quasi-neutrality cycle. When it comes to the last cycle, it checks to see if the final mixture has been attained, and restarting the whole process if needed. When a value less than the global cycle limit error is achieved, the process is completed.

4.2 Simulation Results

In order to simulate the CO_2/CH_4 plasma and replicate the experimental data, several steps were necessary. First, it is necessary to study electron kinetics, in order to test whether the swarm parameters were accurate comparing to the experimental data. For this, a study of the swarm parameters was carried out in section 4.2.1, and LoKI-B was used.

Having done this validation, we move on to LoKI-C and create a model for the chemistry of our system. This was done by testing different reactions between the molecules present in the plasma and different rate coefficients, that were found in the literature. After this, we can test our model for numerous plasmas conditions, to try to replicate our experimental data. In this case, it was necessary to the give the gas temperature T_g, pressure p, the length and radius of the plasma reactor. Furthermore in order to have the correct electrical current, it was necessary to adjust the electron density n_e parameter, since the parameters are related by the following expression [49]:

$$I = n_e \cdot e\pi R^2 v_d \tag{4.20}$$

where e is the elementary electric charge, R is the reactor radius and v_d the drift velocity, which was obtained through the simulation. After the input parameters were determined, the LoKI software was used, and it ran until the system converged, as described in figure 4.1

4.2.1 Swarm Analysis

In order to test the electron kinetics of the simulation, the swarm parameters for pure CO_2 and CH_4 were obtained. This was done using the LoKI-B code, and a temperature of 300 K. Values for the characteristic energy, the reduced townsend coefficient and the mobility gas density were obtained for different reduced electric fields (E/N) in the range of interest for this work, and compared to experimental values, as it can be seen in figures 4.2 to 4.7. The experimental values were taken from the IST Lisbon Database [53] and from the Dutton Database [54].

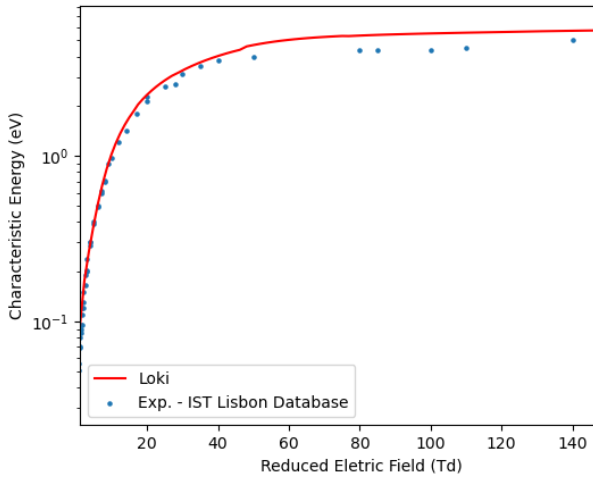

Figure 4.2: Characteristic energy, pure CH_4

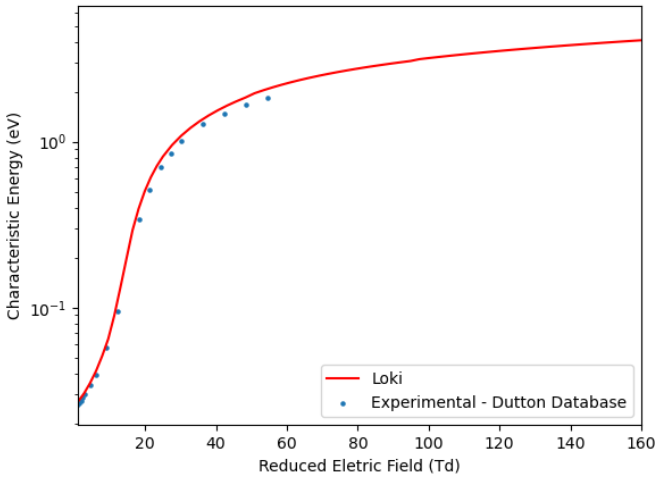

Figure 4.3: Characteristic energy, pure CO_2

The swarm parameters were obtained for pure CO_2 or CH_4 discharges. Results show a very good agreement between the simulation and the experimental results, especially considering that for our experiment, $E/N \in [40, 100]Td$. Finally, using the electron kinetics presented, it was possible to obtain the drift velocity parameter v_d, which was used to calculate the plasma current, using equation 4.20.

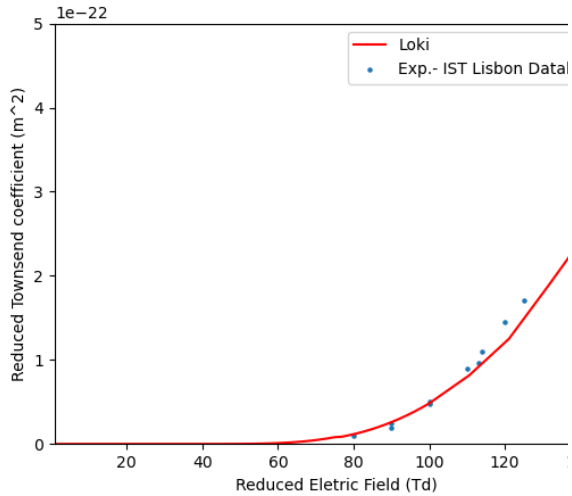

Figure 4.4: Reduced townsend coefficient, pure CH_4

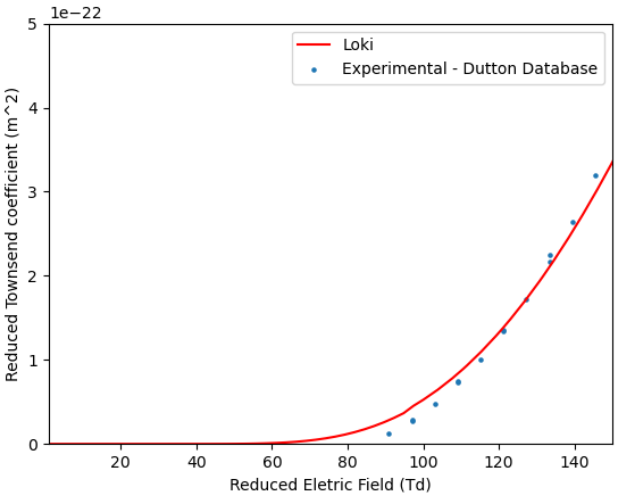

Figure 4.5: Reduced townsend coefficient, pure CO_2

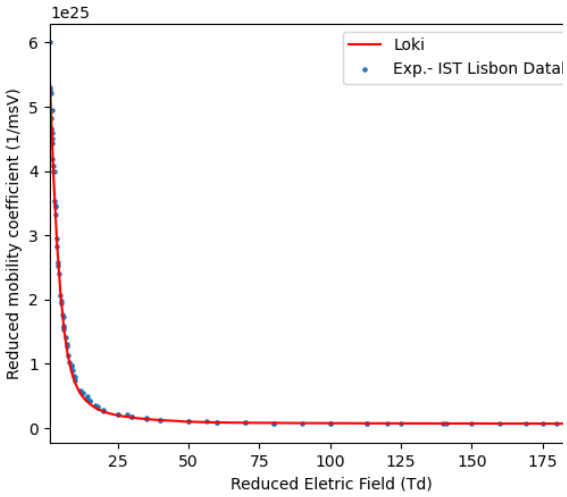

Figure 4.6: Mobility gas density, pure CH_4

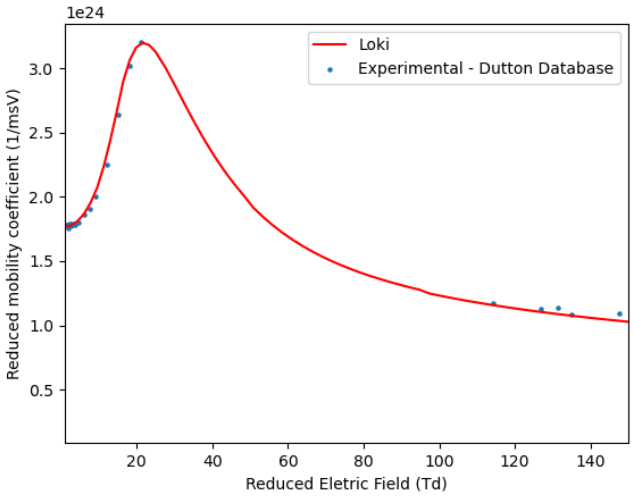

Figure 4.7: Mobility gas density, pure CO_2

4.2.2 Chemistry Analysis

Having explored the electron kinetics, we can now dive into the simulation results for the chemical composition of the plasma. In this work, to analyze the plasma chemistry associated to CO_2-CH_4 plasmas, we extended the chemical module proposed in [49] for pure CO_2 discharges by including several additional species. The list of all molecules and ions considered can be found in tables 4.1. To this purpose, we considered more than 250 reactions, using the rate coefficients taken from the available literature. In appendix A we can find the complete list of reactions included in our chemistry module. For completeness, the calculated concentrations of all the species considered in the model are given in the appendix B for a few representative working conditions. After the comparison with the experimental results is made, we will also explore which reactions are more important for the creation and destruction of the most important species. We start by looking at the variation with the current, at a constant pressure and initial chemical composition.

O_2	O	O_3	H_2	H
CO_2	CO	CH_4	CH_3	CH_2
HCO	OH	H_2O	CH_2O	CH
C	C_2	C_2H	C_2H_2	C_2H_3
C_2H_4	C_2H_5	C_2H_6		
$O_2(+)$	O(+)	O(-)	$CO_2(+)$	CO(+)

Table 4.1: Molecules and ions included in the kinetic model

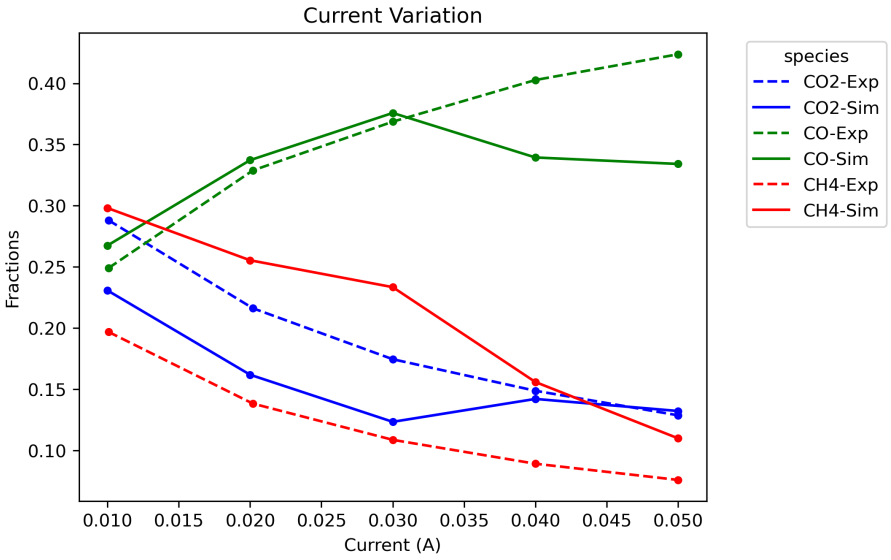

Figure 4.8: Experimental and simulation equilibrium concentration values for CO_2, CO, CH_4, with varying current, at 3 Torr, with a 50/50% CO_2/CH_4 mixture and with total flow at 2.89 sccm.

Although the general trends are well captured by the model, there are some discrepancies between the experimental and the simulated values in figure 4.8 In particular, there is an overestimation of the amount of CH_4 for all current values and an underestimation of the amount of CO_2 and CO in some current values . In the experimental values, it is possible to see an overall trend of increasing CO and decreasing CO_2 and CH_4 with the current. For the simulated concentrations, it is not possible to see this trend, particularly for currents above 30 mA.

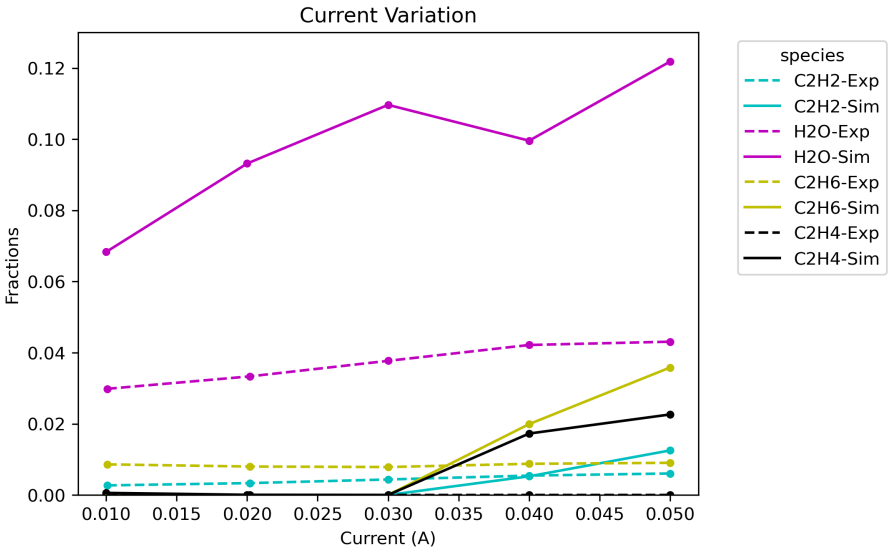

Figure 4.9: Experimental and simulation equilibrium concentration values for H_2O, C_2H_2, C_2H_4 and C_2H_6, with varying current, at 3 Torr, with a 50/50% CO_2/CH_4 mixture and with total flow at 2.89 sccm.

In figure 4.9 the concentration of the remainder species is presented. There is an overestimation of amount of H_2O in the simulation results, but overall it is possible to see an increase in the amount of H_2O with the gas current both in the experimental and simulated data. For the C_2H_m species, we can see that, for lower currents, the concentration values are negligible. However, when the current increases, small amounts of C_2H_2, C_2H_4 and C_2H_6 were detected in the simulation, and there is indeed

an overestimation of these concentrations, comparing with the experimental data.

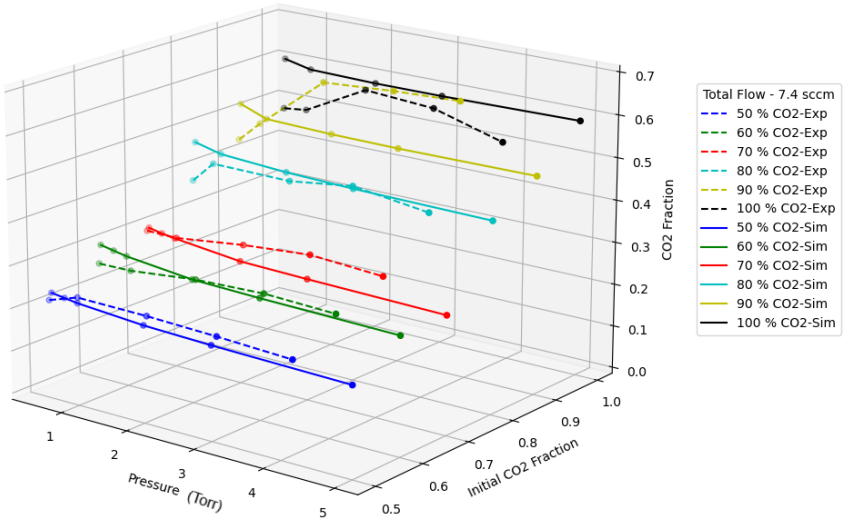

Figure 4.10: Experimental and simulation equilibrium concentration values for CO_2, with current of 40mA and varying pressure, with a total flow of 7.40sccm.

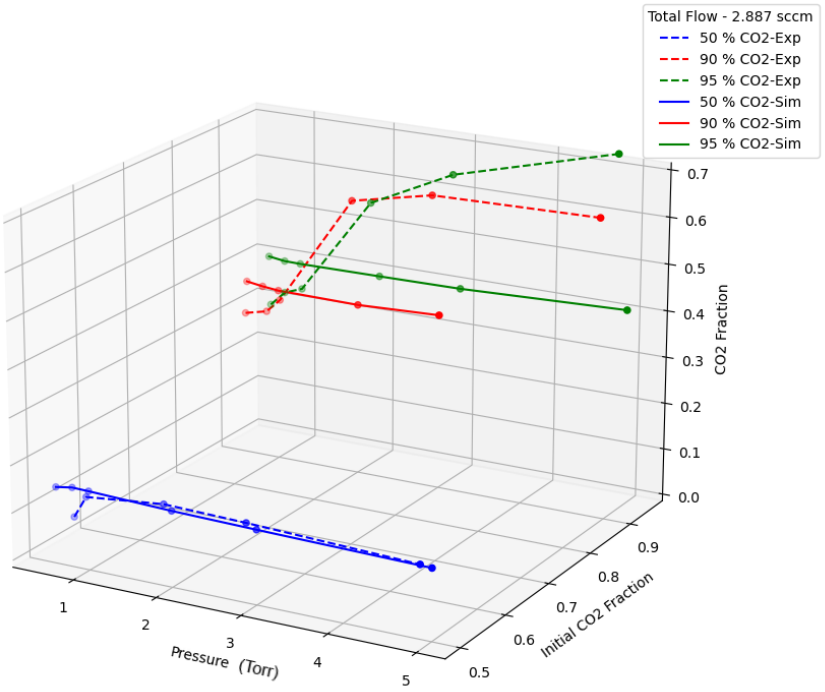

Figure 4.11: Experimental and simulation equilibrium concentration values for CO_2,with current of 40mA and varying pressure, with a total flow of 2.89sccm.

We now turn our attentions to the concentration results for a varying pressure and initial flow of CO_2, while keeping current at 40 mA. We start by looking at the values for the CO_2 species, which are present in figures 4.10 and 4.11 . First, the simulation results indicate that concentration does not have a significant variation with the pressure, which is not what is observed in the experimental results. Secondly, we see that, the equilibrium concentration of CO_2 increases with the increase in the flow of CO_2, which makes total sense. Finally, comparing the experimental results with the simulation, there

are two distinct situations: When the flow of CO_2 is $\leq 80\%$, the agreement is almost perfect with the experimental data. When the flow of CO_2 is ≥ 90, the results are not so good, since the variation with the pressure is not the same in both situations. This becomes especially problematic when the total flow is 2.89 sccm, and there are major discrepancies between the results, that can reach almost 30%.

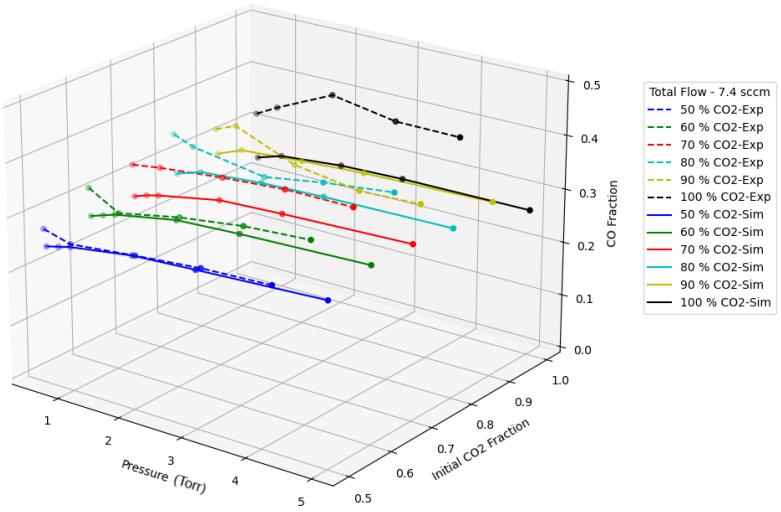

Figure 4.12: Experimental and simulation equilibrium concentration values for CO, with varying pressure, current of 40 mA and with a total flow of 7.40sccm.

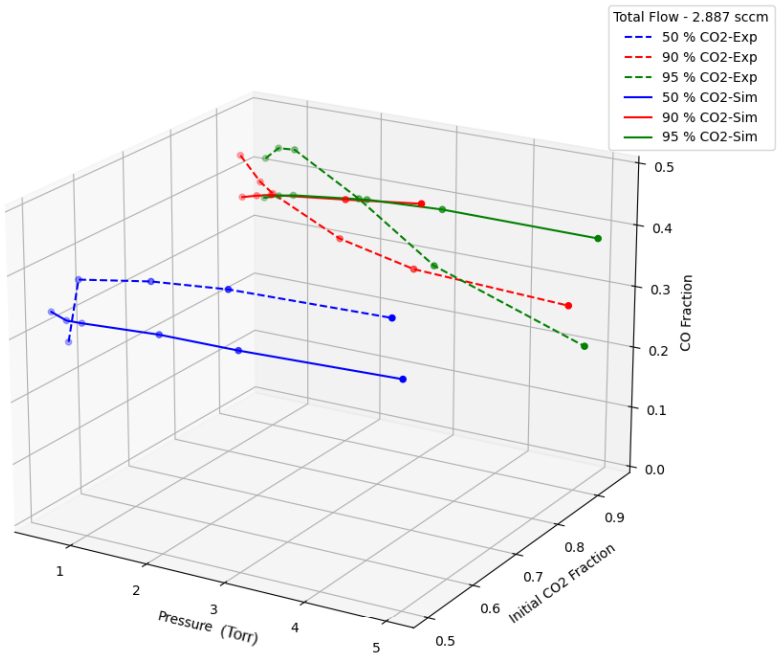

Figure 4.13: Experimental and simulation equilibrium concentration values for CO, with varying pressure, current of 40 mA and a total flow of 2.89sccm.

The results for the CO concentration are presented in figures 4.12 and 4.13. It is possible to see a slight increase of the concentration with the increase of pressure. Furthermore, the results are much more in agreement with the experiment, for initial CO_2 fractions between 50% and 80 %. Also, we can see that when the total flow pumped is 2.89 sccm, the results are worst compared to 7.40 sccm. Overall, it is possible to say that the concentration of CO is quite stable with the variation of pressure and of the

initial mixture, making up between 20 and 25 % of the mixture, when the total flow is 7.40 sccm and between 30 and 35% of the mixture, when the total flow is 2.89 sccm. One explanation for this behavior is the fact that the outlet flux is one of the main loss mechanisms for the CO molecule.

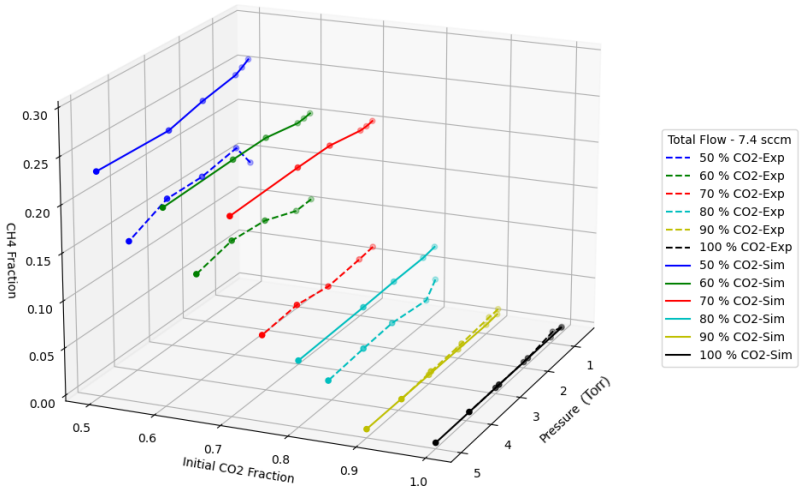

Figure 4.14: Experimental and simulation equilibrium concentration values for CH_4, with varying pressure, current of 40 mA and with a total flow of 7.40sccm.

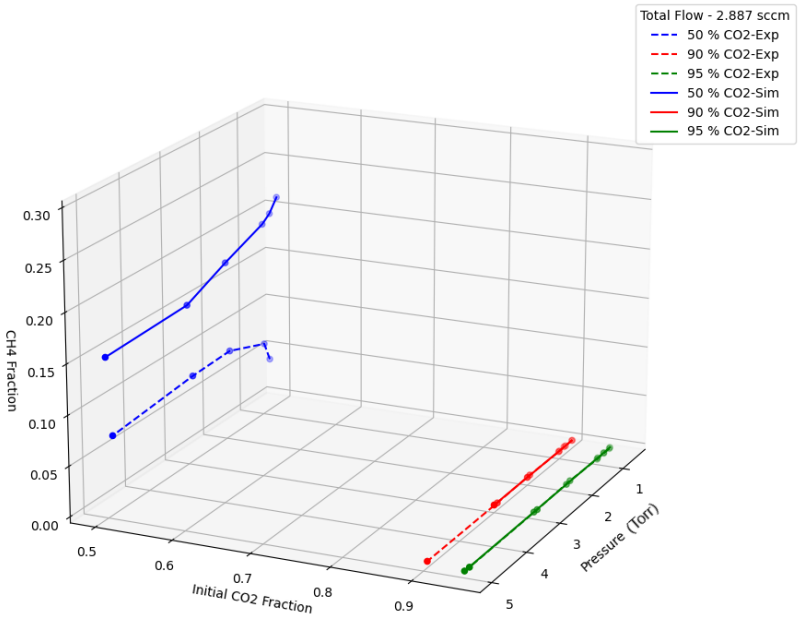

Figure 4.15: Experimental and simulation equilibrium concentration values for CH_4, with varying pressure, current of 40 mA and a total flow of 2.89sccm.

The results for the CH_4 molecule are present in figures 4.14 and 4.15. For the simulation results, there is a slight decrease increase in the concentration of CH_4 with the pressure. Furthermore, the equilibrium concentration reduces very much with the increase in the initial amount of CO_2 in the mixture (and thus less CH_4). Comparing the results with the experimental ones, there is clearly an overestimation of CH_4 of between 10% to 15% for all of the pressure conditions, when the initial amount of CO_2 is lower than 10 %. Finally it is also possible to see that for low amounts of CH_4 in the initial mixture ($\leq 10\%$), the molecules are almost all destroyed, since its concentrations are negligible.

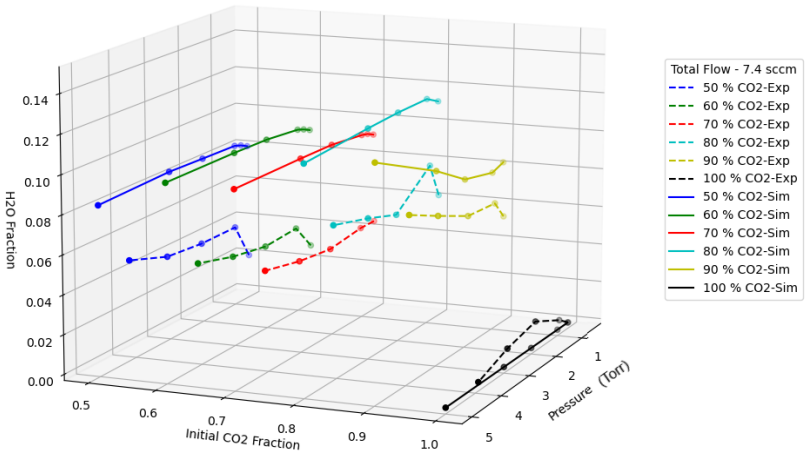

Figure 4.16: Experimental and simulation equilibrium concentration values for H_2O, with varying pressure, current of 40 mA and with a total flow of 7.40sccm.

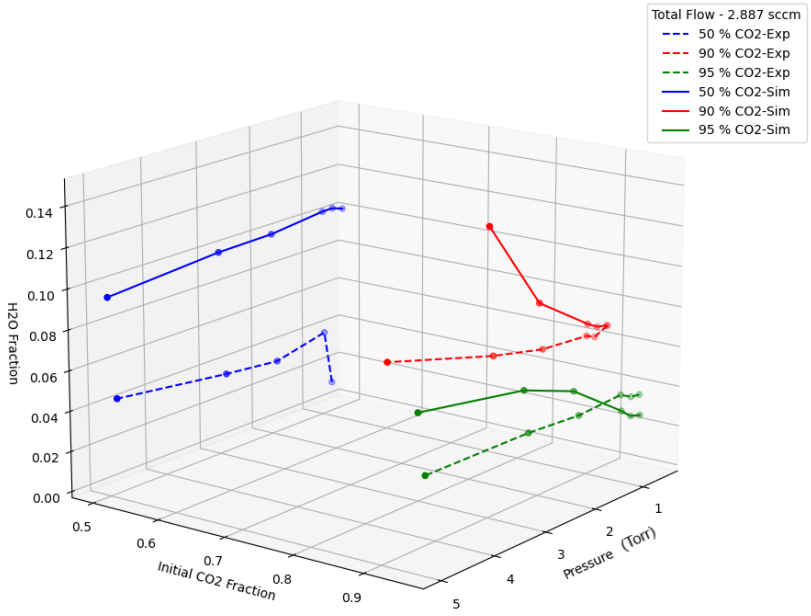

Figure 4.17: Experimental and simulation equilibrium concentration values for H_2O, with varying pressure, current of 40 mA and a total flow of 2.89sccm.

The results for the H_2O molecule are present in figures 4.16 and 4.17. We can see that when the initial CO_2 fraction is ≤ 80, there is a decrease of the concentration of H_2O with the pressure. However, when the initial CO_2 fraction is > 80, the opposite is observed, and the concentration is increased with the increase of pressure. Finally, comparing the experimental with the simulation results, we can see that there is an overestimation of the H_2O concentration, of about 3% to 10 %, for a vast majority of the conditions.

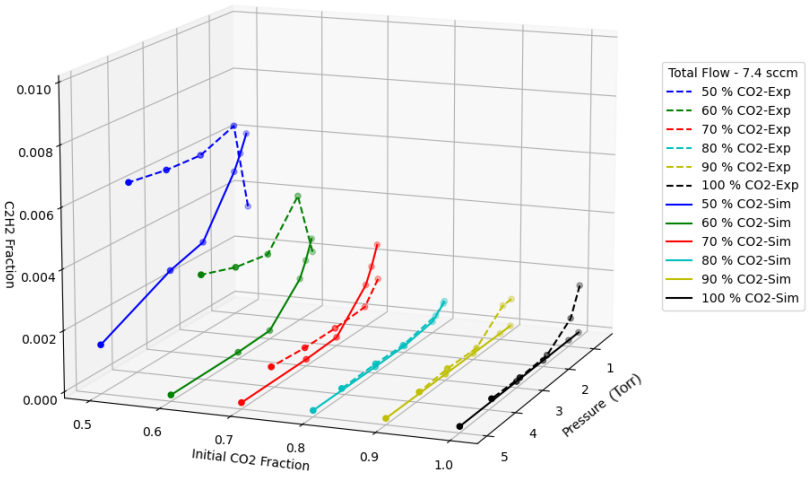

Figure 4.18: Experimental and simulation equilibrium concentration values for C_2H_2, with varying pressure, current of 40 mA and with a total flow of 7.40sccm.

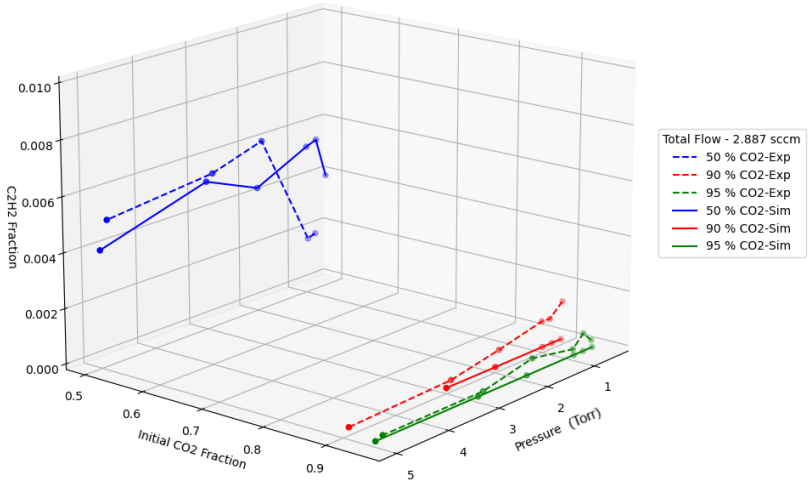

Figure 4.19: Experimental and simulation equilibrium concentration values for C_2H_2, with varying pressure, current of 40 mA and a total flow of 2.89sccm.

The results associated with the change of concentration of C_2H_2 as a function of the gas pressure and initial CO_2 flow are shown in figures 4.18 and 4.19. It is worth mentioning that, since this molecule has a very low concentration, we expect lower accuracy on the experimental measures. Despite this, we can see that for the simulation results, there is a steady decrease of the C_2H_2 for almost all conditions with the pressure, except when the total flow is 2.89 sccm and the initial CO_2 fraction is 50 %. Comparing with the experimental results, overall, there is not a very good agreement between the simulated and the experimental concentrations. However, we can see that the simulation indicates that the concentration of the molecule is always lower 1 % and that this concentration increases when the initial CH_4 fraction is greater, which is consistent with the experimental results.

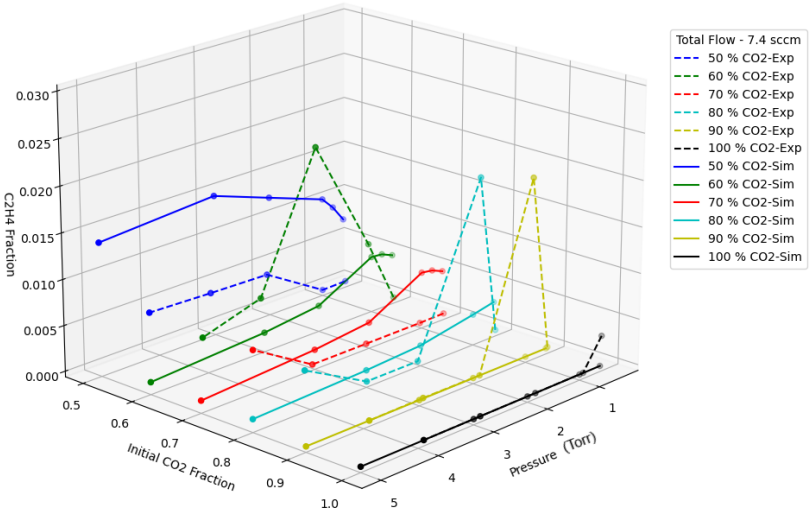

Figure 4.20: Experimental and simulation equilibrium concentration values for C_2H_4, with varying pressure, current of 40 mA and with a total flow of 7.40sccm.

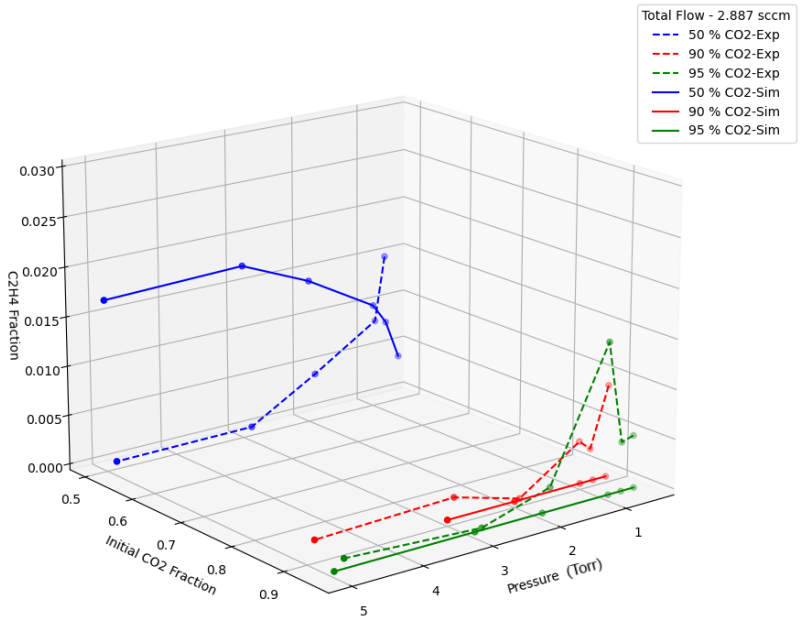

Figure 4.21: Experimental and simulation equilibrium concentration values for C_2H_4, with varying pressure, current of 40 mA and a total flow of 2.89sccm.

In figures 4.20 and 4.21 we present the concentration results for the C_2H_4 molecule . We can see that, for most conditions, the concentration decreases with the increase of pressure, and this trend is only not followed when the initial CO_2 fraction is 50 %. Furthermore, the concentration of C_2H_2 decreases when the initial CH_4 fraction also decreases, which is expected. As for the comparison with the experimental results, the results are not very consistent. In many cases, there is an overestimation of the C_2H_4 compared to the experimental results. Furthermore, the sudden increase of the C_2H_4 when the pressure is equal to 1 Torr, is not replicated in the simulation.

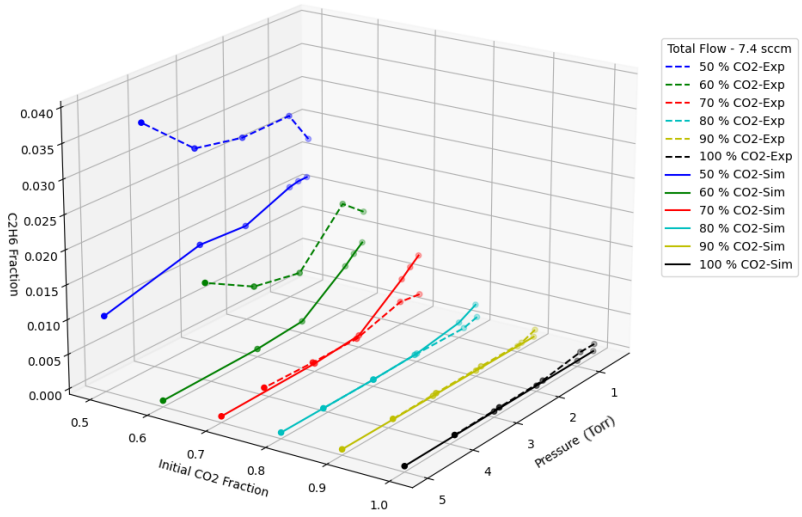

Figure 4.22: Experimental and simulation equilibrium concentration values for C_2H_6, with varying pressure, current of 40 mA and with a total flow of 7.40sccm.

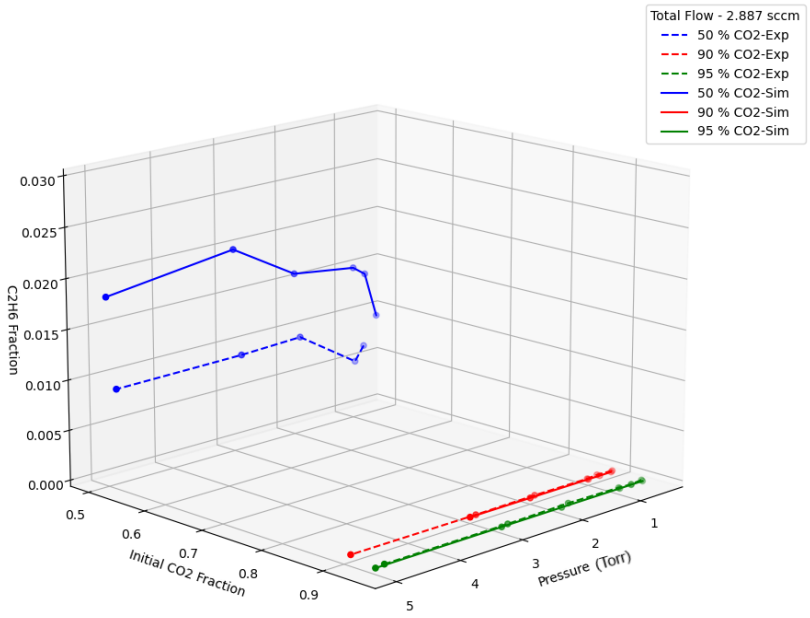

Figure 4.23: Experimental and simulation equilibrium concentration values for C_2H_6, with varying pressure, current of 40 mA and a total flow of 2.89sccm.

Finally, the results for the molecule C_2H_6 are present in figures 4.22 and 4.23. Overall, we can see that the concentration decreases with the increase of pressure for almost every condition, except when the initial flow of CO_2 is 50% and the total flow is 2.89 sccm. Furthermore, an initial amount of CH_4 in the mixture is also correlated to an increase in the amount of C_2H_6 , which is expected. Finally comparing with the experimental results, the results are not very consistent. Despite this, for lower values of CH_4 flow, the amount of C_2H_6 becomes residual, both on the experimental and simulation data.

Overall, the simulation results of the density are satisfactory. It was possible to simulate all the relevant species and the dependence with plasma parameters. Although the agreement with experiment was not always very good, the predicted orders of magnitude and several general trends were correctly described. For most conditions, the errors between the experimental and simulated concentrations were between 2% and 15 %, despite some instances, when the total flow was 2.89 sccm, where the error

could go up to 30 %. Furthermore, for some of the species, like CH_4 and H_2O, an error of about 5 % to 15 % in the concentration was consistently found, which is where major improvements in the model can happen.

We now turn our attention to the different chemical reactions that influence the plasma composition. On tables 4.2 to 4.5 , the main mechanisms that responsible for the creation and destruction of the most important species of the plasma are exposed. For a more consistent approach, this analysis was made for a varying pressure and different initial plasma composition, and a constant total flow of 7.40 sccm and current of 40 mA. Only reactions with a density contribution of above 1 % were considered. Both the inflow and outflow reactions were neglected.

Species	Process	Number	Reaction	Max (%)	Min (%)
CO_2	Creation	F1CO_2	CO(a3P)+CO(X) $\longrightarrow$ CO2(X)+C(X)	33.69	8.66
		F2CO_2	CO(a3P)+O2(X) $\longrightarrow$ CO2(X)+O(3P)	49.04	$\leq$1.00
		F3CO_2	CO(X)+OH(X) $\longrightarrow$ H(1s)+CO2(X)	67.62	$\leq$1.00
		F4CO_2	CO2(+,X)+O(3P) $\longrightarrow$ O(+,gnd)+CO2(X)	7.72	$\leq$1.00
		F5CO2	CO2(+,X)+Wall $\longrightarrow$ CO2(X)	12.23	$\leq$ 1.00
		F6CO2	O(-,gnd)+CO(X) $\longrightarrow$ e+CO2(X)	36.94	7.22
		F7CO2	O(3P)+CO(X)+CO2(X) $\longrightarrow$ CO2(X)+CO2(X)	7.60	$\leq$1.00
		F8CO_2	O(3P)+HCO(X) $\longrightarrow$ H(1s)+CO2(X)	47.84	$\leq$1.00
	Destruction	D1CO2	CH(X)+CO2(X) $\longrightarrow$ H(1s)+2CO(X)	8.45	$\leq$1.00
		D2CO_2	CH2(X)+CO2(X) $\longrightarrow$ CH2O(X)+CO(X)	15.64	$\leq$1.00
		D3CO_2	CO(a3P)+CO2(X) $\longrightarrow$ 2CO(X)+O(3P)	33.84	15.84
		D4CO_2	e+CO2(X) $\longrightarrow$ CO(X)+O(-,gnd)	3.22	1.19
		D5CO_2	e+CO2(X) $\longrightarrow$ e+CO(X)+O(1D)	78.12	49.53

Table 4.2: Relevant creation and destruction processes for the CO_2 molecule, with the following plasma conditions: Discharge current 40 mA; Varying gas pressure from 0.6 Torr to 5 Torr; Total inlet gas flow of 7.40 sccm, composed of CO_2 and CH_4. Varying initial flow of CO_2, from 50 % to 100% of the total gas flow.

Species	Process	Number	Reaction	Max (%)	Min (%)
CO	Creation	F1 CO	C2H5(X)+HCO(X)⟶C2H6(X)+CO(X)	3.25	≤1.00
		F2CO	CH(X)+CO2(X)⟶H(1s)+2CO(X)	3.23	≤ 1.00
		F3 CO	CH2(X)+CO2(X)⟶CH2O(X)+CO(X)	2.12	≤ 1.00
		F4 CO	CH2(X)+O(3P)⟶CO(X)+2H(1s)	1.55	≤ 1.00
		F5CO	CH3(X)+HCO(X)⟶CH4(X)+CO(X)	1.99	≤ 1.00
		F6CO	CO(a3P)+CO(X)⟶CO(X)+CO(X)	71.12	22.67
		F7CO	CO(a3P)+CO2(X)⟶2CO(X)+O(3P)	15.34	8.64
		F8CO	CO(a3P)+CO2(X)⟶CO(X)+CO2(X)	7.67	4.32
		F9CO	CO(a3P)+O(3P)⟶CO(X)+O(3P)	31.30	≤ 1.00
		F10CO	CO(a3P)+O2(X)⟶CO(X)+2O(3P)	6.27	1.06
		F11CO	e+CO2(X)⟶e+CO(X)+O(1D)	25.64	6.72
		F12CO	H(1s)+HCO(X)⟶CO(X)+H2(X)	3.74	≤ 1.00
		F13CO	O(3P)+HCO(X)⟶CO(X)+OH(X)	2.24	≤ 1.00
		F14CO	O2(X)+C(X)⟶CO(X)+O(3P)	1.13	≤ 1.00
	Destruction	D1CO	CO(a3P)+CO(X)⟶CO2(X)+C(X)	1.37	≤ 1.00
		D2CO	CO(X)+OH(X)⟶H(1s)+CO2(X)	6.33	≤ 1.00
		D3CO	e+CO(X)<⟶e+CO(a3P)	96.87	91.46
		D4CO	e+CO(X)⟶e+C(X)+O(3P)	1.12	≤ 1.00
		D5CO	O(-,gnd)+CO(X)⟶e+CO2(X)	3.02	≤ 1.00

Table 4.3: Relevant creation and destruction processes for the CO molecule, with the following plasma conditions: Varying gas pressure from 0.6 Torr to 5 Torr; Total inlet gas flow of 7.40 sccm, composed of CO_2 and CH_4. Varying initial flow of CO_2, from 50 % to 100% of the total gas flow.

Species	Process	Number	Reaction	Max (%)	Min (%)
CH4	Creation	F1 CH4	C2H5(X)+CH3(X)⟶C2H4(X)+CH4(X)	4.74	≤ 1.00
		F2 CH4	CH3(X)+H(1s)⟶CH4(X)	99.95	63.34
		F3 CH4	CH3(X)+HCO(X)⟶CH4(X)+CO(X)	31.62	≤ 1.00
	Destruction	D1 CH4	CH4(X)+O(1D)⟶CH3(X)+OH(X)	89.90	29.47
		D2 CH4	CH4(X)+O(3P)⟶CH3(X)+OH(X)	4.76	≤ 1.00
		D3 CH4	CH4(X)+OH(X)⟶CH3(X)+H2O(X)	5.01	≤ 1.00
		D4 CH4	e+CH4(X)⟶e+CH2(X)+H2(X)	34.63	≤ 1.00
		D5 CH4	e+CH4(X)⟶e+CH3(X)+H(1s)	31.74	≤ 1.00
		D6 CH4	O(1D)+CH4(X)⟶CH2O(X)+H2(X)	9.77	3.27

Table 4.4: Relevant creation and destruction processes for the CH_4 molecule, with the following plasma conditions: Varying gas pressure from 0.6 Torr to 5 Torr; Total inlet gas flow of 7.40 sccm, composed of CO_2 and CH_4. Varying initial flow of CO_2, from 50 % to 100% of the total gas flow.

Species	Process	Number	Reaction	Max (%)	Min (%)
H2O	Creation	F1 H2O	C2H5(X)+OH(X)-C2H4(X)+H2O(X)	6.62	≤ 1.00
		F2 H2O	C2H6(X)+OH(X)$\longrightarrow$C2H5(X)+H2O(X)	9.46	≤ 1.00
		F3 H2O	CH2O(X)+OH(X)$\longrightarrow$H2O(X)+HCO(X)	60.97	3.64
		F4 H2O	CH4(X)+OH(X)$\longrightarrow$CH3(X)+H2O(X)	12.49	≤ 1.00
		F5 H2O	H2(X)+OH(X)$\longrightarrow$H2O(X)+H(1s)	9.47	≤ 1.00
		F6 H2O	OH(X)+H(1s)$\longrightarrow$H2O(X)	95.25	10.80
		F7 H2O	OH(X)+HCO(X)$\longrightarrow$CO(X)+H2O(X)	3.64	≤ 1.00
	Destruction	D1 H2O	CH2(X)+H2O(X)$\longrightarrow$CH3(X)+OH(X)	30.92	≤ 1.00
		D2 H_2O	e+H2O(X)$\longrightarrow$e+H(1s)+OH(X)	99.98	69.08

Table 4.5: Relevant creation and destruction processes for the H_2O molecule, with the following plasma conditions: Varying gas pressure from 0.6 Torr to 5 Torr; Total inlet gas flow of 7.40 sccm, composed of CO_2 and CH_4. Varying initial flow of CO_2, from 50 % to 100% of the total gas flow.

A analysis of the results for each species is given below:

- **CO_2 Creation** : For the creation process, when the flow of CO_2 is lower (between 50% and 80 %) F1CO_2, F3Co_2 and F5CO_2 are the most important processes, to take into account. While F3$CO_2$is favoured by higher pressures, F5CO_2 contributions decrease with the increase of pressure. When the flow of CO_2 is higher ($\geq$ 90 %), but there is still some CH_4, F6CO_2, F2CO_2 and F8Co_2 become the most relevant processes of creation to take into account. While F2CO_2 and F6CO_2 is favoured by high pressures, the opposite effect happens for F8CO_2. Finally, when the flow is 100 % CO_2 F2CO_2, F4CO_2, F7CO_2 and F7CO_2 become the most relevant process, with a reasonable contribution from F1CO_2.

- **CO_2 Destruction** The most relevant processes for the destruction of CO_2 are D1CO_2, D2CO_2, D3CO_2 and D5CO_2. D1CO_2 and D2CO_2 are most favoured when the initial flow of CO_2 is between 50% and 80 %. Furthermore, when the pressure increases, the contribution from D1CO_2 decreases, while the contribution from D2CO_2 increases. D3CO_2 contribution to the density is for most conditions $\approx 30\%$, except when the initial flow is 100 % CO_2, which makes the contribution decline to lower values. It is also favoured by the increase in the pressure. D5CO_2 is also a very important process. In most conditions, its contribution is close to 50 %, but when the flow of CO_2 is $\geq 90\%$ its contribution increases, and can reach 78 %. This process is also favoured by lower pressures.

- **CO Creation** : F6CO, F7CO, F8CO, F9CO, F10CO and F11CO are the most relevant processes for the creation of CO. F6CO is a very important process, with a contribution of about 50 % to 70 % for almost all conditions and it is favoured by higher pressures, although When the flow is 100 % CO_2, the contribution is reduced to 20%-30%. F7CO contribution is topically between 10% and 15 % and its contribution increases when the initial flow of CO_2 is higher. F8CO is a also a relevant process, which contribution increases with the initial flow of CO_2 and with the increase of pressure. F9CO, F10CO and F11CO are processes that usually do not have a relevant contribution, except when the flow of CO_2 reaches 100 %, where the maximum values of the contribution shown in table 4.3 are reached.

- **CO Destruction**: Process D3CO is the main reaction responsible for the destruction of CO, for all conditions. Typically it accounts for 93 to 96 % of the total density. This value tends to decrease as the initial flow of CO_2 increases, and this is were processes D1 CO, D2CO, D4CO and D5CO become more favourable and also contribute for the destruction of CO.

- **CH_4 Creation**: For the creation of CH_4, $F2CH_4$ is the most important reaction. The contribution is between 85% and 93 % for most of the conditions, and increases with the pressure. Under these conditions, reaction $F3CH_4$ accounts for the rest of the density, with a contribution between 7% and 15%. There are two sets of conditions that don't follow this rule: First, when the flow is 50 % CO_2, the contribution of $F2CH_4$ is reduced up to 63 %, while $F3CH_4$ increases up to 32 % and $F1CH_4$ increases up to almost 5 %. Secondly, when the flow of CO_2 is 100 %, reaction $F3CH_4$ accounts for basically 100 % of the creation of CH_4.

- **CH_4 Destruction** $F1CH_4$ is a very important reaction for the destruction of CH_4. Its contribution to the density increases with the pressure and the CO_2 flow, going from 30 % to 87 %. $F6CH_4$ also has this behavior, at a smaller contribution, going from 3% to 10%. $F4CH_4$ and $F5CH_4$ have the opposite behavior than $F1CH_4$: It decreases with the increase in pressure and CO_2 flow, from $\approx 33\%$ to $\leq 1\%$. $F2CH_4$ is only relevant for high values of CO_2 flow. Finally, $F3CH_4$ has a big variation with the increase of pressure, going from 1% to 5% in its contribution, but is only relevant when the CO_2 flow is $\geq 90\%$

- **H_2O Creation** $C3H_2O$ is an important process for the creation of H_2O. It typically accounts for 30% to 40% of the total density, but there are two exceptions. When the CO_2 flow is 50 % this value increases, and it can reach 61 % at 5 Torr. On the other hand, when the CO_2 flow is 90 %, this value is reduced, and it contribute only to 3% of the total density. $C5H_2O$ has the opposite trend of $C3H_2O$: It usually signifies 40% to 50 % of the total density of H_2O, but when the CO_2 flow is 50 %, this value is reduced, and can reach 4 % and when the CO_2 flow is 90 %, it has a very big increase and it can contribute to 90 % of the creation of H_2O. For $C1H_2O$ and $C2H_2O$ are only relevant reactions when the CO_2 flow is 50 %. At the highest pressures, they can reach a contribution of 6 & and 9%, to the total density. Finally processes $C4H_2O$ and $C5H_2O$ are especially relevant at higher pressures, and can reach a contribution of 12% and 9%, respectively, while being almost negligible at lower pressures.

- **H_2O Destruction** There are two main contributions for the destruction of the H_2O molecule. $D2H_2O$ typically has a contribution of 80 % to 95 % to the total density, that decreases with the increase of pressure. This is true for almost all of the conditions, except when the CO_2 flow is 90%, when the contribution of $D2H_2O$ can reach 99% of the total density. $D1H_2O$ has always the opposite behavior of $D2H_2O$, since these are the only two reactions necessary to understand the destruction of H_2O.

Chapter 5

Conclusion

5.1 Achievements

In this work, we carried out an experimental and modelling study of CO_2-CH_4 plasmas, sustained under gas pressures between 0.5 and 5 torr and discharge currents ranging from 10 to 50 mA. During the experimental campaign we investigated several parameters, including the gas temperature and the plasma composition. These parameters were investigated as function of input gas pressure, gas flow and initial gas mixture. In respect to gas temperature analysis, the results revealed that the emission of CO molecules (measured through OES) can be used as a thermometer to characterize the discharge heating. This is particularly relevant for CO_2 non-thermal discharges given that CO is expected to be a direct product of the CO_2 decomposition. This approach based on OES also offers a huge advantage from the practical point of view when compared with other plasma diagnostics (e.g. FTIR) which require a much more complex experimental setup.

Regarding the broadband continuous emission of CO_2-CH_4 plasmas, an easy-to-handle solution to measure the reduced electric field was developed, in the case of easy access to the broadband emission. This approach still needs more validation, so that the dependence of the reduced electric field on the intensity of the broadband emission is determined for a wider range of plasma conditions.

Regarding the studies associated to plasma composition, it is worth noticing that in this work we used FTIR to follow the evolution of not only CO_2 and CH_4 species, but also several decomposition products, including CxHy. These results are particularly relevant to the validation of future models focused on CO_2-CH_4 plasma chemistry.

On the modeling section, a kinetic model for CO_2/CH_4 was developed, which included 23 species and more than 250 reactions. This model was then used to replicate the experimental conditions in chapter 3 and good agreement between experimental results and modelling was obtained. Despite the fact that the agreement with experiment was not always excellent, the expected orders of magnitude and some broad patterns were accurately characterized. Finally, the most relevant processes determining the plasma chemical composition and its variability with experimental conditions were investigated.

5.2 Future work

In spite of the analysis of CO_2-CH_4 glow discharges using modelling and different plasma diagnostic techniques, future work is still required to progress towards a complete understanding of plasma-based CO_2 reforming.

First, regarding the gas temperature study, it would be very interesting to compare the gas temperature measurements obtained through FTIR measurements and those obtained through the rotational temperature fit, for the same plasma conditions, in order to determine under what conditions this is a valid method of measuring this parameter.

Second, regarding the broadband emission, it would of great utility to further develop the relation between the broadband intensity and the reduced electric field .This would provide a very simple way of measuring the reduced electric field, given that the broadband emission is accessible.

Finally, in terms of kinetic modeling, since the rate coefficients used were based on the literature available, which is not always consistent, a sensitivity study of the impact of these variations in the rate coefficients in the model is necessary.

References

[1] A. Fridman, *Plasma Chemistry*. Cambridge University Press, 2008. DOI: 10.1017/CBO9780511546075.

[2] I. Adamovich, S. D. Baalrud, A. Bogaerts, P. J. Bruggeman, M. Cappelli, V. Colombo, U. Czarnetzki, U. Ebert, J. G. Eden, P. Favia, D. B. Graves, S. Hamaguchi, G. Hieftje, M. Hori, I. D. Kaganovich, U. Kortshagen, M. J. Kushner, N. J. Mason, S. Mazouffre, S. M. Thagard, H.-R. Metelmann, A. Mizuno, E. Moreau, A. B. Murphy, B. A. Niemira, G. S. Oehrlein, Z. L. Petrovic, L. C. Pitchford, Y.-K. Pu, S. Rauf, O. Sakai, S. Samukawa, S. Starikovskaia, J. Tennyson, K. Terashima, M. M. Turner, M. C. M. van de Sanden, and A. Vardelle, "The 2017 plasma roadmap: Low temperature plasma science and technology", vol. 50, no. 32, p. 323 001, Jul. 2017. DOI: 10.1088/1361-6463/aa76f5.

[3] U. O. of Science (SC) (United States), "Plasma: at the frontier of scientific discovery", 2017. DOI: https://doi.org/10.2172/1615243.

[4] IPCC, " Climate Change 2021: The Physical Science Basis. Contribution of Working Group I to the Sixth Assessment Report of the Intergovernmental Panel on Climate Change [Masson-Delmotte, V., P. Zhai, A. Pirani, S.L. Connors, C. Péan, S. Berger, N. Caud, Y. Chen, L. Goldfarb, M. I. Gomis, M. Huang, K. Leitzell, E. Lonnoy, J. B. R. Matthews, T. K. Maycock, T. Waterfield, O. Yelekçi, R. Yu and B. Zhou (eds.)]. ", *Cambridge University Press, In Press*, 2021. [Online]. Available: https://www.ipcc.ch/report/ar6/wg1/#SPM.

[5] Goede, Adelbert P. H., "Co2 neutral fuels", *EPJ Web Conf.*, vol. 189, p. 00 010, 2018. [Online]. Available: https://doi.org/10.1051/epjconf/201818900010.

[6] B. Klarenaar, "Vibrational kinetics of co2 in non-thermal plasma", English, Jun. 2018, Proefschrift.

[7] T. Silva, M. Grofulović, L. Terraz, C. D. Pintassilgo, and V. Guerra, "Modelling the input and relaxation of vibrational energy in CO2 plasmas", *Journal of Physics D: Applied Physics*, vol. 51, no. 46, p. 464 001, Sep. 2018. DOI: 10.1088/1361-6463/aadbd7.

[8] I. Suzuki, "General anharmonic force constants of carbon dioxide", *Journal of Molecular Spectroscopy*, vol. 25, no. 4, pp. 479–500, 1968, ISSN: 0022-2852. DOI: https://doi.org/10.1016/S0022-2852(68)80018-9.

[9] "Appendix d: Information on some diatomic molecules for the identification and processing of low-temperature plasma spectra", pp. 505–567, 2009. DOI: https://doi.org/10.1002/9783527627509.app4.

[10] B. L. M. Klarenaar, R. Engeln, D. C. M. van den Bekerom, M. C. M. van de Sanden, A. S. Morillo-Candas, and O. Guaitella, "Time evolution of vibrational temperatures in a CO2glow discharge measured with infrared absorption spectroscopy", *Plasma Sources Science and Technology*, vol. 26, no. 11, p. 115 008, Oct. 2017. DOI: 10.1088/1361-6595/aa902e.

[11] T. Lee, J. Martin, and P. Taylor, "An accurate ab initio quartic force field and vibrational frequencies for ch4 and isotopomers", *The Journal of Chemical Physics*, vol. 102, Feb. 1995. DOI: 10.1063/1.469398.

[12] L. A. University of California, "Characteristic vibrations of CH_4", Aug. 2021. [Online]. Available: http://www2.ess.ucla.edu/~schauble/MoleculeHTML/CH4_html/CH4_page.html.

[13] R. Snoeckx and A. Bogaerts, "Plasma technology – a novel solution for co2 conversion?", *Chem. Soc. Rev.*, vol. 46, pp. 5805–5863, 19 2017. DOI: 10.1039/C6CS00066E.

[14] Y. Fan, J.-y. Ren, W. Onstot, J. Pasale, T. T. Tsotsis, and F. N. Egolfopoulos, "Reactor and technical feasibility aspects of a co2 decomposition-based power generation cycle, utilizing a high-temperature membrane reactor", *Industrial & Engineering Chemistry Research*, vol. 42, no. 12, pp. 2618–2626, 2003. DOI: 10.1021/ie020980r.

[15] L. Polak and D. Slovetsky, "Electron impact induced electronic excitation and molecular dissociation", *International Journal for Radiation Physics and Chemistry*, vol. 8, no. 1, pp. 257–282, 1976, ISSN: 0020-7055. DOI: https://doi.org/10.1016/0020-7055(76)90070-X.

[16] A. Cenian, A. Chernukho, V. Borodin, and G. Śliwiński, "Modeling of plasma-chemical reactions in gas mixture of co2 lasers i. gas decomposition in pure co2 glow discharge", *Contributions to Plasma Physics*, vol. 34, no. 1, pp. 25–37, 1994. DOI: https://doi.org/10.1002/ctpp.2150340105.

[17] A. Cenian, A. Chernukho, and V. Borodin, "Modeling of plasma-chemical reactions in gas mixture of co2 lasers. ii. theoretical model and its verification", *Contributions to Plasma Physics*, vol. 35, no. 3, pp. 273–296, 1995. DOI: https://doi.org/10.1002/ctpp.2150350309.

[18] R. Aerts, T. Martens, and A. Bogaerts, "Influence of vibrational states on co2 splitting by dielectric barrier discharges", *The Journal of Physical Chemistry C*, vol. 116, no. 44, pp. 23 257–23 273, 2012. DOI: 10.1021/jp307525t. eprint: https://doi.org/10.1021/jp307525t. [Online]. Available: https://doi.org/10.1021/jp307525t.

[19] T. Kozák and A. Bogaerts, "Splitting of CO2by vibrational excitation in non-equilibrium plasmas: A reaction kinetics model", *Plasma Sources Science and Technology*, vol. 23, no. 4, p. 045 004, Jun. 2014. DOI: 10.1088/0963-0252/23/4/045004.

[20] T. Silva, M. Grofulović, B. L. M. Klarenaar, A. S. Morillo-Candas, O. Guaitella, R. Engeln, C. D. Pintassilgo, and V. Guerra, "Kinetic study of low-temperature CO2plasmas under non-equilibrium conditions. i. relaxation of vibrational energy", *Plasma Sources Science and Technology*, vol. 27, no. 1, p. 015 019, Jan. 2018. DOI: 10.1088/1361-6595/aaa56a.

[21] M. Grofulović, T. Silva, B. L. M. Klarenaar, A. S. Morillo-Candas, O. Guaitella, R. Engeln, C. D. Pintassilgo, and V. Guerra, "Kinetic study of CO2 plasmas under non-equilibrium conditions. II. input of vibrational energy", *Plasma Sources Science and Technology*, vol. 27, no. 11, p. 115 009, Nov. 2018. DOI: 10.1088/1361-6595/aadb60.

[22] L. Terraz, T. Silva, A. Morillo-Candas, O. Guaitella, A. Tejero-del-Caz, L. L. Alves, and V. Guerra, "Influence of n2 on the CO2 vibrational distribution function and dissociation yield in non-equilibrium plasmas", vol. 53, no. 9, p. 094 002, Dec. 2019. DOI: 10.1088/1361-6463/ab55fb.

[23] A. S. Morillo-Candas, T. Silva, B. L. M. Klarenaar, M. Grofulović, V. Guerra, and O. Guaitella, "Electron impact dissociation of CO2", vol. 29, no. 1, 01LT01, Jan. 2020. DOI: 10.1088/1361-6595/ab6075.

[24] T. Silva, M. Grofulović, L. Terraz, C. Pintassilgo, and V. Guerra, "Dynamics of gas heating in the afterglow of pulsed co2 and co2–n2 glow discharges at low pressure", *Plasma Chemistry and Plasma Processing*, vol. 40, May 2020. DOI: 10.1007/s11090-020-10061-7.

[25] V. A. Legasov, V. K. Zhivotov, E. G. Krasheninnikov, M. F. Krotov, B. I. Patrushev, V. D. Rusanov, G. V. Rykunov, A. M. Spektor, A. A. Fridman, and G. V. Sholin, "Nonequilibrium plasma-chemical process of the decomposition of CO2 in HF and UHF discharges", *Akademiia Nauk SSSR Doklady*, vol. 238, pp. 66–69, Jan. 1978.

[26] I. P. Butylkin, V. K. Zhivotov, E. G. Krasheninnikov, M. F. Krotov, V. D. Rusanov, I. V. Tarasov, and A. A. Fridman, "Plasma-chemical process of CO2 dissociation in a nonequilibrium microwave discharge", *Zhurnal Tekhnicheskoi Fiziki*, vol. 51, pp. 925–931, May 1981.

[27] A. Bogaerts and E. C. Neyts, "Plasma technology: An emerging technology for energy storage", *ACS Energy Letters*, vol. 3, no. 4, pp. 1013–1027, 2018. DOI: 10.1021/acsenergylett.8b00184.

[28] W. Bongers, H. Bouwmeester, B. Wolf, F. Peeters, S. Welzel, D. van den Bekerom, N. den Harder, A. Goede, M. Graswinckel, P. W. Groen, J. Kopecki, M. Leins, G. van Rooij, A. Schulz, M. Walker, and R. van de Sanden, "Plasma-driven dissociation of co2 for fuel synthesis", *Plasma Processes and Polymers*, vol. 14, no. 6, p. 1 600 126, 2017. DOI: https://doi.org/10.1002/ppap.201600126. eprint: https://onlinelibrary.wiley.com/doi/pdf/10.1002/ppap.201600126.

[29] T. Silva, N. Britun, T. Godfroid, and R. Snyders, "Optical characterization of a microwave pulsed discharge used for dissociation of CO2", *Plasma Sources Science and Technology*, vol. 23, no. 2, p. 025 009, Mar. 2014. DOI: 10.1088/0963-0252/23/2/025009.

[30] S. Tiago, B. Nikolay, G. Thomas, and S. Rony, "Understanding co2 decomposition in microwave plasma by means of optical diagnostics", *Plasma Processes and Polymers*, vol. 14, no. 6, p. 1 600 103, 2017. DOI: https://doi.org/10.1002/ppap.201600103.

[31] N. den Harder, D. C. M. van den Bekerom, R. S. Al, M. F. Graswinckel, J. M. Palomares, F. J. J. Peeters, S. Ponduri, T. Minea, W. A. Bongers, M. C. M. van de Sanden, and G. J. van Rooij, "Homogeneous co2 conversion by microwave plasma: Wave propagation and diagnostics", *Plasma Processes and Polymers*, vol. 14, no. 6, p. 1 600 120, DOI: https://doi.org/10.1002/ppap.201600120.

[32] Q. Wang, B.-H. Yan, Y. Jin, and Y. Cheng, "Dry reforming of methane in a dielectric barrier discharge reactor with ni/al2o3 catalyst: Interaction of catalyst and plasma", *Energy & Fuels*, vol. 23, no. 8, pp. 4196–4201, 2009. DOI: 10.1021/ef900286j.

[33] R. Snoeckx, Y. Zeng, X. Tu, and A. Bogaerts, "Plasma-based dry reforming: Improving the conversion and energy efficiency in a dielectric barrier discharge", *RSC Adv.*, vol. 5, Mar. 2015. DOI: 10.1039/C5RA01100K.

[34] V. Shapoval and E. Marotta, "Investigation on plasma-driven methane dry reforming in a self-triggered spark reactor", *Plasma Processes and Polymers*, vol. 12, no. 8, pp. 808–816, 2015. DOI: https://doi.org/10.1002/ppap.201400177.

[35] C. Montesano, M. Faedda, L. M. Martini, G. Dilecce, and P. Tosi, "Ch4 reforming with co2 in a nanosecond pulsed discharge. the importance of the pulse sequence", *Journal of CO2 Utilization*, vol. 49, p. 101 556, 2021, ISSN: 2212-9820. DOI: https://doi.org/10.1016/j.jcou.2021.101556.

[36] D. Li, X. Li, M. Bai, X. Tao, S. Shang, X. Dai, and Y. Yin, "Co2 reforming of ch4 by atmospheric pressure glow discharge plasma: A high conversion ability", *International Journal of Hydrogen Energy*, vol. 34, no. 1, pp. 308–313, 2009, ISSN: 0360-3199. DOI: https://doi.org/10.1016/j.ijhydene.2008.10.053.

[37] A. J. Wolf, T. W. H. Righart, F. J. J. Peeters, W. A. Bongers, and M. C. M. van de Sanden, "Implications of thermo-chemical instability on the contracted modes in CO2 microwave plasmas", vol. 29, no. 2, p. 025 005, Feb. 2020. DOI: 10.1088/1361-6595/ab5eca.

[38] P. W. C. Groen, A. J. Wolf, T. W. H. Righart, M. C. M. van de Sanden, F. J. J. Peeters, and W. A. Bongers, "Numerical model for the determination of the reduced electric field in a CO2 microwave plasma derived by the principle of impedance matching", vol. 28, no. 7, p. 075 016, Jul. 2019. DOI: 10.1088/1361-6595/ab1ca1.

[39] U. Fantz, "Basics of plasma spectroscopy", vol. 15, no. 4, S137–S147, Oct. 2006. DOI: 10.1088/0963-0252/15/4/s01.

[40] P. J. Bruggeman, N. Sadeghi, D. C. Schram, and V. Linss, "Gas temperature determination from rotational lines in non-equilibrium plasmas: A review", vol. 23, no. 2, p. 023 001, Apr. 2014. DOI: 10.1088/0963-0252/23/2/023001.

[41] T. Silva, N. Britun, T. Godfroid, and R. Snyders, "Simple method for gas temperature determination in co2-containing discharges", *Opt. Lett.*, vol. 39, no. 21, pp. 6146–6149, Nov. 2014. DOI: 10.1364/OL.39.006146.

[42] Y. Du, K. Tamura, S. Moore, P. Zhimin, T. Nozaki, and P. Bruggeman, "Co angstrom system for gas temperature measurements in co2 containing plasmas", *Plasma Chemistry and Plasma Processing*, vol. 37, Jan. 2017. DOI: 10.1007/s11090-016-9759-5.

[43] G. Herzberg, "Molecular spectra and molecular structure. i. spectra of diatomic molecules", *American Journal of Physics*, vol. 19, no. 6, pp. 390–391, 1951. DOI: 10.1119/1.1932852.

[44] H. F. C. L. Rodrigues, "Activation of carbon dioxide and methane by non-equilibrium plasmas", *IST - Instituto Superior Técnico*, Nov. 2018. [Online]. Available: https://fenix.tecnico.ulisboa.pt/cursos/meft/dissertacao/1972678479054453.

[45] A. S. Morillo Candás, "Investigation of fundamental mechanisms of co2 plasmas", *PhD thesis, Laboratoire de Physique des Plasmas (LPP)*, Dec. 2019.

[46] M. Slack and A. Grillo, "High temperature rate coefficient measurements of co + o chemiluminescence", *Combustion and Flame*, vol. 59, no. 2, pp. 189–196, 1985, ISSN: 0010-2180. DOI: https://doi.org/10.1016/0010-2180(85)90024-0.

[47] V. Guerra, M. Pinheiro, B. Gordiets, J. Loureiro, and C. Ferreira, "Calculated data on electron transport and excitation rate coefficients in n-2-o-2 and n-2-h-2 discharges", *Plasma Sources Science and Technology*, vol. 6, p. 220, Jan. 1999. DOI: 10.1088/0963-0252/6/2/016.

[48] A. Tejero-del-Caz, V. Guerra, D. Gonçalves, M. L. da Silva, L. Marques, N. Pinhão, C. D. Pintassilgo, and L. L. Alves, "The LisbOn KInetics boltzmann solver", *Plasma Sources Science and Technology*, vol. 28, no. 4, p. 043 001, Apr. 2019. DOI: 10.1088/1361-6595/ab0537.

[49] A. F. Silva, A. S. Morillo-Candás, A. Tejero-del-Caz, L. L. Alves, O. Guaitella, and V. Guerra, "A reaction mechanism for vibrationally-cold low-pressure CO2 plasmas", vol. 29, no. 12, p. 125 020, Dec. 2020. DOI: 10.1088/1361-6595/abc818.

[50] P. J. Chantry, "A simple formula for diffusion calculations involving wall reflection and low density", *Journal of Applied Physics*, vol. 62, no. 4, pp. 1141–1148, 1987. DOI: 10.1063/1.339662.

[51] K. Kutasi, V. Guerra, and P. Sá, "Theoretical insight into ar–o2surface-wave microwave discharges", *Journal of Physics D: Applied Physics*, vol. 43, no. 17, p. 175 201, Apr. 2010. DOI: 10.1088/0022-3727/43/17/175201.

[52] "Molecular theory of gases and liquids. j. o. hirschfelder, c. f. curtiss, and r. b. bird. wiley, new york, 1954. xxvi + 1219 pp., $20.00.", *Journal of Polymer Science*, vol. 17, no. 83, pp. 116–116, 1955. DOI: https://doi.org/10.1002/pol.1955.120178311.

[53] L. Alves, “The ist-lisbon database on lxcat”, *Journal of Physics: Conference Series*, vol. 565, p. 012 007, Dec. 2014. DOI: 10.1088/1742-6596/565/1/012007.

[54] J. Dutton, “The ist-lisbon database on lxcat”, *J. Phys. Chem. Ref. Data,*, vol. 4, p. 577, 1975.

[55] M. (Research and Software), [Online]. Available: http://www.lxcat.net/Morgan.

[56] R. J. et al, “Cross sections and rate coefficients for electron-impact ionization of hydrocarbon”, 2001.

[57] R. K. Janev and D. Reiter, “Collision processes of chy and chy+ hydrocarbons with plasma electrons and protons”, *Physics of Plasmas*, vol. 9, no. 9, pp. 4071–4081, 2002. DOI: 10.1063/1.1500735.

[58] R. Janev and D. Reiter, “Collision processes of hydrocarbon species in hydrogen plasmas. part 2. the ethane and propane families”, *ChemInform*, vol. 34, Sep. 2003. DOI: 10.1002/chin.200337260.

[59] J. R.K. and R. Detlev, “Collision processes of c2, 3hy and c2, 3hy+ hydrocarbons with electrons and protons”, *Physics of Plasmas*, vol. 11, pp. 780–829, Feb. 2004. DOI: 10.1063/1.1630794.

[60] I. J. Wysong, “Measurement of quenching rates of co(a3,v=0) using laser pump-and-probe technique”, *Chemical Physics Letters*, vol. 329, no. 1, pp. 42–46, 2000, ISSN: 0009-2614. DOI: https://doi.org/10.1016/S0009-2614(00)00967-2.

[61] M. P. Skrzypkowski, T. Gougousi, R. Johnsen, and M. F. Golde, “Measurement of the absolute yield of co(a3)+o products in the dissociative recombination of co2+ ions with electrons”, *The Journal of Chemical Physics*, vol. 108, no. 20, pp. 8400–8407, 1998. DOI: 10.1063/1.476267.

[62] W. Felder, W. Morrow, and R. Young, “Co(a3): Rate coefficients for quenching by o(3p)”, *Chemical Physics Letters*, vol. 15, no. 1, pp. 100–103, 1972, ISSN: 0009-2614. DOI: https://doi.org/10.1016/0009-2614(72)87026-X.

[63] P. Koelman, S. Heijkers, S. Tadayon Mousavi, W. Graef, D. Mihailova, T. Kozak, A. Bogaerts, and J. van Dijk, “A comprehensive chemical model for the splitting of co2 in non-equilibrium plasmas”, *Plasma Processes and Polymers*, vol. 14, no. 4-5, p. 1 600 155, 2017. DOI: https://doi.org/10.1002/ppap.201600155.

[64] L. Alves, P. Coche, M. Ridenti, and V. Guerra, “Electron scattering cross sections for the modelling of oxygen-containing plasmas”, *The European Physical Journal D*, vol. 70, Jun. 2016. DOI: 10.1140/epjd/e2016-70102-1.

[65] N. I. o. S. . and Technology, “Nist chemical kinetics database”, [Online]. Available: https://kinetics.nist.gov/kinetics/index.jsp.

[66] A. Cenian, A. Chernukho, V. Borodin, and G. Śliwiński, “Modeling of plasma-chemical reactions in gas mixture of co2 lasers i. gas decomposition in pure co2 glow discharge”, *Contributions to Plasma Physics*, vol. 34, no. 1, pp. 25–37, DOI: https://doi.org/10.1002/ctpp.2150340105.

Appendix A

List of Reactions 1

In this appendix, the reactions for the kinetic model used to simulate CO_2-CH_4, as well as the correspondent rate coefficient expression and reference are presented. The table structure is the following: the first column displays the numbering based on the process type, the seconds column shows the chemical equation, the third column displays the rate coefficient expression of the reaction (where f (σ) means that it was calculated through cross sections obtained from the EEDF) and the fourth column indicates the reference from which the reaction rate was obtained.

Number	Reaction	Rate	Reference
EN1	$e + CO_2 \longrightarrow e + e + CO_2(^+, X)$	f(σ)	[53]
EN2	$e + CO_2 \longrightarrow e + CO + O(1\,D)$	f(σ)	[53]
EN3	$e + CO_2 \longrightarrow e + CO(a_3P) + O(3\,P)$	f(σ)	[53]
EN4	$e + CO_2 \longrightarrow CO + O(-, gnd)$	f(σ)	[53]
EN5	$e + CO \longrightarrow C + O(-, gnd)$	f(σ)	[53]
EN6	$e + CO \longleftrightarrow e + CO(a_3P)$	f(σ)	[53]
EN7	$e + CO \longrightarrow e + C + O(3\,P)$	f(σ)	[53]
EN8	$e + CO \longrightarrow e + e + CO(^+, X)$	f(σ)	[53]
EN9	$e + O_2 \longleftrightarrow e + O_2(a_1Dg)$	f(σ)	[53]
EN10	$e + O_2 \longleftrightarrow e + O_2(b_1Sg^+)$	f(σ)	[53]
EN11	$e + O_2(a_1Dg) \longleftrightarrow e + O_2(b_1Sg^+)$	f(σ)	[53]
EN12	$e + O(3\,P) \longleftrightarrow e + O(1\,D)$	f(σ)	[53]
EN13	$e + O_2 \longrightarrow e + 2\,O(3\,P)$	f(σ)	[53]
EN14	$e + O_2 \longrightarrow e + O(3\,P) + O(1\,D)$	f(σ)	[53]
EN15	$e + O_2(a_1Dg) \longrightarrow e + 2\,O(3\,P)$	f(σ)	[53]
EN16	$e + O_2(a_1Dg) \longrightarrow e + O(3\,P) + O(1\,D)$	f(σ)	[53]
EN17	$e + O_3 \longrightarrow e + O(3\,P) + O_2$	f(σ)	[53]
EN18	$e + O_2 \longrightarrow 2\,e + O_2(^+, X)$	f(σ)	[53]
EN19	$e + O_2(a_1Dg) \longrightarrow 2\,e + O_2(^+, X)$	f(σ)	[53]
EN20	$e + O(3\,P) \longrightarrow 2\,e + O(^+, gnd)$	f(σ)	[53]
EN21	$e + O_2 \longrightarrow 2\,e + O(3\,P) + O(^+, gnd)$	f(σ)	[53]

EN22	$e + O_2(a_1Dg) \longrightarrow 2\,e + O(3\,P) + O(^+, gnd)$	f(σ)	[53]
EN23	$e + O_2 \longrightarrow O(-, gnd) + O(3\,P)$	f(σ)	[53]
EN24	$e + O_2(a_1Dg) \longrightarrow O(-, gnd) + O(3\,P)$	f(σ)	[53]
EN25	$e + C_2 \longrightarrow e + 2\,C$	f(σ)	[55]
EN26	$e + CH_4 \longrightarrow e + CH_3 + H(1\,s)$	f(σ)	[53]
EN27	$e + CH_4 \longrightarrow e + CH_2 + H_2$	f(σ)	[53]
EN28	$e + CH_4 \longrightarrow e + CH + H_2 + H(1\,s)$	f(σ)	[56],[57],[58], [59]
EN29	$e + CH_4 \longrightarrow e + C + 2\,H_2$	f(σ)	[56]-[59]
EN30	$e + CH_3 \longrightarrow e + CH_2 + H(1\,s)$	f(σ)	[56]-[59]
EN31	$e + CH_3 \longrightarrow e + CH + 2\,H(1\,s)$	f(σ)	[56]-[59]
EN32	$e + CH_2 \longrightarrow e + CH + H(1\,s)$	f(σ)	[53]
EN33	$e + CH_2 \longrightarrow e + C + H_2$	f(σ)	[53]
EN34	$e + CH \longrightarrow e + C + H(1\,s)$	f(σ)	[56]-[59]
EN35	$e + C_2H \longrightarrow e + C_2 + H(1\,s)$	f(σ)	[56]-[59]
EN36	$e + C_2H \longrightarrow e + C + CH$	f(σ)	[56]-[59]
EN37	$e + C_2H_2 \longrightarrow e + C_2H + H(1\,s)$	f(σ)	[56]-[59]
EN38	$e + C_2H_2 \longrightarrow e + C_2 + H_2$	f(σ)	[56]-[59]
EN39	$e + C_2H_2 \longrightarrow e + C_2 + 2\,H(1\,s)$	f(σ)	[56]-[59]
EN40	$e + C_2H_2 \longrightarrow e + 2\,CH$	f(σ)	[56]-[59]
EN41	$e+ C_2H_2 \longrightarrow e+ C_2H+ H(1\,s)$	f(σ)	[56]-[59]
EN42	$e+ C_2H_2 \longrightarrow e+ C_2+ H_2$	f(σ)	[56]-[59]
EN43	$e+ C_2H_2 \longrightarrow e+ C_2+ 2\,H(1\,s)$	f(σ)	[56]-[59]
EN44	$e+ C_2H_2 \longrightarrow e+ 2\,CH$	f(σ)	[56]-[59]
EN45	$e+ C_2H_2 \longrightarrow e+ CH_2+ C$	f(σ)	[56]-[59]
EN46	$e+ C_2H_3 \longrightarrow e+ C_2H_2+ H(1\,s)$	f(σ)	[56]-[59]
EN47	$e+ C_2H_3 \longrightarrow e+ C_2H+ H_2$	f(σ)	[56]-[59]
EN48	$e+ C_2H_4 \longrightarrow e+ C_2H_3+ H(1\,s)$	f(σ)	[56]-[59]
EN49	$e+ C_2H_4 \longrightarrow e+ C_2H_2+ H_2$	f(σ)	[56]-[59]
EN50	$e+ C_2H_4 \longrightarrow e+ C_2H_2+ 2\,H(1\,s)$	f(σ)	[56]-[59]
EN51	$e+ C_2H_4 \longrightarrow e+ C_2H+ H_2+ H(1\,s)$	f(σ)	[56]-[59]
EN52	$e+ C_2H_4 \longrightarrow e+ CH_3+ CH$	f(σ)	[56]-[59]
EN53	$e+ C_2H_4 \longrightarrow e+ 2\,CH_2$	f(σ)	[56]-[59]
EN54	$e+ C_2H_4 \longrightarrow e+ C+ CH_4$	f(σ)	[56]-[59]
EN55	$e+ C_2H_5 \longrightarrow e+ C_2H_4+ H(1\,s)$	f(σ)	[56]-[59]
EN56	$e+ C_2H_5 \longrightarrow e+ C_2H_3+ H_2$	f(σ)	[56]-[59]
EN57	$e+ C_2H_6 \longrightarrow e+ C_2H_5+ H(1\,s)$	f(σ)	[56]-[59]
EN58	$e+ C_2H_6 \longrightarrow e+ C_2H_4+ H_2$	f(σ)	[56]-[59]
EN59	$e+ H_2 \longrightarrow e+ H(1\,s)+ H(1\,s)$	f(σ)	[53]
EN60	$e+ H_2O \longrightarrow e+ H_2+ O(3\,P)$	f(σ)	-

EN61	e+ $H_2O \longrightarrow$ e+ H(1 s)+ OH	f(σ)	-

Table A.1: Electron-Neutral impact reactions.

Number	Reaction	Rate	Reference
NN1	$CO(a_3P) + O_2 \longrightarrow CO + 2\,O(3\,P)$	2.40e-17	[60]
NN2	$CO(a_3P) + O_2 \longrightarrow CO_2 + O(3\,P)$	1.20e-17	[60]
NN3	$CO(a_3P) + CO \longrightarrow CO_2 + C$	9.12e-19	[60]
NN4	$CO(a_3P) + CO \longrightarrow 2\,CO$	5.61e-17	[60]
NN5	$CO(a_3P) + CO_2 \longrightarrow CO + CO_2$	5.00e-18	[61]
NN6	$CO(a_3P) + CO_2 \longrightarrow 2\,CO + O(3\,P)$	5.00e-18	[61]
NN7	$CO(a_3P) + O(3\,P) \longrightarrow CO + O(3\,P)$	1.90e-16	[62]
NN8	$O(3\,P) + CO + CO_2 \longrightarrow CO_2 + CO_2$	1.64e-45exp($\frac{-1510.0}{T_g}$)	[63]
NN9	$O(3\,P) + CO + CO \longrightarrow CO_2 + CO$	8.20e-46exp($\frac{-1510.0}{T_g}$)	[63]
NN10	$O(3\,P) + CO + O_2 \longrightarrow CO_2 + O_2$	8.20e-46exp($\frac{-1510.0}{T_g}$)	[63]
NN11	$O_2 + C \longrightarrow CO + O(3\,P)$	3.00e-17	[63]
NN12	$O_2(a_1Dg) + O(3\,P) \longrightarrow O_2 + O(3\,P)$	7.00e-23	[64]
NN13	$O(3\,P) + O(1\,D) \longrightarrow O(3\,P) + O(3\,P)$	8.00e-18	[64]
NN14	$O(1\,D) + O_2 \longrightarrow O(3\,P) + O_2(a_1Dg)$	1.00e-18	[64]
NN15	$O(1\,D) + O_3 \longrightarrow 2\,O_2$	1.20e-16	[64]
NN16	$O(1\,D) + O_3 \longrightarrow O_2 + 2\,O(3\,P)$	1.20e-16	[64]
NN17	$O_3(exc) + O(3\,P) \longrightarrow O_3 + O(3\,P)$	2.00e-19	[64]
NN18	$O_3(exc) + O_2 \longrightarrow O_3 + O_2$	3.00e-21	[64]
NN19	$2\,O(3\,P) + O_2 \longrightarrow O_3 + O(3\,P)$	2.10e-46exp($\frac{345.0}{T_g}$)	[64]
NN20	$O_2(a_1Dg) + O_3 \longrightarrow 2\,O_2 + O(3\,P)$	5.20e-17exp($\frac{-2840.0}{T_g}$)	[64]
NN21	$O(3\,P) + O_3 \longrightarrow 2\,O_2$	9.00e-18exp($\frac{-2300.0}{T_g}$)	[64]
NN22	$O(3\,P) + O_3 \longrightarrow O_2(a_1Dg) + O_2$	5.94e-18exp($\frac{-2300.0}{T_g}$)	[64]
NN23	$O(3\,P) + O_3 \longrightarrow O_2(b_1Sg^+) + O_2$	3.06e-18exp($\frac{-2300.0}{T_g}$)	[64]
NN24	$O(1\,D) + O_2 \longrightarrow O(3\,P) + O_2(b_1Sg^+)$	2.56e-17exp($\frac{67.0}{T_g}$)	[64]
NN25	$O_2(a_1Dg) + O_3(exc) \longrightarrow 2\,O_2 + O(3\,P)$	2.60e-16exp($\frac{-1287.0}{T_g}$)	[64]
NN26	$O(3\,P) + O_3(exc) \longrightarrow 2\,O_2$	8.00e-18exp($\frac{-507.0}{T_g}$)	[64]
NN27	$O(3\,P) + O_2 + O_2 \longrightarrow O_3 + O_2$	2.11e-47exp($\frac{663.0}{T_g}$)	[64]
NN28	$O(3\,P) + O_2 + O_2 \longrightarrow O_3(exc) + O_2$	4.29e-47exp($\frac{663.0}{T_g}$)	[64]
NN29	$O(1\,D) + O_2 \longrightarrow O(3\,P) + O_2$	7.00e-18exp($\frac{67.0}{T_g}$)	[64]
NN30	$2\,O_2(a_1Dg) \longrightarrow O_2(b_1Sg^+) + O_2$	6.99e-34$Tg^{3.8}$exp($\frac{7.00e+02}{T_g}$)	[64]
NN31	$2\,O(3\,P) + O_2 \longrightarrow O_2 + O_2$	1.90e-42$Tg^{-1.0}$exp($\frac{-1.70e+02}{T_g}$)	[64]
NN32	$2\,O(3\,P) + O_2 \longrightarrow O_2 + O_2(a_1Dg)$	1.26e-42$Tg^{-1.0}$exp($\frac{-1.70e+02}{T_g}$)	[64]
NN33	$2\,O(3\,P) + O_2 \longrightarrow O_2 + O_2(b_1Sg^+)$	6.48e-43$Tg^{-1.0}$exp($\frac{-1.70e+02}{T_g}$)	[64]

NN34	$O(3P) + O_2 + O_3 \longrightarrow 2\,O_3$	1.66e-46exp($\frac{300.0}{T_g}$)	[64]
NN35	$3\,O(3P) \longrightarrow O_2 + O(3P)$	3.60e-44$Tg^{-0.63}$	[64]
NN36	$O_2(a_1Dg) + O_2 \longrightarrow O_2 + O_2$	2.29e-26$Tg^{0.8}$	[64]
NN37	$CH_4 + CO_2 \longrightarrow CH_3 + H(1s) + CO_2$	2.92e+17$\cdot T_g^{-8.0}$ exp($\frac{-6.11e+04}{T_g}$)	[65]
NN38	$CH_4 + CO \longrightarrow CH_3 + H(1s) + CO$	2.92e+17$\cdot T_g^{-8.0}$ exp($\frac{-6.11e+04}{T_g}$)	[65]
NN39	$CH_4 + O_2 \longrightarrow CH_3 + H(1s) + O_2$	2.92e+17$\cdot T_g^{-8.0}$ exp($\frac{-6.11e+04}{T_g}$)	[65]
NN40	$CH_4 + CH_4 \longrightarrow CH_3 + H(1s) + CH_4$	2.92e+17$\cdot T_g^{-8.0}$ exp($\frac{-6.11e+04}{T_g}$)	[65]
NN41	$CH_4 + H(1s) \longrightarrow CH_3 + H_2$	3.65e-26$\cdot T_g^{3.0}$ exp($\frac{-4.41e+03}{T_g}$)	[65]
NN42	$CH_3 + H_2 \longrightarrow CH_4 + H(1s)$	4.71e-28$\cdot T_g^{3.12}$ exp($\frac{-4.38e+03}{T_g}$)	[65]
NN43	$CH_4 + CH_2 \longrightarrow CH_3 + CH_3$	7.14e-18 exp($\frac{-5.05e+03}{T_g}$)	[65]
NN44	$CH_3 + CH_3 \longrightarrow CH_4 + CH_2$	7.14e-18 exp($\frac{-5.05e+03}{T_g}$)	[65]
NN45	$CH_4 \longrightarrow CH_3 + H(1s)$	1.40e-12 exp($\frac{-4.57e+04}{T_g}$)	[65]
NN46	$CH_3 + H(1s) \longrightarrow CH_4$	2.02e-15$\cdot T_g^{-0.4}$	[65]
NN47	$CH_4 + O(3P) \longrightarrow CH_3 + OH$	8.02e-24$\cdot T_g^{2.2}$ exp($\frac{-3.82e+03}{T_g}$)	[65]
NN48	$CH_4 + O(1D) \longrightarrow CH_3 + OH$	1.35e-16	[65]
NN49	$CH_3 + OH \longrightarrow CH_4 + O(3P)$	1.14e-25$\cdot T_g^{2.2}$ exp($\frac{-2.24e+03}{T_g}$)	[65]
NN50	$CH_4 + OH \longrightarrow CH_3 + H_2O$	4.01e-27$\cdot T_g^{3.04}$ exp($\frac{-9.20e+02}{T_g}$)	[65]
NN51	$CH_3 + H_2O \longrightarrow CH_4 + OH$	7.86e-28$\cdot T_g^{2.9}$ exp($\frac{-7.48e+03}{T_g}$)	[65]
NN52	$CH_3 + CH_2O \longrightarrow CH_4 + HCO$	9.56e-27$\cdot T_g^{2.8}$ exp($\frac{-2.95e+03}{T_g}$)	[65]
NN53	$CH_4 + HCO \longrightarrow CH_3 + CH_2O$	1.19e-26$\cdot T_g^{2.85}$ exp($\frac{-1.13e+04}{T_g}$)	[65]
NN54	$CH_3 + H(1s) \longrightarrow CH_2 + H_2$	1.96e-24$\cdot T_g^{2.43}$ exp($\frac{-6.01e+03}{T_g}$)	[65]
NN55	$CH_2 + H_2 \longrightarrow CH_3 + H(1s)$	7.21e-25$\cdot T_g^{2.3}$ exp($\frac{-3.70e+03}{T_g}$)	[65]
NN56	$CH_3 \longrightarrow CH_2 + H(1s)$	1.69e-14 exp($\frac{-4.56e+04}{T_g}$)	[65]
NN57	$CH_2 + O(3P) \longrightarrow CO + H_2$	6.64e-17	[65]
NN58	$CH_2 + O(3P) \longrightarrow CO + H(1s) + H(1s)$	1.33e-16	[65]
NN59	$CH_2 + H(1s) \longrightarrow CH + H_2$	1.00e-17 exp($\frac{9.00e+02}{T_g}$)	[65]
NN60	$CH + H_2 \longrightarrow CH_2 + H(1s)$	5.45e-22$\cdot T_g^{1.79}$ exp($\frac{-8.39e+02}{T_g}$)	[65]
NN61	$CH_2 + O_2 \longrightarrow CO_2 + H_2$	4.47e-09$\cdot T_g^{-3.3}$ exp($\frac{-1.44e+03}{T_g}$)	[65]
NN62	$CH_2 + O_2 \longrightarrow CO_2 + H(1s) + H(1s)$	3.53e-21$\cdot T_g^{0.99}$ exp($\frac{1.36e+02}{T_g}$)	[65]
NN63	$CH_2 + O_2 \longrightarrow CO + H_2O$	4.00e-19	[65]
NN64	$CH_2 \longrightarrow C + H_2$	2.66e-16 exp($\frac{-3.22e+04}{T_g}$)	[65]
NN65	$C + H_2 \longrightarrow CH_2$	2.06e-17 exp($\frac{-5.65e+01}{T_g}$)	[65]
NN66	$CH_2 \longrightarrow CH + H(1s)$	9.33e-15 exp($\frac{-4.51e+04}{T_g}$)	[65]
NN67	$CH_2 + CO_2 \longrightarrow CH_2O + CO$	3.90e-20	[65]
NN68	$CH_2 + OH \longrightarrow H(1s) + CH_2O$	3.01e-17	[65]
NN69	$CH_2 + O(3P) \longrightarrow HCO + H(1s)$	5.01e-17	[65]
NN70	$HCO + H(1s) \longrightarrow O(3P) + CH_2$	6.61e-17 exp($\frac{-5.16e+04}{T_g}$)	[65]
NN71	$H_2 + OH \longrightarrow H_2O + H(1s)$	1.69e-22$\cdot T_g^{1.6}$ exp($\frac{-1.66e+03}{T_g}$)	[65]
NN72	$H_2O + H(1s) \longrightarrow H_2 + OH$	7.42e-22$\cdot T_g^{1.6}$ exp($\frac{-9.72e+03}{T_g}$)	[65]

NN73	$H_2O \longrightarrow$ OH + H(1 s)	6.56e-16 exp($\frac{-5.36e+04}{T_g}$)	[65]
NN74	OH + H(1 s) $\longrightarrow H_2O$	2.69e-16 exp($\frac{-7.46e+01}{T_g}$)	[65]
NN75	H_2 + HCO $\longrightarrow CH_2O$ + H(1 s)	2.96e-24$\cdot T_g^{2.0}$ exp($\frac{-8.97e+03}{T_g}$)	[65]
NN76	CH_2O + H(1 s) $\longrightarrow H_2$ + HCO	2.08e-22$\cdot T_g^{1.62}$ exp($\frac{-1.09e+03}{T_g}$)	[65]
NN77	H(1 s) + $CO_2 \longrightarrow$ CO + OH	2.51e-16 exp($\frac{-1.34e+04}{T_g}$)	[65]
NN78	CO + OH $\longrightarrow$ H(1 s) + CO_2	7.22e-24$\cdot T_g^{1.5}$ exp($\frac{3.73e+02}{T_g}$)	[65]
NN79	H(1 s) + HCO $\longrightarrow$ CO + H_2	1.83e-16	[65]
NN80	H_2O + O(3 P) $\longrightarrow$ OH + OH	8.16e-20$\cdot T_g^{0.95}$ exp($\frac{-8.57e+03}{T_g}$)	[65]
NN81	OH + OH $\longrightarrow H_2O$ + O(3 P)	2.47e-21$\cdot T_g^{1.14}$ exp($\frac{-5.05e+01}{T_g}$)	[65]
NN82	O(3 P) + HCO $\longrightarrow$ H(1 s) + CO_2	4.98e-17	[65]
NN83	O(3 P) + HCO $\longrightarrow$ CO + OH	4.98e-17	[65]
NN84	OH + HCO $\longrightarrow$ CO + H_2O	8.30e-17	[65]
NN85	H_2 + $O_2 \longrightarrow$ OH + OH	3.37e-18$\cdot T_g^{0.44}$ exp($\frac{-3.48e+04}{T_g}$)	[65]
NN86	OH + OH $\longrightarrow$ H_2 + O_2	1.81e-19$\cdot T_g^{0.51}$ exp($\frac{-2.54e+04}{T_g}$)	[65]
NN87	CH + $O_2 \longrightarrow$ HCO + O(3 P)	1.66e-17	[65]
NN88	CH + $O_2 \longrightarrow$ CO + OH	8.30e-17	[65]
NN89	CO + H(1 s) $\longrightarrow$ HCO	5.29e-46 exp($\frac{-3.70e+02}{T_g}$)	[65]
NN90	HCO$\longrightarrow$ CO + H(1 s)	8.60e-09$\cdot T_g^{-2.14}$ exp($\frac{-1.04e+04}{T_g}$)	[65]
NN91	$H_2 \longrightarrow$ H(1 s) + H(1 s)	7.67e-11$\cdot T_g^{-1.4}$ exp($\frac{-5.26e+04}{T_g}$)	[65]
NN92	H(1 s) + H(1 s) $\longrightarrow$ H_2	1.81e-19 exp($\frac{-7.54e+02}{T_g}$)	[65]
NN93	CH + O(3 P) $\longrightarrow$ CO + H(1 s)	6.59e-17	[65]
NN94	CO + $H_2 \longrightarrow$ CO_2 + H(1 s)	1.01e-13$\cdot T_g^{-0.84}$ exp($\frac{-2.49e+04}{T_g}$)	[65]
NN95	H_2O + O(3 P) $\longrightarrow$ H_2 + O_2	1.77e-20$\cdot T_g^{0.97}$ exp($\frac{-3.45e+04}{T_g}$)	[65]
NN96	H_2 + $O_2 \longrightarrow H_2O$ + O(3 P)	2.26e-18$\cdot T_g^{0.51}$ exp($\frac{-3.55e+04}{T_g}$)	[65]
NN97	CH + H(1 s) $\longrightarrow$ C + H_2	6.14e-16$\cdot T_g^{0.01}$ exp($\frac{-2.69e+03}{T_g}$)	[65]
NN98	C + $H_2 \longrightarrow$ CH + H(1 s)	6.64e-16 exp($\frac{-1.17e+04}{T_g}$)	[65]
NN99	H_2 + O(3 P) $\longrightarrow$ H(1 s) + OH	8.37e-26$\cdot T_g^{2.67}$ exp($\frac{-3.16e+03}{T_g}$)	[65]
NN100	H(1 s) + OH $\longrightarrow$ H_2 + O(3 P)	7.95e-27$\cdot T_g^{2.8}$ exp($\frac{-1.95e+03}{T_g}$)	[65]
NN101	CH + $CO_2 \longrightarrow$ H(1 s) + CO + CO	5.71e-18 exp($\frac{-3.45e+02}{T_g}$)	[65]
NN102	H(1 s) + O(3 P) $\longrightarrow$ OH	1.31e-43$\cdot T_g^{-1.0}$	[65]
NN103	OH$\longrightarrow$ H(1 s) + O(3 P)	4.00e-15 exp($\frac{-5.00e+04}{T_g}$)	[65]
NN104	H(1 s) + $O_2 \longrightarrow$ OH + O(3 P)	1.62e-16 exp($\frac{-7.47e+03}{T_g}$)	[65]
NN105	OH + O(3 P) $\longrightarrow$ H(1 s) + O_2	1.12e-16$\cdot T_g^{-0.32}$ exp($\frac{1.77e+02}{T_g}$)	[65]
NN106	CH + $H_2 \longrightarrow CH_3$	1.03e-18	[65]
NN107	CH_2 + $CH_2O \longrightarrow CH_3$ + HCO	1.00e-20	[65]
NN108	CH_2 + $H_2O \longrightarrow CH_3$ + OH	1.60e-20	[65]
NN109	CH_2 + HCO $\longrightarrow CH_3$ + CO	3.01e-17	[65]
NN110	CH_2O + OH $\longrightarrow H_2O$ + HCO	5.65e-21$\cdot T_g^{1.18}$ exp($\frac{2.25e+02}{T_g}$)	[65]
NN111	$CH_3 \longrightarrow$ CH + H_2	1.15e-15 exp($\frac{-4.15e+04}{T_g}$)	[65]

NN112	CH_3 + HCO $\longrightarrow$ CH_4 + CO	2.01e-16	[65]
NN113	CH_3 + O(3 P) $\longrightarrow$ CH_2O + H(1 s)	1.14e-16	[65]
NN114	CH_3 + OH $\longrightarrow$ CH_2 + H_2O	1.20e-16 $\exp(\frac{-1.40e+03}{T_g})$	[65]
NN115	H_2O + HCO $\longrightarrow$ CH_2O + OH	3.87e-22$\cdot T_g^{1.35}$ $\exp(\frac{-1.31e+04}{T_g})$	[65]
NN116	HCO + HCO $\longrightarrow$ CH_2O + CO	5.00e-17	[65]
NN117	O(1 D) + CH_4 $\longrightarrow$ CH_2O + H_2	1.50e-17	[65]
NN118	O(1 D) + H_2O $\longrightarrow$ OH + OH	7.53e-21$\cdot T_g^{1.3}$ $\exp(\frac{-8.60e+03}{T_g})$	[65]
NN119	C_2 + H_2 $\longrightarrow$ C_2H + H(1 s)	1.10e-16 $\exp(\frac{-4.00e+03}{T_g})$	[65]
NN120	C_2H + C_2H $\longrightarrow$ C_2H_2 + C_2	3.01e-18	[65]
NN121	C_2H + C_2H_3 $\longrightarrow$ C_2H_2 + C_2H_2	1.60e-18	[65]
NN122	C_2H + C_2H_4 $\longrightarrow$ C_2H_3 + C_2H_2	1.00e-09	[65]
NN123	C_2H + C_2H_5 $\longrightarrow$ C_2H_2 + C_2H_4	3.01e-18	[65]
NN124	C_2H + C_2H_6 $\longrightarrow$ C_2H_2 + C_2H_5	5.99e-18	[65]
NN125	C_2H + CH_4 $\longrightarrow$ C_2H_2 + CH_3	3.02e-18	[65]
NN126	C_2H + H(1 s) $\longrightarrow$ C_2H_2	3.01e-16	[65]
NN127	C_2H + H_2 $\longrightarrow$ C_2H_2 + H(1 s)	3.21e-23$\cdot T_g^{2.32}$ $\exp(\frac{-1.09e+03}{T_g})$	[65]
NN128	C_2H + HCO $\longrightarrow$ C_2H_2 + CO	1.00e-16	[65]
NN129	C_2H + O(3 P) $\longrightarrow$ CH + CO	1.69e-17	[65]
NN130	C_2H + O_2 $\longrightarrow$ HCO + CO	4.00e-18	[65]
NN131	C_2H + OH $\longrightarrow$ CH_2 + CO	3.01e-17	[65]
NN132	C_2H + OH $\longrightarrow$ C_2H_2 + O(3 P)	3.01e-17	[65]
NN133	C_2H_2 $\longrightarrow$ C_2H + H(1 s)	6.64e-14 $\exp(\frac{-5.38e+04}{T_g})$	[65]
NN134	C_2H_2 + C_2H_2 $\longrightarrow$ C_2H_3 + C_2H	1.60e-17 $\exp(\frac{-4.25e+04}{T_g})$	[65]
NN135	C_2H_2 + C_2H_4 $\longrightarrow$ C_2H_3 + C_2H_3	4.00e-17 $\exp(\frac{-3.44e+04}{T_g})$	[65]
NN136	C_2H_2 + C_2H_5 $\longrightarrow$ C_2H + C_2H_6	4.50e-19 $\exp(\frac{-1.18e+04}{T_g})$	[65]
NN137	C_2H_2 + CH_3 $\longrightarrow$ CH_4 + C_2H	3.00e-19 $\exp(\frac{-8.70e+03}{T_g})$	[65]
NN138	C_2H_2 + H(1 s) $\longrightarrow$ H_2 + C_2H	1.00e-16 $\exp(\frac{-1.40e+04}{T_g})$	[65]
NN139	C_2H_2 + H(1 s) $\longrightarrow$ C_2H_3	1.40e-17 $\exp(\frac{-1.30e+03}{T_g})$	[65]
NN140	C_2H_2 + H_2 $\longrightarrow$ C_2H_4	5.00e-19 $\exp(\frac{-1.96e+04}{T_g})$	[65]
NN141	C_2H_2 + H_2 $\longrightarrow$ C_2H_3 + H(1 s)	4.00e-18 $\exp(\frac{-3.27e+04}{T_g})$	[65]
NN142	C_2H_2 + O(3 P) $\longrightarrow$ CH_2 + CO	6.72e-22$\cdot T_g^{1.5}$ $\exp(\frac{-8.50e+02}{T_g})$	[65]
NN143	C_2H_2 + OH $\longrightarrow$ C_2H + H_2O	5.56e-23$\cdot T_g^{2.0}$ $\exp(\frac{-7.04e+03}{T_g})$	[65]
NN144	C_2H_3 $\longrightarrow$ C_2H_2 + H(1 s)	4.89e-15 $\exp(\frac{-1.61e+04}{T_g})$	[65]
NN145	C_2H_3 + C_2H_3 $\longrightarrow$ C_2H_4 + C_2H_2	1.60e-18	[65]
NN146	C_2H_3 + C_2H_6 $\longrightarrow$ C_2H_4 + C_2H_5	1.00e-27$\cdot T_g^{3.3}$ $\exp(\frac{-5.28e+03}{T_g})$	[65]
NN147	C_2H_3 + CH_2O $\longrightarrow$ C_2H_4 + HCO	8.83e-27$\cdot T_g^{2.81}$ $\exp(\frac{-2.95e+03}{T_g})$	[65]
NN148	C_2H_3 + CH_3 $\longrightarrow$ C_2H_2 + CH_4	6.50e-19	[65]
NN149	C_2H_3 + CH_4 $\longrightarrow$ C_2H_4 + CH_3	2.40e-30$\cdot T_g^{4.02}$ $\exp(\frac{-2.75e+03}{T_g})$	[65]
NN150	C_2H_3 + H(1 s) $\longrightarrow$ C_2H_2 + H_2	2.00e-17	[65]

NN151	C_2H_3 + H(1 s) $\longrightarrow$ C_2H_4	2.01e-16	[65]
NN152	C_2H_3 + H_2 $\longrightarrow$ C_2H_4 + H(1 s)	5.00e-26$\cdot T_g^{2.63}$ exp($\frac{-4.30e+03}{T_g}$)	[65]
NN153	C_2H_3 + H_2O $\longrightarrow$ C_2H_4 + OH	7.86e-28$\cdot T_g^{2.9}$ exp($\frac{-7.48e+03}{T_g}$)	[65]
NN154	C_2H_3 + HCO $\longrightarrow$ C_2H_4 + CO	1.50e-16	[65]
NN155	C_2H_3 + O(3 P) $\longrightarrow$ C_2H_2 + OH	1.76e-18$\cdot T_g^{0.2}$ exp($\frac{2.15e+02}{T_g}$)	[65]
NN156	C_2H_3 + O(3 P) $\longrightarrow$ CO + CH_3	1.25e-17	[65]
NN157	C_2H_3 + O(3 P) $\longrightarrow$ HCO + CH_2	1.25e-17	[65]
NN158	C_2H_3 + O_2 $\longrightarrow$ CH_2O + HCO	9.00e-18	[65]
NN159	C_2H_3 + OH $\longrightarrow$ C_2H_2 + H_2O	5.00e-17	[65]
NN160	C_2H_4 $\longrightarrow$ C_2H_3 + H(1 s)	4.30e-13 exp($\frac{-4.86e+04}{T_g}$)	[65]
NN161	C_2H_4 $\longrightarrow$ C_2H_2 + H_2	5.80e-14 exp($\frac{-3.60e+04}{T_g}$)	[65]
NN162	C_2H_4 + C_2H_4 $\longrightarrow$ C_2H_3 + C_2H_5	8.00e-16 exp($\frac{-3.60e+04}{T_g}$)	[65]
NN163	C_2H_4 + C_2H_5 $\longrightarrow$ C_2H_6 + C_2H_3	1.05e-27$\cdot T_g^{3.13}$ exp($\frac{-9.06e+03}{T_g}$)	[65]
NN164	C_2H_4 + CH_3 $\longrightarrow$ C_2H_3 + CH_4	6.91e-18 exp($\frac{-5.48e+03}{T_g}$)	[65]
NN165	C_2H_4 + H(1 s) $\longrightarrow$ H_2 + C_2H_3	9.00e-16 exp($\frac{-7.50e+03}{T_g}$)	[65]
NN166	C_2H_4 + H(1 s) $\longrightarrow$ C_2H_5	6.53e-21$\cdot T_g^{1.28}$ exp($\frac{-6.49e+02}{T_g}$)	[65]
NN167	C_2H_4 + H_2 $\longrightarrow$ C_2H_5 + H(1 s)	1.70e-17 exp($\frac{-3.43e+04}{T_g}$)	[65]
NN168	C_2H_4 + O(3 P) $\longrightarrow$ CH_3 + HCO	2.17e-22$\cdot T_g^{1.55}$ exp($\frac{-2.15e+02}{T_g}$)	[65]
NN169	C_2H_4 + O_3 $\longrightarrow$ CH_2O + CO_2 + H_2	7.06e-25	[65]
NN170	C_2H_4 + O_3 $\longrightarrow$ CH_2O + CO + H_2O	7.06e-25	[65]
NN171	C_2H_4 + O_3 $\longrightarrow$ CH_2O + CH_2O + O(3 P)	2.69e-25	[65]
NN172	C_2H_4 + OH $\longrightarrow$ C_2H_3 + H_2O	2.56e-26$\cdot T_g^{2.75}$ exp($\frac{-2.10e+03}{T_g}$)	[65]
NN173	C_2H_5 $\longrightarrow$ C_2H_4 + H(1 s)	1.70e-12 exp($\frac{-1.68e+04}{T_g}$)	[65]
NN174	C_2H_5 + C_2H_5 $\longrightarrow$ C_2H_4 + C_2H_6	2.30e-18	[65]
NN175	C_2H_5 + CH_2O $\longrightarrow$ C_2H_6 + HCO	8.97e-27$\cdot T_g^{2.81}$ exp($\frac{-2.95e+03}{T_g}$)	[65]
NN176	C_2H_5 + CH_3 $\longrightarrow$ C_2H_4 + CH_4	1.91e-18	[65]
NN177	C_2H_5 + CH_4 $\longrightarrow$ C_2H_6 + CH_3	1.43e-31$\cdot T_g^{4.14}$ exp($\frac{-6.32e+03}{T_g}$)	[65]
NN178	C_2H_5 + H(1 s) $\longrightarrow$ C_2H_4 + H_2	3.01e-18	[65]
NN179	C_2H_5 + H(1 s) $\longrightarrow$ C_2H_6	6.00e-17	[65]
NN180	C_2H_5 + H(1 s) $\longrightarrow$ CH_3 + CH_3	6.00e-17	[65]
NN181	C_2H_5 + H_2 $\longrightarrow$ C_2H_6 + H(1 s)	5.10e-30$\cdot T_g^{3.6}$ exp($\frac{-4.25e+03}{T_g}$)	[65]
NN182	C_2H_5 + H_2O $\longrightarrow$ C_2H_6 + OH	5.58e-24$\cdot T_g^{1.44}$ exp($\frac{-1.02e+04}{T_g}$)	[65]
NN183	C_2H_5 + HCO $\longrightarrow$ C_2H_6 + CO	2.01e-16	[65]
NN184	C_2H_5 + O(3 P) $\longrightarrow$ CH_2O + CH_3	2.67e-17	[65]
NN185	C_2H_5 + O(3 P) $\longrightarrow$ C_2H_4 + OH	5.32e-18$\cdot T_g^{0.03}$ exp($\frac{1.98e+02}{T_g}$)	[65]
NN186	C_2H_5 + OH $\longrightarrow$ C_2H_6 + O(3 P)	1.57e-46$\cdot T_g^{8.8}$ exp($\frac{-2.50e+02}{T_g}$)	[65]
NN187	C_2H_5 + OH $\longrightarrow$ C_2H_4 + H_2O	4.00e-17	[65]
NN188	C_2H_6 $\longrightarrow$ CH_3 + CH_3	1.17e+19$\cdot T_g^{-8.24}$ exp($\frac{-4.71e+04}{T_g}$)	[65]
NN189	C_2H_6 + CH_2 $\longrightarrow$ C_2H_5 + CH_3	1.07e-17 exp($\frac{-3.98e+03}{T_g}$)	[65]

NN190	C_2H_6 + CH_3 $\longrightarrow$ C_2H_5 + CH_4	2.40e-37$\cdot T_g^{6.0}$ exp($\frac{-3.04e+03}{T_g}$)	[65]
NN191	C_2H_6 + H(1 s) $\longrightarrow$ C_2H_5 + H_2	2.40e-21$\cdot T_g^{1.5}$ exp($\frac{-3.73e+03}{T_g}$)	[65]
NN192	C_2H_6 + HCO $\longrightarrow$ C_2H_5 + CH_2O	7.65e-26$\cdot T_g^{2.72}$ exp($\frac{-9.18e+03}{T_g}$)	[65]
NN193	C_2H_6 + O(3 P) $\longrightarrow$ C_2H_5 + OH	1.64e-21$\cdot T_g^{1.5}$ exp($\frac{-2.92e+03}{T_g}$)	[65]
NN194	C_2H_6 + OH $\longrightarrow$ C_2H_5 + H_2O	1.18e-23$\cdot T_g^{2.0}$ exp($\frac{-4.35e+02}{T_g}$)	[65]
NN195	CH + C_2H_6 $\longrightarrow$ C_2H_4 + CH_3	1.30e-16	[65]
NN196	CH + CH $\longrightarrow$ C_2H_2	2.00e-16	[65]
NN197	CH_2 + CH $\longrightarrow$ C_2H_2 + H(1 s)	6.61e-17	[65]
NN198	CH_2 + CH_2 $\longrightarrow$ C_2H_2 + 2 H(1 s)	3.32e-16 exp($\frac{-5.53e+03}{T_g}$)	[65]
NN199	CH_2 + CH_2 $\longrightarrow$ C_2H_4	1.70e-18	[65]
NN200	CH_3 + CH $\longrightarrow$ C_2H_3 + H(1 s)	5.00e-17	[65]
NN201	CH_3 + CH_2 $\longrightarrow$ H(1 s) + C_2H_4	7.00e-17	[65]
NN202	CH_3 + CH_3 $\longrightarrow$ C_2H_6	5.47e-14$\cdot T_g^{-1.1}$ exp($\frac{-1.60e+02}{T_g}$)	[65]
NN203	CH_3 + CH_3 $\longrightarrow$ C_2H_4 + H_2	1.70e-14 exp($\frac{-1.61e+04}{T_g}$)	[65]

Table A.2: Neutral-Neutral reactions. The rate coefficient units are m^3/ s

Number	Reaction	Rate	Reference
EI1	e + $O_2(b_1Sg^+)$ $\longrightarrow$ e + 2 O(3 P)	f(σ)	[64]
EI2	e + $O_2(b_1Sg^+)$ $\longrightarrow$ e + O(3 P) + O(1 D)	f(σ)	[64]
EI3	e + O($-$, gnd) $\longrightarrow$ 2 e + O(3 P)	f(σ)	[64]
EI4	e + $CO_2(^+, X)$ $\longrightarrow$ CO + O(3 P)	$2.7 \cdot 10^{-14} T_e^{-0.75}$	[63]

Table A.3: Electron-Ion impact reactions. The rate coefficients units are m^3/s.

Number	Reaction
T1	$CO_2(^+, X)$ + wall $\longrightarrow CO_2$
T2	$CO(^+, X)$ + wall $\longrightarrow CO$
T3	$O_2(^+, X)$ + wall $\longrightarrow O_2$
T4	$O(^+, gnd)$ + wall $\longrightarrow O(3\,P)$
T5	$O_2(a_1Dg)$ + wall $\longrightarrow O_2$
T6	$O_2(b_1Sg^+)$ + wall $\longrightarrow O_2$
T7	$O(3\,P)$ + wall $\longrightarrow 0.5\,O_2$
T8	$O(1\,D)$ + wall $\longrightarrow O(3\,P)$
T9	$O_3(exc)$ + wall $\longrightarrow O_3$

Table A.4: Transport mechanisms. The neutral species undergo diffusion to the wall, while charged species suffer classical ambipolar diffusion.

Number	Reaction	Rate	Reference
NI1	$CO(^+, X) + O_2 \longrightarrow O_2(^+, X) + CO$	5e-16	[66]
NI2	$O(^+, gnd) + CO_2 \longrightarrow O_2(^+, X) + CO$	8.1e-16	[63]
NI3	$O(^+, gnd) + CO_2 \longrightarrow CO_2(^+, X) + O(3\,P)$	4.5e-16	[63]
NI4	$CO_2(^+, X) + O_2 \longrightarrow O_2(^+, X) + CO_2$	5.3e-17	[63]
NI5	$CO_2(^+, X) + O(3\,P) \longrightarrow O_2(^+, X) + CO$	1.64e-16	[63]
NI6	$CO_2(^+, X) + O(3\,P) \longrightarrow O(^+, gnd) + CO_2$	9.62e-17	[63]
NI7	$CO(^+, X) + CO_2 \longrightarrow CO_2(^+, X) + CO$	1e-15	[63]
NI8	$O(-, gnd) + CO \longrightarrow CO_2 + e$	5.8e-15$Tg^{-0.39}$	[63]
NI9	$O_2(b_1Sg^+) + O(3\,P) \longrightarrow O_2 + O(3\,P)$	4e-20	[64]
NI10	$O_2(b_1Sg^+) + O(3\,P) \longrightarrow O_2(a_1Dg) + O(3\,P)$	4e-20	[64]
NI11	$O_2(b_1Sg^+) + O_3 \longrightarrow 2\,O_2 + O(3\,P)$	1.5e-17	[64]
NI12	$O(-, gnd) + O_2(a_1Dg) \longrightarrow O_3 + e$	1.425e-16	[64]
NI13	$O(-, gnd) + O(3\,P) \longrightarrow O_2 + e$	1.9e-16	[64]
NI14	$O(-, gnd) + O_2 \longrightarrow O_3 + e$	1e-18	[64]
NI15	$O(-, gnd) + O_2(b_1Sg^+) \longrightarrow O(3\,P) + O_2 + e$	6.9e-16	[64]
NI16	$O(^+, gnd) + O(-, gnd) \longrightarrow 2\,O(3\,P)$	2.8e-13	[64]
NI17	$O(^+, gnd) + O_3 \longrightarrow O_2(^+, X) + O_2$	1e-16	[64]
NI18	$O(^+, gnd) + O_2 \longrightarrow O_2(^+, X) + O(3\,P)$	3.46e-16$Tg^{-0.5}$	[64]
NI19	$O(^+, gnd) + O_2(a_1Dg) \longrightarrow O_2(^+, X) + O(3\,P)$	3.46e-16$Tg^{-0.5}$	[64]
NI20	$O_2(^+, X) + O(-, gnd) \longrightarrow O_2 + O(3\,P)$	1.66e-12$Tg^{-0.5}$	[64]

Table A.5: Ion-Neutral and Ion-Ion reactions. The rate coefficient units are m^3/s.

Appendix B

Simulated Chemical Composition

In this appendix, using the kinetic model presented in chapter 4, the concentrations of all the species present in the model are shown, for some of the working conditions mentioned before.

Experimental Condition	**Pressure (Torr)**	**Total Flow (sccm)**	**CO_2 flow (sccm)**	**CH_4 flow (sccm)**
1	3	7.40	90 %	10%
2	3	7.40	50 %	50%
3	3	2.89	50 %	50%

Table B.1: Experimental conditions.

	Experimental Condition		
Concentration (%)	1	2	3
O_2	2.50	2.10e-3	7.44e-4
O	0.77	1.67e-3	8.72 e-4
O_3	4.00e-6	$<$ 1e-7	$<$ 1e-7
CO_2	49.69	20.71	14.21
CO	30.93	28.01	33.94
C	1.20e-5	1.20e-5	9.00e-6
CH_4	0.33	22.85	15.60
CH_3	1.03e-4	1.51e-2	0.01
H	0.19	4.68e-3	3.26e-3
H_2	5.83	16.15	21.37
CH_2	6.00e-6	5.52e-3	5.10e-3
OH	3.16e-4	1.05e-3	6.45e-4
H_2O	9.62	8.46	9.96
CH_2O	0.14	0.64	0.61
HCO	9.40e-5	1.50e-3	8.54e-4
CH	$<$ 1e-7	6.00e-6	3.00e-6
C_2	$<$ 1e-7	1.8e-5	2.5e-5
C_2H	$<$ 1e-7	$<$ 1e-7	$<$ 1e-7
C_2H_2	$<$ 1e-7	0.26	0.53
C_2H_3	$<$ 1e-7	1.10e-3	2.24e-3
C_2H_4	$<$ 1e-7	1.38	1.99
C_2H_5	$<$ 1e-7	0.02	0.03
C_2H_6	2.00e-5	1.49	1.73

Table B.2: Chemical Composition.